N64-13288

JPL CELESTIAL SENSOR ACTIVITIES

1 January 1960 through 1 January 1963

FOR INFORMATION ONLY

This work was performed for the Jet Propulsion Laboratory, California Institute of Technology, sponsored by the National Aeronautics and Space Administration under Contract NAS7-100.

JPL- 22801

JET PROPULSION LABORATORY INTEROFFICE MEMO

TO: H. H. Haglund April 4, 1963

FROM: G. W. Meisenholder

SUBJECT: Summary of Celestial Sensor Activity to be Discussed at Goddard Space Flight Center 11 April 1963.

1.0 This Memo is a summary of JPL guidance and control celestial sensor development activity over the past three years. Since time for preparation of this report has been short it is comprised mainly of excerpts from previous internal and external JPL documents.

2.0 Sensors that have flown.

a. Ranger Sun Sensors (See pages 5, 6, 8, 9, 25).

1. Rugged - no moving parts - can be dipped in liquid nitrogen with no effect.

2. No appreciable scale factor change over large solar constant change.

3. 4π steradian field of view.

4. 200 milliwatt power consumption during cruise.

5. Large output - 16 volts/degree at 6K output impedance. No preamplifier required.

6. Accuracy average on 24 single axis pairs:

40°F to 160°F null shift = 20 sec = .0057°.

Null offset average before flight acceptance testing = .7" $\pm$12 sec 1σ.

Null offset average after flight acceptance testing = 2.5" $\pm$20 sec 1σ.

The above numbers include test equipment errors.

b. Ranger Earth Sensor (See pages 7, 11-15, 25, 26, 29, 30, 56-61, 69, 70).

1. Rugged - no moving parts - no pressurization - no hot cathodes - no failures during shake or shock of 14 units.

2. Handles a large dynamic range by E^7 property of photomultiplier gain.

3. 2.9 watts, 2.6 lbs, 17 transistors.

4. Quite unsensitive to stray light.

5. Accuracy $\simeq .1^\circ\ 1\sigma + 5\%$ of apparent angular diameter of earth.

c. Mariner II Sun Sensors.

1. Very similar to Ranger types except the "shadow vane" is shorter. Scale factor is 9 volts per degree at $\simeq$ 6K output impedance. No preamplifiers required.

2. Sun Gate (See pages 34, 48). Indicates when sun is within 2.5° of sun for acquisition logic.

d. Mariner II Long Range Earth Sensor (See pages 28, 35, 36, 38-44, 67, 68, 71-78).

1. Field of view ±2° in roll ±5° in hinge.

2. Radiant input range 5×10^{-11} w/cm^2 to [illegible] $\times 10^{-7}$ w/cm^2 (6000°K bolometric). Some units could track 5×10^{-12} w/cm^2.

3. 6.2 lbs, 6.5 watts.

4. Absolute null stability .1° 3σ roll, .25° 3σ hinge.

5. Roll scale factor 4 v/deg ±10% over all radiant inputs above.

6. Hinge scale factor 4 v/degree.

7. Acquisition signal +7 volts ± 1 volt.

8. Light flux readout zero to -3 volts d. c.

9. Lens 7 element f 1.2 2" focal length.

3.0 Sensors developed to the working prototype stage.

a. Mariner A Horizon Scanner (See pages 27, 31-33, 39).

1. Works on 2° to 70° diameter planets.

2. Was an "outhouse" development.

3. Operates in 10 micron region using bolometer detector.

4. Four leaf rosette scan pattern with .5° x .5° instantaneous field of view.

5. Effective aperature 1.2" (3" actual) for 230°F energy.
6. 230°F is approximately 6 times "clipping" level.
7. Time constant of bolometer and pre-amp is one millisecond.
8. Time for one complete rosette is 560 milliseconds.
9. 50 transistors, 10 gears, 2 motors, 10 watts, 11 pounds.
10. Noise equivalent temperature @ 230°F = .4°K --- i.e., 0.4°F is equal to the RMS noise level at the pre-amp output (neglecting scan modulation). This is within a factor of 3 of calculated best S/N.

b. 5" Sun Sensor (See pages [illegible], 11, 34, 35).

Increased null stability in sun sensors without moving parts is possible by incorporating an occulting technique. An imaging sensor of this type has been fabricated and tested.

c. Mariner C Canopus Tracker (See pages 50, 53, 54, 55).

Utilizing an all electrostatic imagedissector tube the Mariner C Canopus tracker will yield error information for vehicle roll angular attitude control. Five cone angle positions are set during the mission by electronic means. No moving parts are required other than a possible sun shutter. Preliminary weight, power estimates are [illegible] pounds, 2.5 watts. Accuracy requirement is .5° 3σ.

d. Mariner C Square Root Sun Sensor.

In order to eliminate the necessity for gyros on initial sun acquisition a sun sensor system with a large "linear" range has been developed. Rate information is obtained by "looking at" the rate of change of position error signal.

e. Mariner C Earth Gate.

Simple photoconductive detector oriented in the earth direction used as an additional bit of information to verifying roll acquisition.

f. A vibrating mirror Canopus tracker to back up the primary Canopus tracker development just in case unforseen problems developed in the all electronic version. Total cost of parts and in house labor was 35K.

4.0 A. D. sensors in progress.

a. LPHS (Lunar and Planetary Horizon Scanner) (See pages 1-4).

This development has been let on a low level to Barnes Engineering. Initial progress has been extremely encouraging to date. This should ultimately result in a very long life no moving part horizon scanner with a large dynamic range of planet angle (10°→180°). See attached LPHS RFP specifications.

b. Photoconductive (visible) Planet Sensor.

To be used ultimately as a replacement for the Ranger earth sensor and for directing science toward the destination planet at a large initial range (say where the planet subtents .5°). No moving parts should be required.

c. Random star angular rate and position indicator.

This is directed for backup or possible total elimination of gyros on spacecraft.

d. 4 π Steradian Sun Sensor (See pages 48-50).

Will provide the sun direction in spacecraft coordinates to an accuracy of $\approx 6°$ over 4 π steradians. Very simple device with no moving parts utilizing silicon solar cell detectors.

e. Mariner B Canopus Tracker (See pages 50, 53-55).

Will essentially be the same as the Mariner C device except that greater null stability is required.

f. Approach Planet Scanner (See page 46).

To be used to determine approach guidance corrections on the destination planet. No hardware - analyses and drawings have been partially completed.

5.0 Special test equipment.

a. Chilao test site (See page 10) for sun and star tracking.

b. Earth-moon-star simulator (See pages 36, 43, 44) for precise lab performance tests.

c. IR planet simulators (See pages 32, 33, 51) for long wavelength scanner development and testing.

d. Sun simulator (See pages 10, 17, 19, 23, 24, 37, 47, 62-65). Presently comes close to delivering a uniform, 32' diameter sun at one solar constant.

e. Absolute spectroradiometer. This device is used to determine the absolute flux output of a simulator or source v/s wavelength.

6.0 Other development projects.

a. Electrostatic image dissector (See pages 52, 53).

Attachment A to
Request for Proposal 2960

GENERAL SPECIFICATION

Lunar and Planetary Horizon Scanner

18 September 1962

Prepared by ______________________________
G. W. Meisenholder

GENERAL SPECIFICATION

Lunar and Planetary Horizon Scanner

1. SCOPE.

1.1 Scope. This General Specification covers anticipated requirements for a Lunar and Planetary Horizon Scanner prototype, hereinafter referred to as LPHS, that would be useful for Lunar orbiters as well as other missions, including Voyager terminal guidance and orbiters of Mars and Venus.

1.2 Description. The LPHS provides:

a. two-axis local vertical position error signals and apparent angular diameter information to be used for range purposes against the following celestial objects in the order of their relative priority: (1) Moon, (2) Mars, (3) Venus, and (4) Earth.

2. APPLICABLE DOCUMENTS.

2.1 No JPL Specifications are included in this General Specification.

3. REQUIREMENTS.

3.1 Accuracy and dynamic range. The accuracy and dynamic range requirements are shown in Figure 1.

Figure 1
Accuracy Requirements Vs. Range from Surface

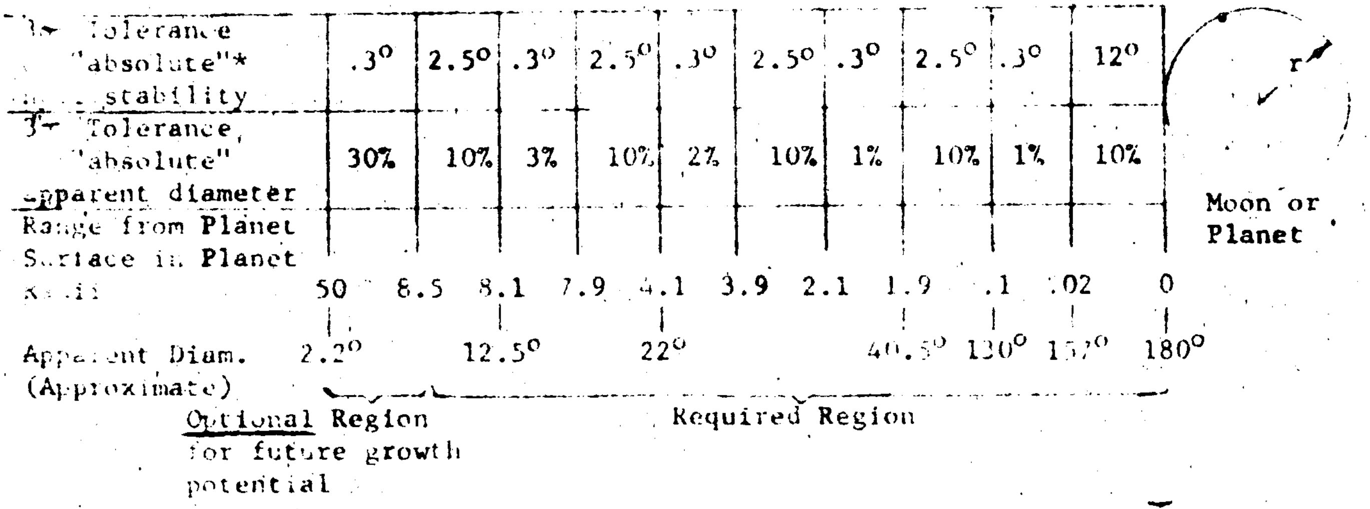

3σ Tolerance "absolute"* null stability
.3°
2.5°
.3°
2.5°
.3°
2.5°
.3°
2.5°
.3°
12°
3σ Tolerance, "absolute" apparent diameter
30%
10%
3%
10%
2%
10%
1%
10%
1%
10%
Range from Planet Surface in Planet Radii
50
8.5
8.1
7.9
4.1
3.9
2.1
1.9
.1
.02
0
Apparent Diam. (Approximate)
2.2°
12.5°
22°
40.5°
130°
157°
180°
Optional Region for future growth potential
Required Region
r
Moon or Planet

*Absolute null stability is the maximum allowable in flight angular deviation between "the instrument" electrical null position and its external mechanical reference surfaces. (In contrast with resolution which is the minimum detectable angular change.)

3.2 Optional accuracy. The optional accuracy under influence of a disturbing radiant source:

a. If a foreign radiant source is within 10° of the planet limb being tracked (See Figure 2.) the accuracy requirements of Figure 1 may be relaxed to 2.5° null stability and 10% range accuracy. The Contractor must indicate in his proposal under what situations he feels it will be necessary for his proposed device to use this option. In flight, the device must yield an alarm output of 7 volts ± 10% (into a 50K resistive load) when the optional accuracy applies.

Figure 2
Foreign Radiant Source Disturbance Geometry

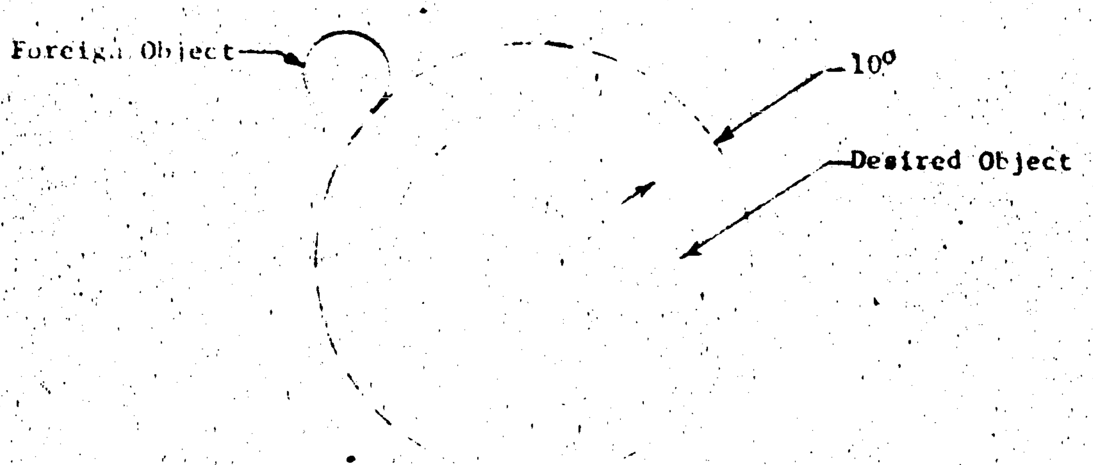

3.3 Acquisition range. The LPHS shall deliver properly phased error signals or search logic signals when the near planet limb is within 35° of the LPHS mechanical null line of sight. A larger acquisition field of view is desirable, if possible.

3.4 Time constant. Two second maximum, .1 second desired to a 1.2° + 3σ null requirement, step function change in angular position from null. Time constant refers to response within the linear range region only.

3.5 Error signal output. The two axis output error signals shall be analog .6 volt per degree (± 10%) with an output impedance of 3000 ohms. Linear range is described by Figure 3. Note that the dead band may be a function of the accuracy requirement, if necessary.

Figure 3
Output Error Characteristic

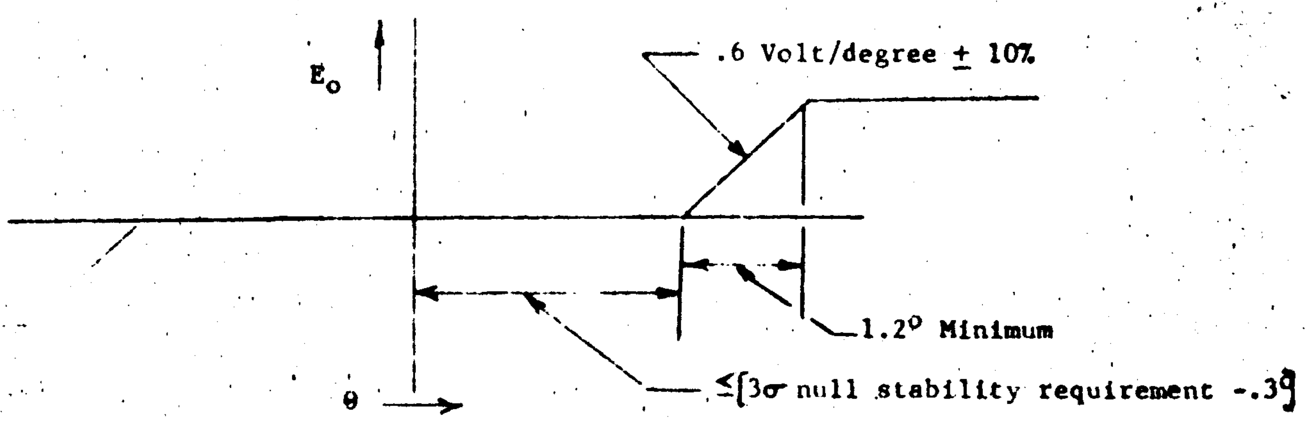

3.6 Apparent diameter output. The apparent diameter output may be analog or digital, linear or nonlinear, and is left up to the Contractor. The apparent diameter output must be single valued when the planet is within 1.2° + 3σ null requirement of its external alignment reference null position.

3.7 Available power. The following power will be available to the LPHS:

2400 cycle square wave 104 volt peak-to-peak (± 5% tolerance on the RMS value)

400 cycle single phase 26 v RMS

D.C. battery power 28 V $^{+6V}_{-4V}$

3.8 Prototype definition. The LPHS prototype developed under this Contract need not be the flight configuration.

a. An optical breadboard, neatly packaged, the volume of which should be approximately the same as the expected flight hardware, is visualized as the mechanical configuration of the optical portion of the prototype.

b. An electronic breadboard, neatly packaged, the volume of which is not specified, is visualized as a satisfactory configuration for the electronics portion of this prototype.

c. The electronic and optical breadboards, when properly interconnected, must meet the other accuracy specifications of this General Specification.

4. ANTICIPATED SPECIFICATIONS FOR THE FOLLOW-ON FLIGHT UNITS.

4.1 The anticipated specifications for the follow-on flight units include the following requirements:

a. Specification No. 30258, Environmental Specification, Mariner B Flight Equipment

b. Specification No. 20061A, JPL Preferred Parts List

c. Specification No. 30237, JPL Component Screening Specification

d. Continuous unattended operation in flight of three (3) years mean time to failure.

e. It is desirable, although not mandatory, that the follow-on flight hardware be capable of withstanding heat sterilization of 145°C for twenty-four (24) hours non-operating.

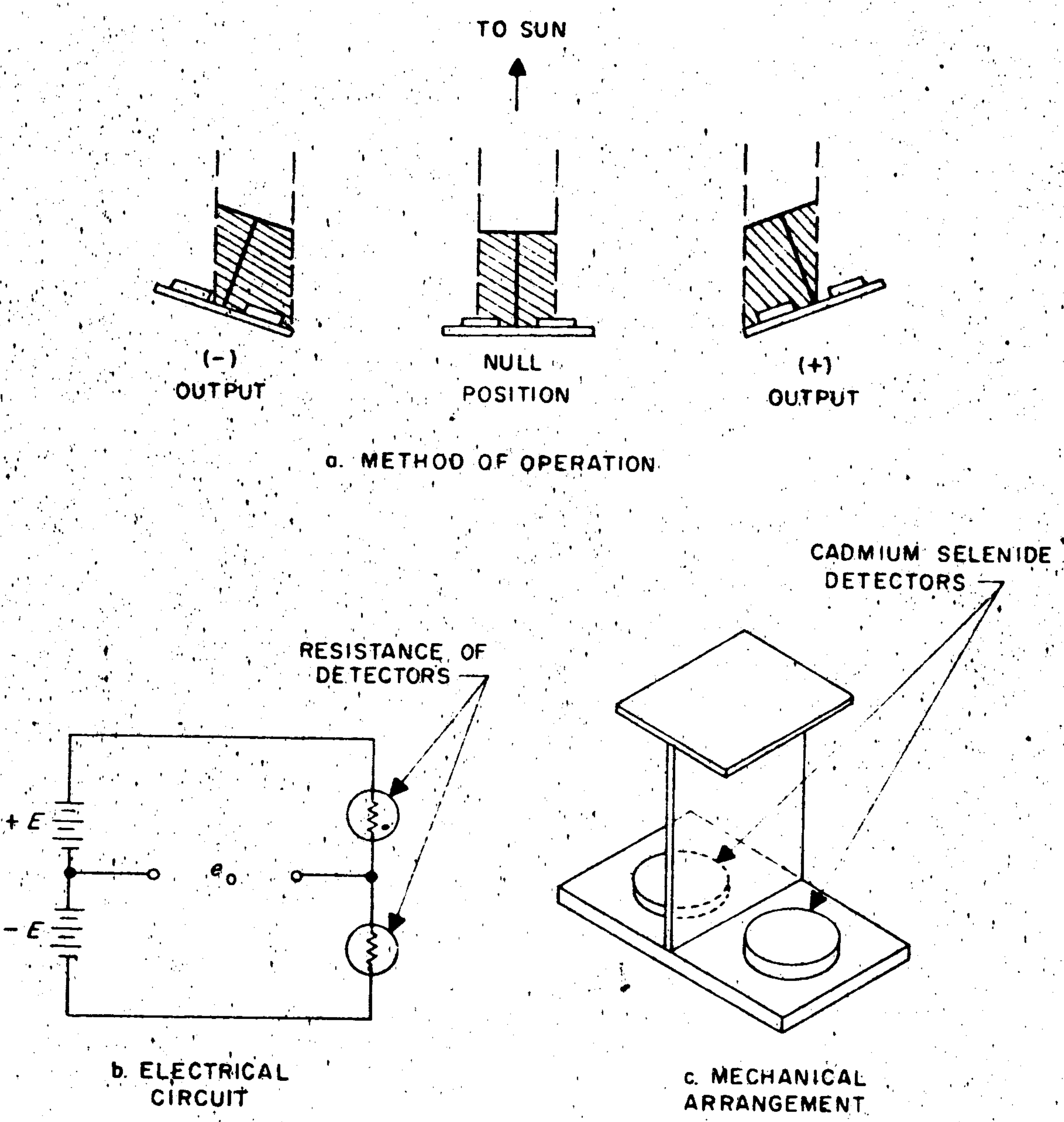
TO SUN
(-) OUTPUT
NULL POSITION
(+) OUTPUT
a. METHOD OF OPERATION
RESISTANCE OF DETECTORS
+E
-E
e_0
b. ELECTRICAL CIRCUIT
CADMIUM SELENIDE DETECTORS
c. MECHANICAL ARRANGEMENT

Fig. 1. Sun sensor

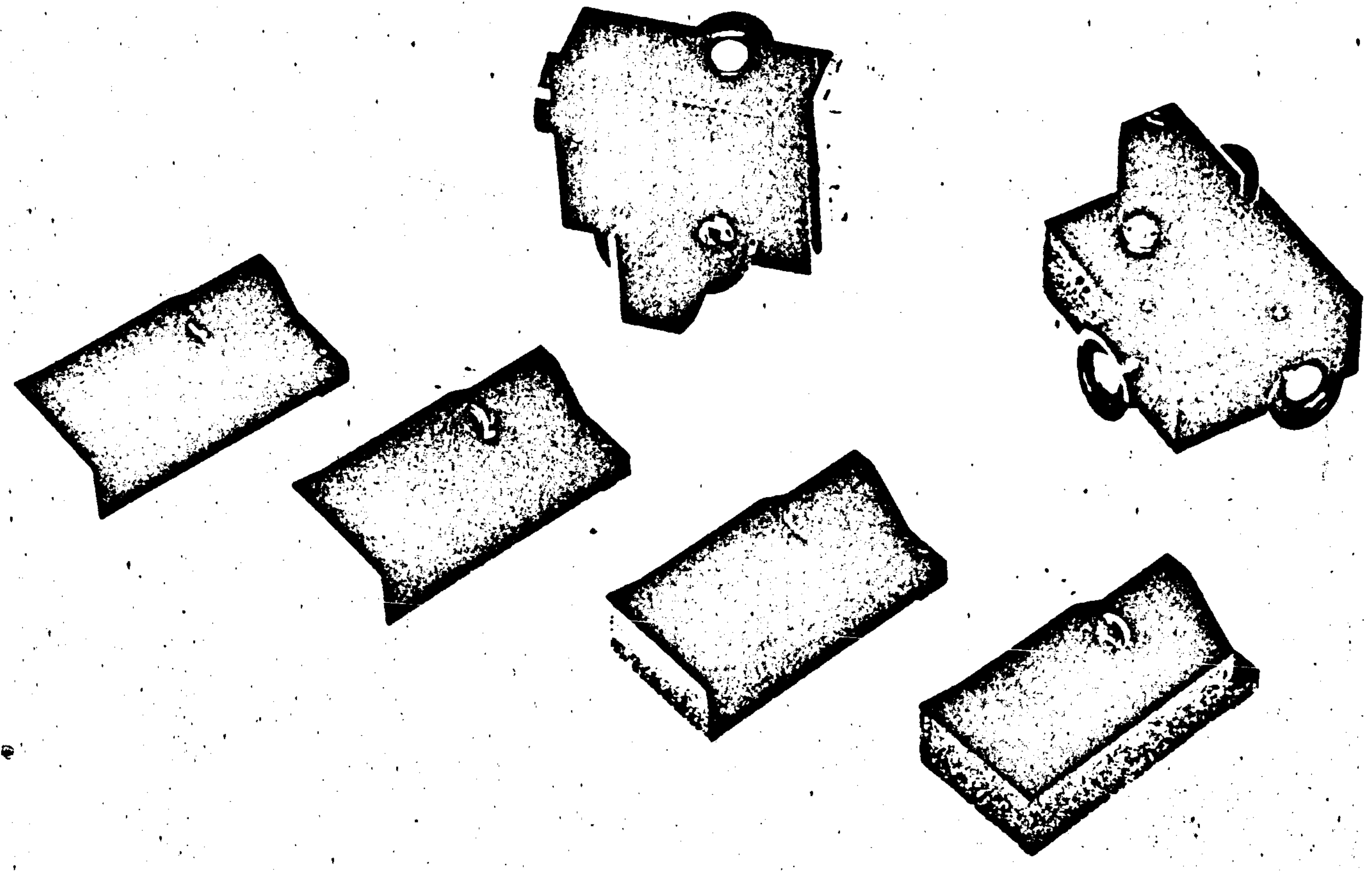

Fig. 2. Sun sensors and Sun finders

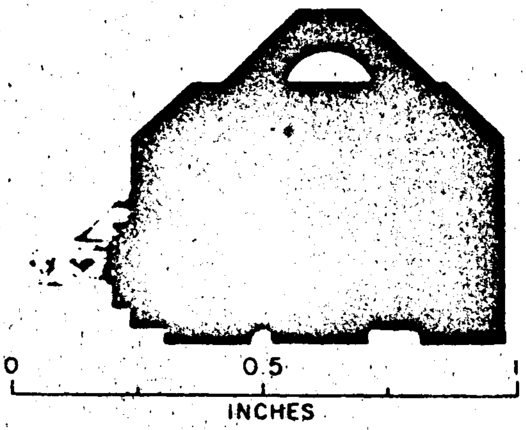
0
0.5
1
INCHES

Fig. 3. Sun sensor shadowing technique

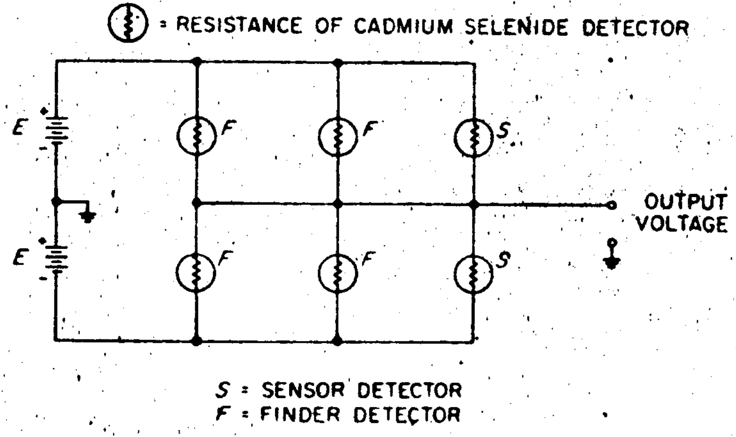
= RESISTANCE OF CADMIUM SELENIDE DETECTOR
E
E
F
F
S
F
F
S
OUTPUT VOLTAGE
S = SENSOR DETECTOR
F = FINDER DETECTOR

Fig. 4. Sun sensor electrical circuits

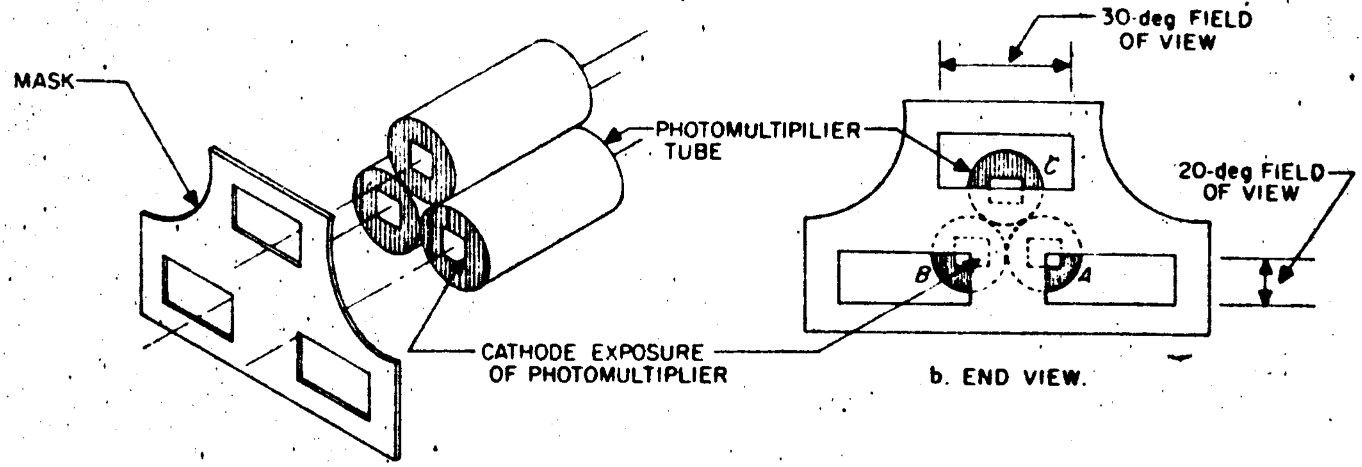
MASK
PHOTOMULTIPILIER TUBE
CATHODE EXPOSURE OF PHOTOMULTIPLIER
30-deg FIELD OF VIEW
20-deg FIELD OF VIEW
C
B
A

a. ISOMETRIC VIEW

b. END VIEW.

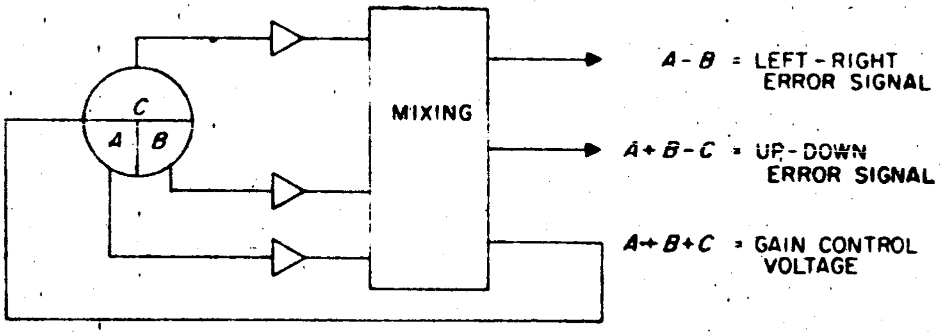
C
A
B
MIXING
A - B = LEFT - RIGHT ERROR SIGNAL
A + B - C = UP - DOWN ERROR SIGNAL
A + B + C = GAIN CONTROL VOLTAGE

c. ELECTRICAL CIRCUIT

Fig. 5. Earth sensor

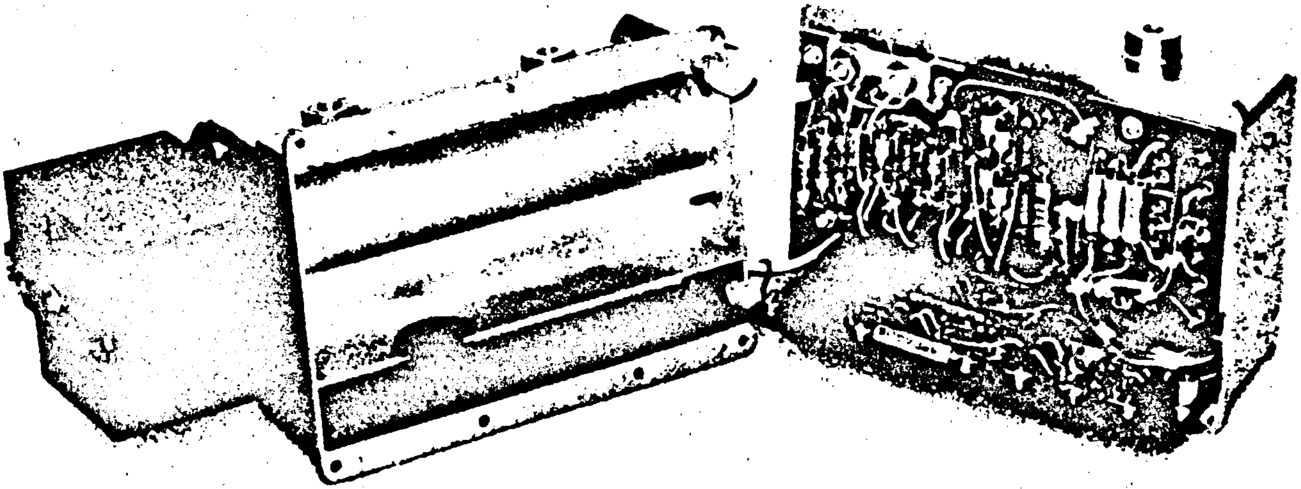

Fig. 6. Photograph of Earth sensor

1. Attitude Control

As reported in previous *SPS*, the *Ranger* attitude control utilizes a sun-earth reference system with dry nitrogen jets operating in an on-off manner as the actuation method. The sun is the primary reference toward which the axis of symmetry (roll axis) of the spacecraft is directed in response to signals from an array of photoconductive cells. The earth reference is acquired using a 2-axis optical sensor mechanized around three photomultiplier tubes. This sensor is mounted to and moves with the high-gain antenna hinge motion (about pitch axis) and is directed toward the earth by the hinge motion and by rolling the spacecraft. The earth sensor thus controls the roll attitude of the spacecraft and the hinge angle of the antenna to keep the antenna pointed toward the earth.

a. Sun sensor. The *Ranger* sun sensors are optical devices which use a shadow technique on a photoconductive detector. The detectors are CdSe cells made by Clairex Corporation. The primary units (Fig 15) mount on the frame of the spacecraft and nominally point at the sun during the flight limit cycle operation. The secondary units (Fig 15) are used to complete a spherical field of view requirement and mount on the underside of the solar panel tips. They function only during acquisition of the sun.

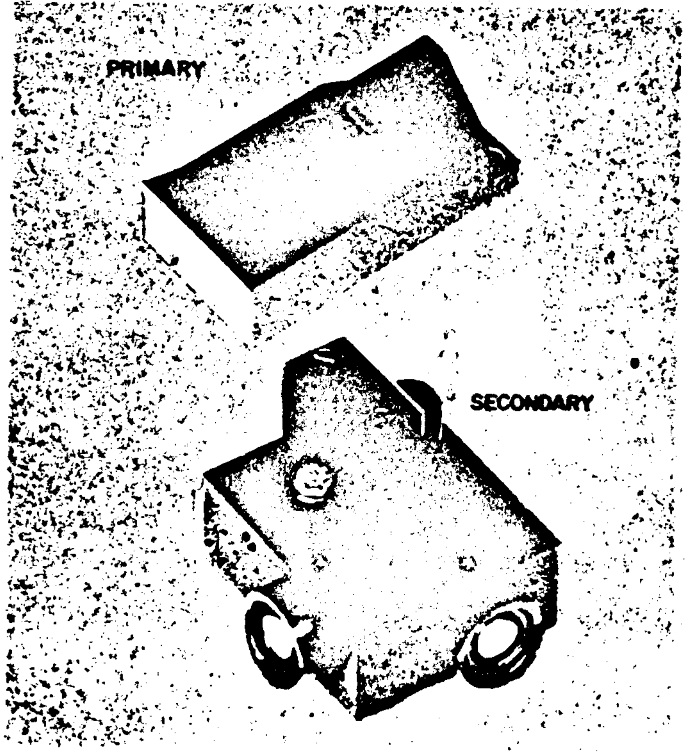

Figure 15. Sun sensors

These detectors are connected in a bridge circuit (Fig 16). The output signal is a voltage developed across the 50K resistive load. In the spacecraft this load will be the input impedance of a summing amplifier. The sensor positive and negative supplies will be zener regulated to 16 volts from the spacecraft 28-volt supplies.

An analysis of the circuit leads to the following equation for the primary sun sensor voltage output

$$E_o = \frac{E(R_2 - R_1)}{R_1 + R_2 + \dfrac{R_1R_2}{R_L}}$$

where R_1 and R_2 are the resistance values of primary detectors (Fig 16) A and F.

Due to the shadowing method on the semiconductor the resistances of the cell as a function of angle from null are very closely approximated by

$$R_{1,2} = Ae^{\pm b\Delta\theta}$$

where $\Delta\theta$ is the angular deviation of sensor from null in degrees.

The sign on the exponential is opposite for two opposed detectors. Although the constants A and b vary with the particular cell chosen, paired detectors with these constants approximately equal have been obtained through a matching process. The nominal values are $A = 6K$ ohms and $b = 0.962$ deg^{-1}. Using these forms for R_1 and R_2, the voltage output as a function of angle from null becomes

$$E_o = \frac{2E \sinh(b\Delta\theta)}{2\cosh(b\Delta\theta) + \dfrac{A}{R_L}}$$

To better understand the effect of each environmental condition on sun sensor performance, accurate before and after data was taken. Approximately a 0.03-degree null shift was observed upon subjecting a primary pair to the type approval vibration environment. This information implies that the effects of vibration were quite small since the day to day null stability has typically been about 0.02 degree. Null shift induced by temperature stabilization of a primary pair was 0.06 degree.

Tests have been performed which indicate that null shifts due to changes in intensity are not serious. A 33% decrease in intensity caused only a 0.02-degree null shift. Since this function is apparently continuous, there is strong support for the assumption that performance of the sun sensor will be virtually unchanged by removing it from the earth's atmosphere.

A best estimate of sun sensor null stability for RA-1 and RA-2 missions is shown in Table 2. These calculations indicate that the sun sensor has a good probability of meeting the original design goal of 0.25 degree 1σ.

The RA-3 sun sensor has been designed to improve null stability by a factor of two. Projecting RA-1 figures into the RA-3 configuration yields an estimate of 0.104 degree 1σ (1.82 milliradians) for this version.

The secondary sun sensors are mounted on the solar panels and may undergo a significant thermal shock between injection and sun acquisition due to removal of the hot shroud. Unpotted detectors in their housings were subjected to a thermal shock of 18°F/min from 250 to −100°F with no damage or change in characteristics. However, in potted units which underwent the same test the glass detector enclosure cracked. After experimentation it was decided that Stycast 2741, a variable hardness potting compound, would be acceptable. Detectors potted

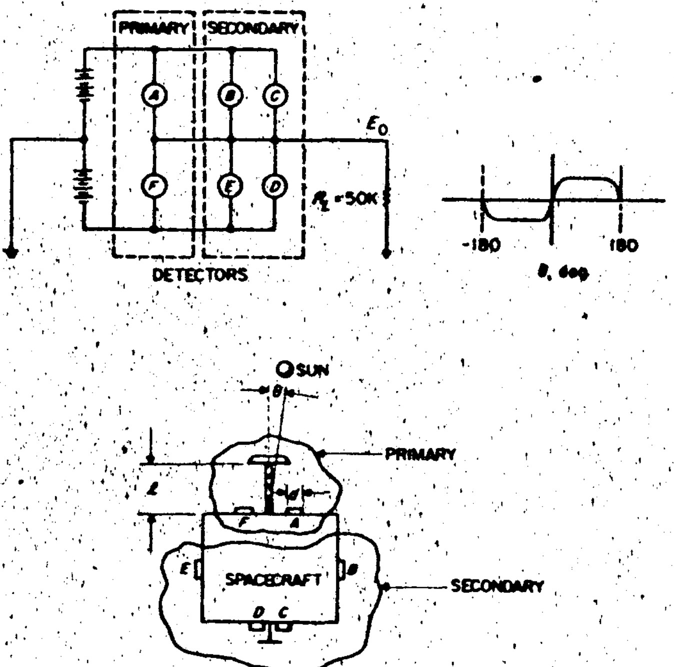

Figure 16. Sun sensor schematic

Table 2. Estimate of sun sensor null stability

Parameter, deg	Null shift (1σ)
Daily random variations	0.02
Asymmetrical temperature of 20°C (assumed 1σ)	0.16
Temperature cycle due to sterilization	0.10
Temperature cycle due to injection	0.05
Intensity change	0.03
Vibration	(small)
Mechanical alignment	0.03
Power dissipation	0.05
Total	0.207 (3.61 mrad)

with this compound survived the required thermal test. A complete evaluation of the sun sensor system under the type approval environment is currently under way.

There are many difficulties inherent in the problem of simulating an extremely bright, collimated light source. Therefore, most of the sun sensor testing has been done with the sun as the source. A temporary test site has been constructed at Chilao, California (Fig 17). The facility uses a two mirror coelostat system to provide a collimated sun bundle at a constant position. This bundle is directed through a tube into a trailer to a Leitz optical dividing head which rests on a stable tripod. The system includes a bore sighting telescope and motors to drive the coelostat mirrors. The overall accuracy of the pointing system is better than 10 seconds of arc. The sensors are tested by mounting them on the dividing head and positioning to known angles while monitoring the outputs.

A technique for increasing the null stability of a dc sun sensor system is use of partial sun occulting. This can be simply implemented in a two axis sensor by the following means. The shape of the four quadrant detector is shown in Figure 18 for purposes of illustration only. The actual shape will vary depending on the desired input-output characteristic. The amount of sun image spill-over in conjunction with detector stability determines basic electrical null stability of the device. A mathematical example of how the occulting technique improves null stability is as follows:

$$x + y = S - C, \tag{1}$$

$$y = S - C - x \tag{2}$$

assuming linear detector input-output characteristics. The control system will work to balance output of A and B detectors.

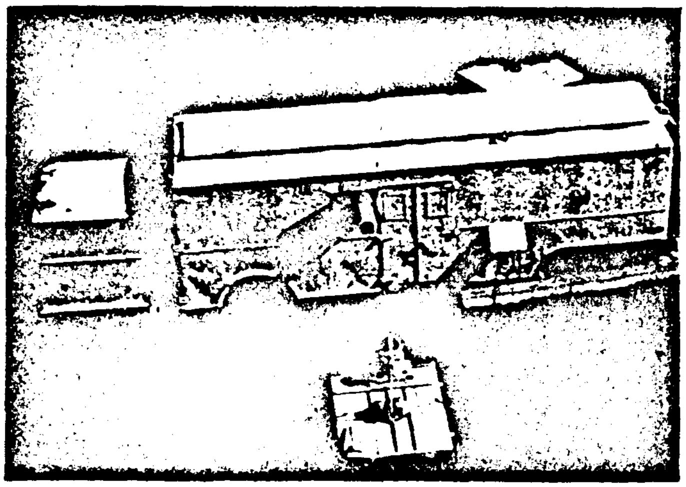

Figure 17. Chilao test site

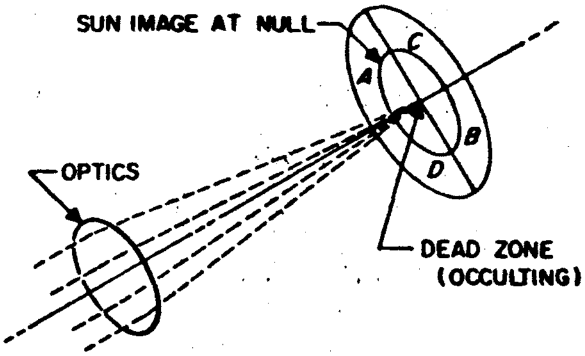

Figure 18. Four quadrant detector

$$E_0(A) = E_n(B) \tag{3}$$

from servo loop action.

$$E_0(A) = K_a Y = K_a(S - C - x) \tag{4}$$

where *K*'s are relative detector gains.

$$E_n(B) = K_b x \tag{5}$$

$$\therefore K_b x = K_a(S - C - x) \tag{6}$$

$$x = \left[\frac{K_a}{K_b + K_a}\right](S - C)$$

Note that if $x = S - C/2$ the null shift $= 0$.

$$\text{Null shift} = \left[\frac{K_a}{K_b + K_a}\right]^{-\frac{1}{2}}(S - C) \tag{7}$$

This exercise shows that null shifts can be held to a minimum by decreasing the amount of spillover and matching detector characteristics with temperature, etc. For purposes of illustration (Fig 19), if the spillover $S - C/2$ is 3 minutes of arc and detector *B* has a gain decrease from 1 to 0.5 the null position will shift 1 minute of arc. This is within the 1-minute design goal even with the large detector gain changes noted. A sun sensor employing this principle has been fabricated (Fig 20) and is being tested now.

b. Earth sensor. Earth sensor optical mechanization is much the same as the sun sensor in that a variable aperture (shadowing) technique is used. The detectors in this case are three ¾-inch diameter end-on photomultiplier

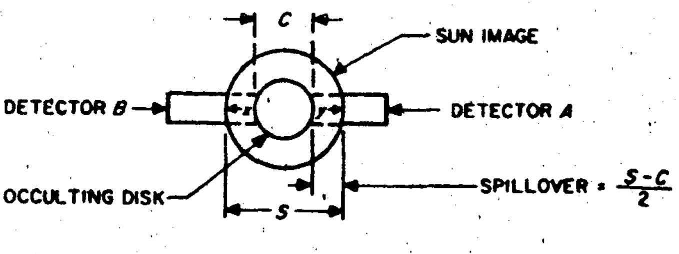

Figure 19. Two quadrant detector

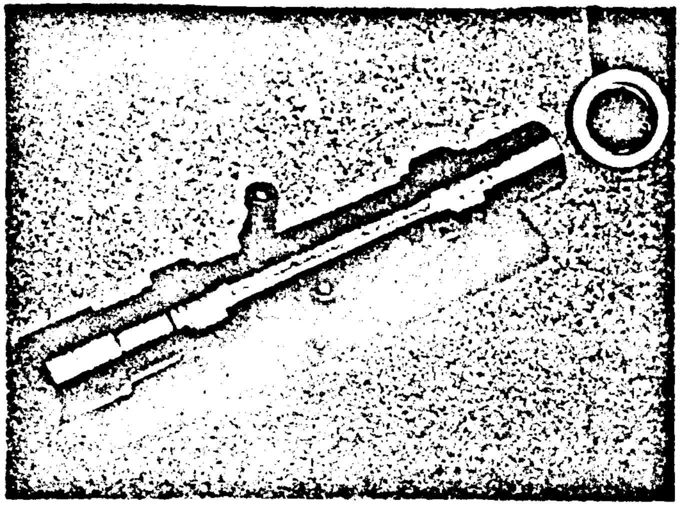

Figure 20. Test sun sensor

tubes arranged so that their outputs can be resolved into two axis error signals.

This sensor has field of view requirements of ±30 degrees in hinge (antenna direction) and ±20 degrees in roll. Linear range extends only ±2.5 degrees on either axis from null at which points the output error signals saturate and remain saturated to the field of view limits. A typical plot around a null is shown in Figure 21. If the earth moves away from null on a line not along either axis, the performance becomes truly two dimensional. Note from Figure 22 that as the earth moves in the positive θ roll direction the hinge error signal weakens because less of the cathodes of A and B photomultipliers is exposed. For motion in θ hinge direction, however, the gain on the roll axis remains essentially constant. In reality neither of these conditions will be precisely true due to variations in sensitivity over the photomultiplier cathode surfaces. The actual experimental situation is illustrated in Figure 23. The coordinate axes are roll and hinge dc error signals. The vertical lines are lines of constant hinge angle θ_H and the horizontal ones are constant roll angle θ_R. The nonsymmetry of the actual two axis output plot cannot be entirely justified by variations in cathode sensitivity and remains unexplained at this time.

Electrically the earth sensor uses photomultiplier tubes excited with a 150-volt ripple on 1200 volts dc. The light inputs to the photomultiplier tubes are then used to amplitude modulate this 400-cycle ac signal at the photocathode. This modulated signal is amplified in the tubes by the dynode multiplier section and also by 400-cycle bandpass preamplifiers which follow each tube. The outputs of the preamplifiers are then mixed in a transformer bank to obtain the roll and hinge error output signals.

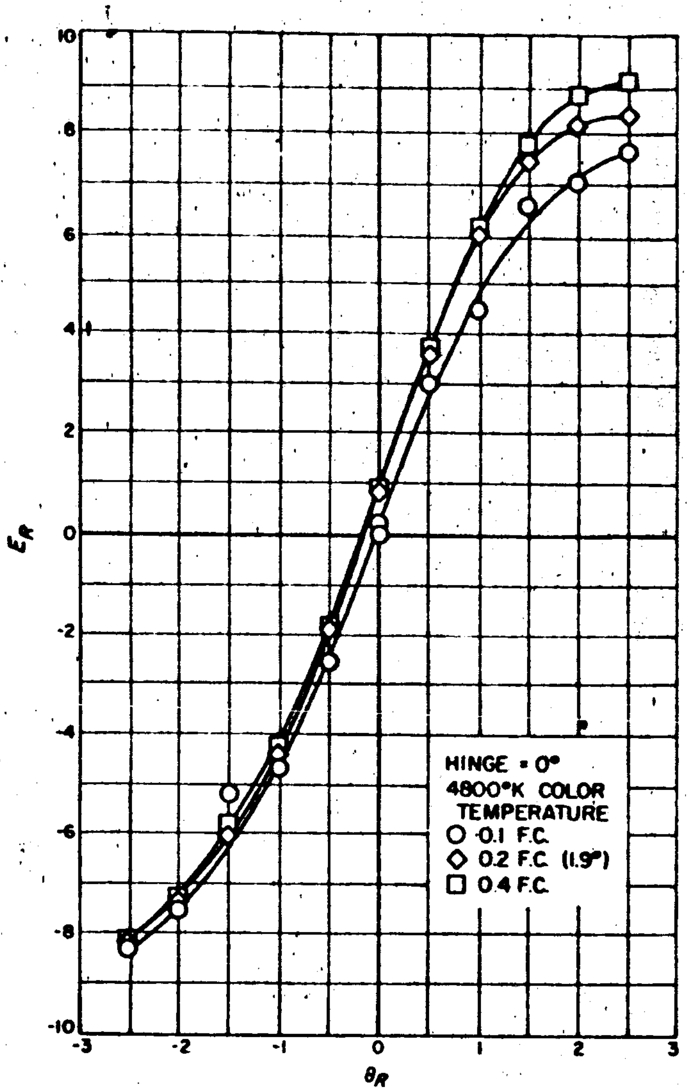

Figure 21. Earth sensor roll axis characteristics

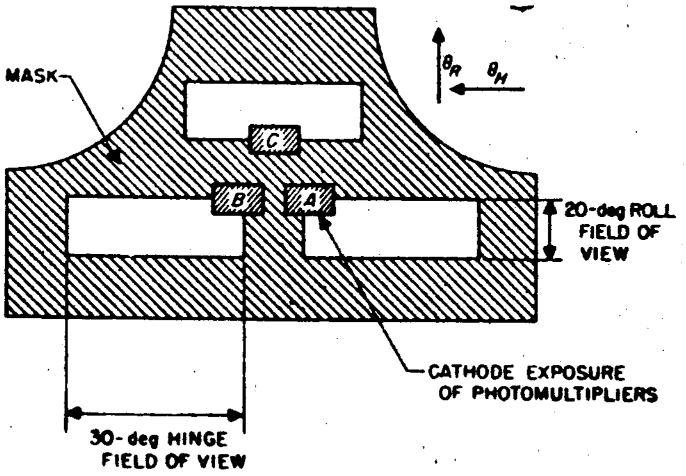
MASK
θ_R
θ_H
C
B
A
20-deg ROLL FIELD OF VIEW
CATHODE EXPOSURE OF PHOTOMULTIPLIERS
30-deg HINGE FIELD OF VIEW

Figure 22. Earth sensor shadow box

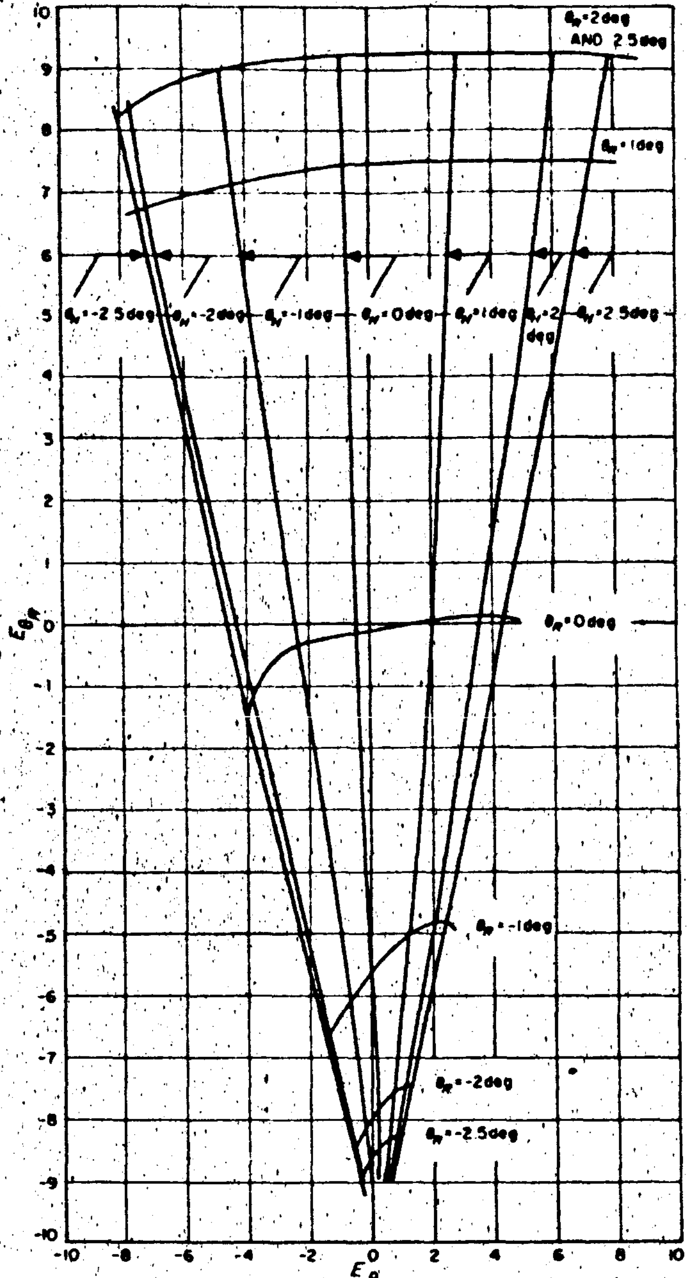

Figure 23. Earth sensor sensitivity characteristics

Also obtained from this mixing section is an acquisition signal equal to the total output of the photomultipliers, $A + B + C$. This is used to automatically adjust the system gain for various earth intensities. This acquisition signal is subtracted from a 400-cycle reference signal and the difference is used to drive a power amplifier which supplies the excitation to the photomultiplier tubes. Thus a loop is established around the tubes which controls the sum of their outputs to be a constant independent of earth intensity. The complete schematic is shown in Figure 24. Physically the earth sensor is as shown in Figure 25.

The environmental evaluation of the earth sensor is not completed at this time. However, a flight unit has successfully passed the RA-1 flight acceptance vibration and vacuum environments. The earth sensor is gold plated and thermally insulated from the antenna yoke to maintain control over the operating temperature. This control will be accomplished primarily by controlling the outer surface emissivity through black stripping.

Testing on the earth sensor components is done before assembly of the complete earth sensor. The photomultiplier tube characteristics as a function of voltage excitation and light intensity are measured. Gain adjustments are made through resistor changes in the dynode string. Then sets of three matched tubes are selected. The preamplifiers and power amplifier are bench checked after fabrication. The completely assembled unit is functionally tested to confirm the data shown in Figure 23. This functional testing is done by mounting the earth sensor on a T-2 theodolite for angle positioning. It is then placed in front of a simulated earth. A photograph of this setup is shown in Figure 26. The output of the earth sensor is demodulated as in the spacecraft and the hinge and roll error signals are monitored with dc voltmeters. Variation in earth sensor performance with intensity change can also be obtained by varying the intensity of the simulated earth. Some results of such tests are shown in Figure 21. For temperature tests (Fig 27) a device has been made which remote controls the theodolite from outside a temperature chamber. Thus with the simulator and theodolite controls outside the oven, but the earth sensor mounted on the theodolite inside, it is possible to run all of the previous tests at controlled temperatures.

Test numbers (Table 3) are possibly pessimistic since all tests at this time have been done on prototype units. The analysis also makes the assumption that all disturbances will be present during flight which is probably not true.

c. Jet valves. Ten miniature jet valves are employed on the *Ranger* spacecraft to control attitude. Four valves each are used to control the yaw and roll axes providing pure couples, and the remaining two valves control the pitch axis. On *Ranger* RA-3 the center of mass is expected to shift significantly along the roll axis. Therefore, utilization of a pure couple for roll control permits the roll valve positions to be frozen for all spacecraft.

The axis of each valve is oriented to prevent gas from impinging onto structure during valve actuations. Investigations have shown conclusively that the bias or coupling effects of impinging gas are significant. This

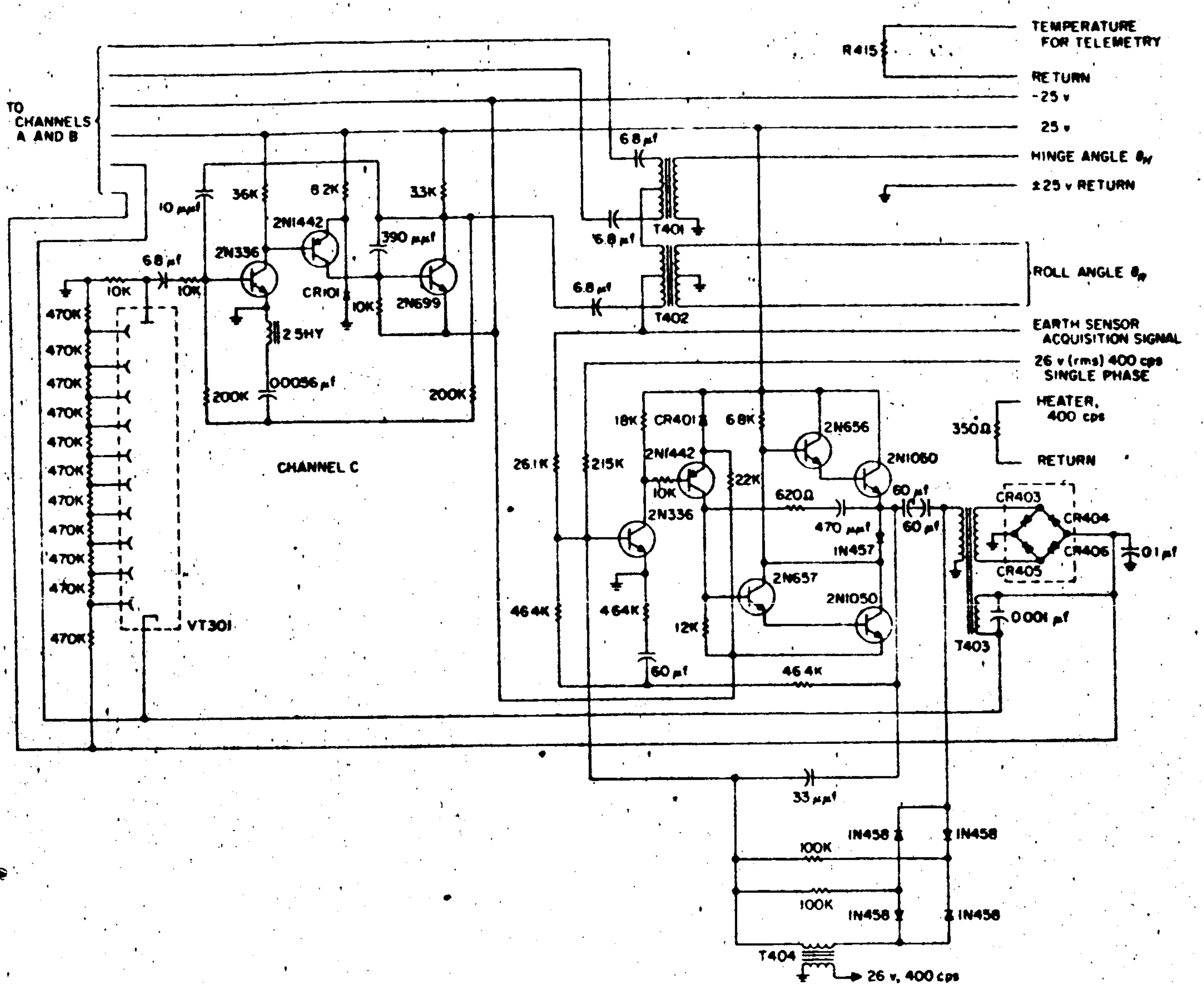
TEMPERATURE FOR TELEMETRY
R415
RETURN
-25 v
25 v
HINGE ANGLE θY
±25 v RETURN
ROLL ANGLE θR
EARTH SENSOR ACQUISITION SIGNAL
26 v (rms) 400 cps SINGLE PHASE
HEATER, 400 cps
350Ω
RETURN
TO CHANNELS A AND B
6.8 µf
6.8 µf
6.8 µf
T401
T402
10 µµf
36K
8.2K
33K
2N1442
2N336
390 µµf
2N699
CR101
10K
6.8 µf
10K
10K
470K
2.5HY
.00056 µf
200K
200K
CHANNEL C
VT301
18K
CR401
6.8K
2N656
2N1050
26.1K
215K
2N1442
22K
10K
620Ω
60 µf
470 µµf
60 µf
1N457
2N336
2N657
2N1050
46.4K
4.64K
12K
60 µf
46.4K
CR403
CR404
CR405
CR406
.01 µf
0.001 µf
T403
33 µµf
1N458
1N458
100K
100K
1N458
1N458
T404
26 v, 400 cps

Figure 24. Earth sensor schematic

influence established the requirement that the yaw control valves be moved from their earlier position on the pitch axis to a position giving a clear field of view (i.e., the solar panel actuator arm was obstructing one of the valves on the pitch axis). This off axis condition gave rise to the requirement for two additional valves in controlling yaw, thus providing pure couple control. The pitch control valves have been oriented with their axes 25 degrees away from the roll axis to prevent gas from impinging on the forward structure of the spacecraft.

Development of the jet valve manufactured by Whittaker Controls has been slow. The design objective of 1 cc/hr maximum external leakage as measured by a mass spectrometer has been difficult to achieve with the valve having all metal seals. Almost perfect spherical conformity and concurrence between the ball poppet and seat are essential to minimize leakage. Greater quality control and new techniques of manufacturing have enabled the manufacturer recently to ship valves which meet the leakage requirements before and after 50,000 cycles of actuation.

Figure 28 illustrates ten valves set up in a test block undergoing cycling tests. The valves shown have completed the *Ranger* type approval environmental requirements without evidence of mechanical weakness.

d. Pressure regulators. The attitude control pressure regulator reduces the source pressure, carried by a pressure vessel, of nominally 3000 psi down to 15 psig for use by the jet valves.

Two radically different regulators are undergoing qualification for the *Ranger* spacecraft. The Sterer Engineering regulator, shown in Figure 29a, has passed all environ-

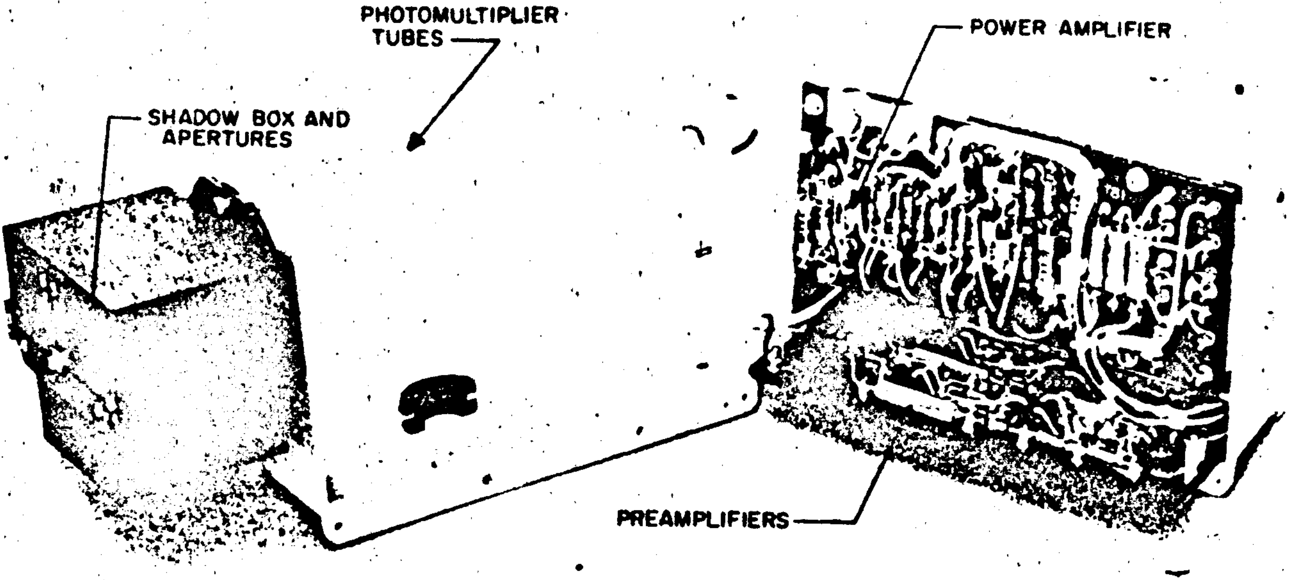
PHOTOMULTIPLIER TUBES
SHADOW BOX AND APERTURES
POWER AMPLIFIER
PREAMPLIFIERS

Figure 25. Earth sensor

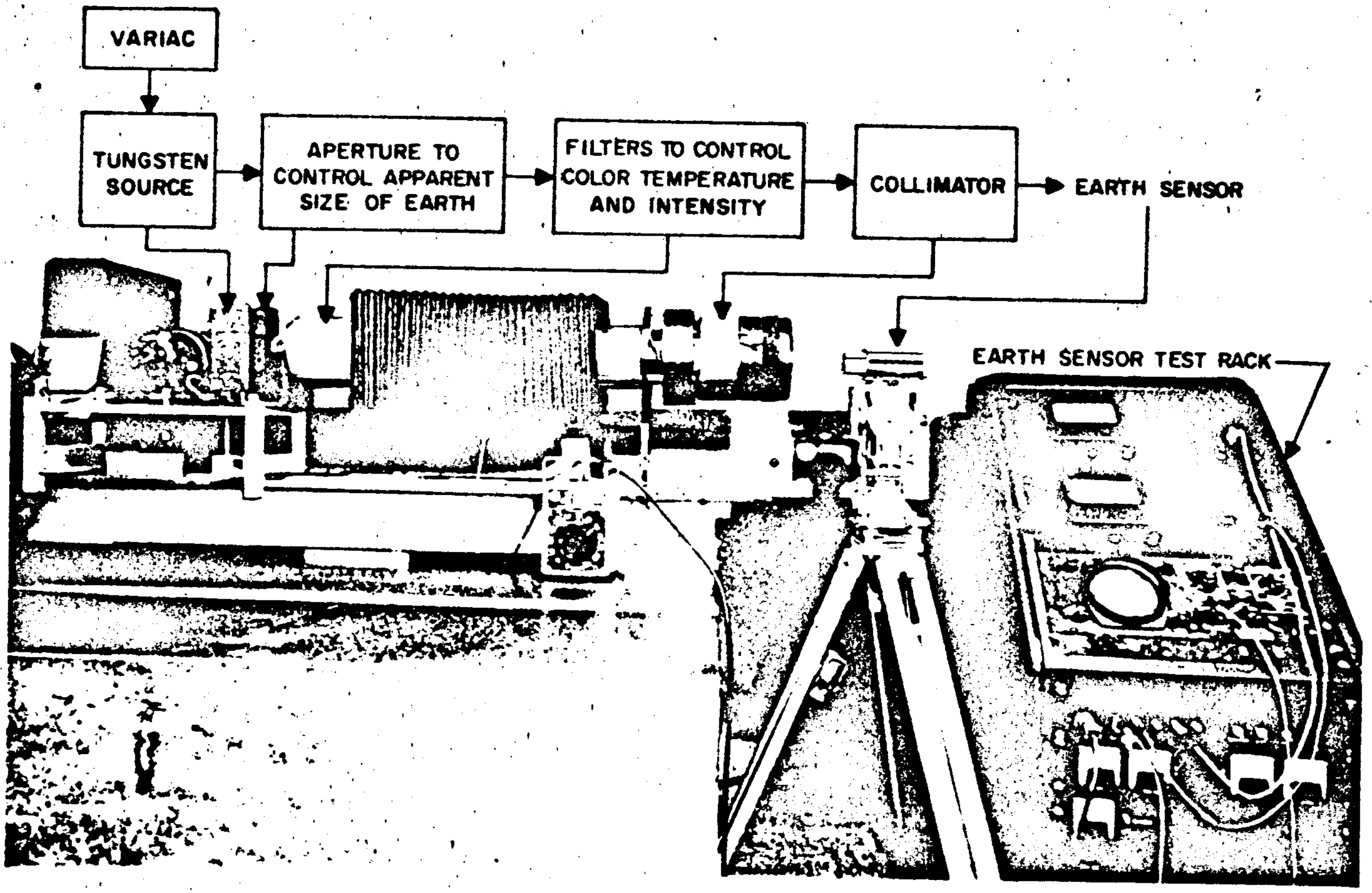
VARIAC
TUNGSTEN SOURCE
APERTURE TO CONTROL APPARENT SIZE OF EARTH
FILTERS TO CONTROL COLOR TEMPERATURE AND INTENSITY
COLLIMATOR
EARTH SENSOR
EARTH SENSOR TEST RACK

Figure 26. Earth simulator

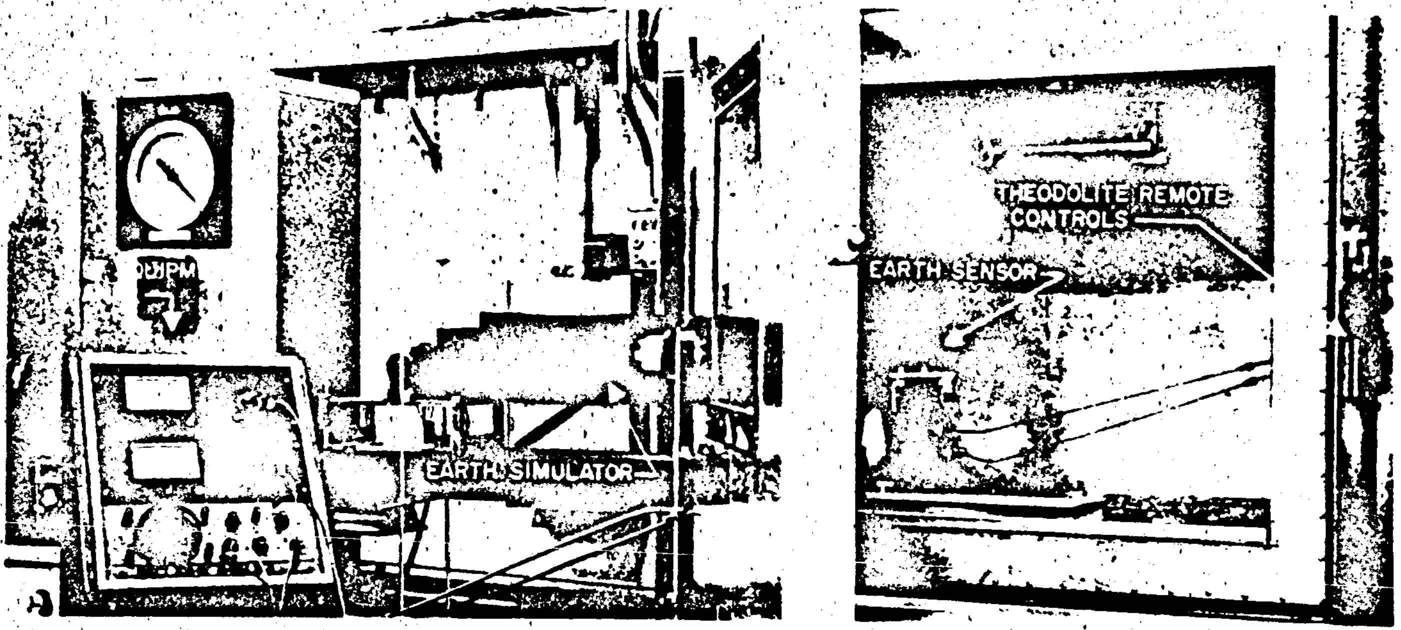
RPM
EARTH SIMULATOR
THEODOLITE REMOTE CONTROLS
EARTH SENSOR

Figure 27. Temperature test setup

V. SUPPORTING ACTIVITIES

A. Celestial Simulator Facilities

The celestial simulator facility will be used for many experiments relating to space exploration. It will provide this Laboratory with the capability of functionally testing spacecraft attitude control and space navigation systems, a facility for sensor development and a useful tool for basic research.

The celestial simulation facility (Fig 41) will be housed in a 50 by 60-foot Butler building. Inside this building there will be a 42-foot diameter dome 26 feet high at the center.

Internal construction. In order to minimize light deflection the interior of the hemispherical dome is to be lined with a special black honeycomb panel constructed of black paper. The cells are about ½ inch across the flats and 4 inches deep. The first or outer inch of the honeycomb is painted glossy black, the bottom 3 inches are flat black. The open black cell represents 97% of the exposed wall area. Some light is reflected from the remaining 3% which is the edge area. Experimental activity is underway in effort to reduce this residual reflection in an effort to get nearer to 100% absorption of impinging light.

The honeycomb panels are mounted on black coffin cloth and backed up structurally by being cemented to ¾-inch thick plywood sheets. This material is in 4- by 8-foot sections. Other types of light absorbing materials were tested singly and in combination. None could match the effectiveness of the honeycomb structure.

The corners of the building will house, respectively, a control room, a laboratory, an observation room, and a room housing air conditioning equipment. Inside the room will be two ladder type structures that will provide a means by which a light system simulating a planet or a star can be located at any desired radial position about the spacecraft simulator. The support is a fabricated steel half arch 20 feet in radius. It is attached by wheels to a 40-foot diameter track on the floor and a 3½-foot diameter track directly above the spacecraft simulator. The support is 20 inches wide with wheel tracks on each side. A movable 20-in.² plate is mounted to the support by a system of wheels fitted into the side tracks. The 20-in.² plate to which light sources can be mounted is controlled by a system of pulleys and cables. It can be positioned at any point along the support by a hand winch and can be locked in place. The entire structure is painted with black camouflage to minimize light reflection.

Two of the supports are available in the celestial simulator laboratory which permits simultaneous simulation of two star fields or planets of different intensity and different locations in the hemisphere. The two support structures will be centered about the spherical air bearing that supports the spacecraft simulator.

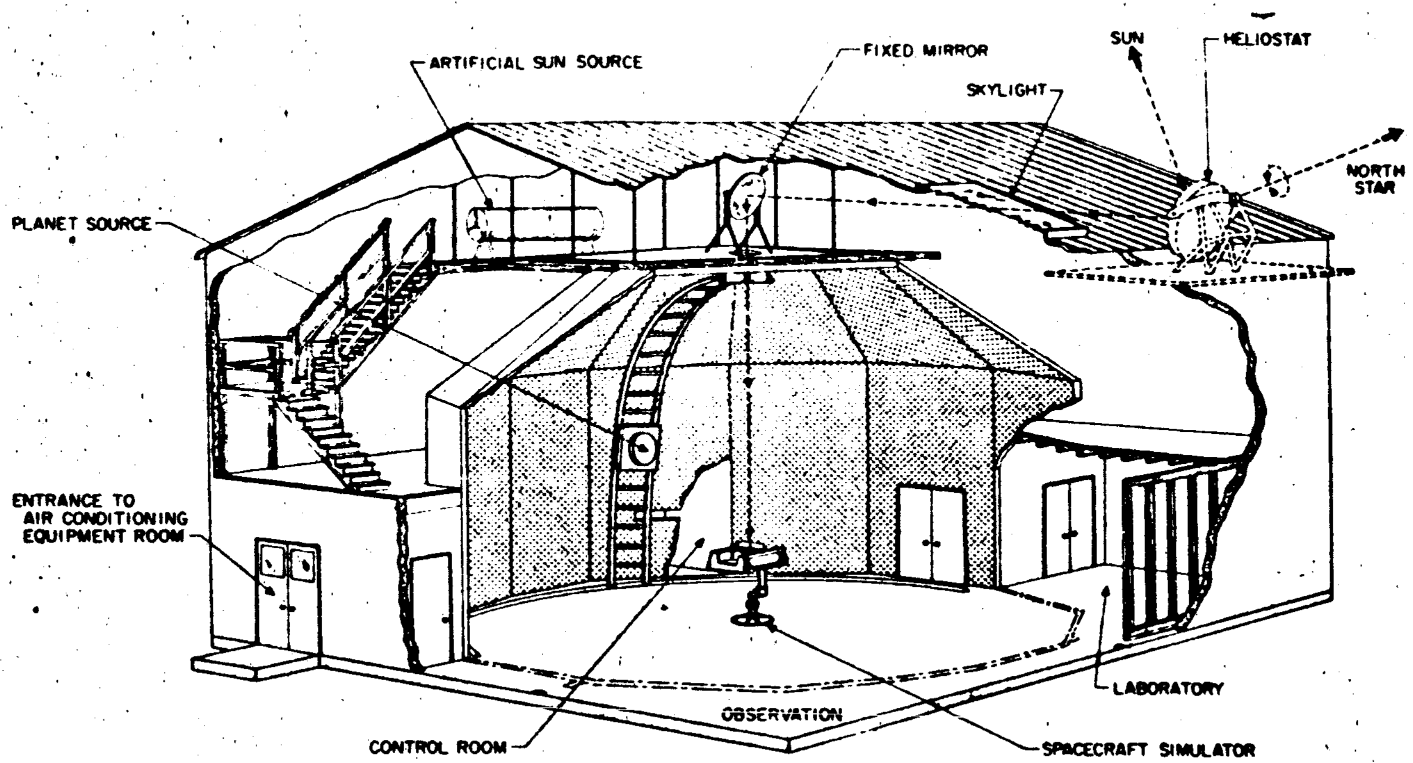

Figure 41. Celestial simulator laboratory

The spacecraft simulator previously described in *SPS 37-4* will be mounted on an isolated concrete slab on the floor in the center of the dome. It has been undergoing testing and minor modifications in preparation for testing the *Ranger* RA-1 attitude control system.

Balance system. The automatic servo balance system has been breadboarded and tested (Fig 42). After coarse manual balancing, it is possible to fine balance the platform to less than 5 cm-gm in all three axes in the horizontal and vertical positions in less than 5 minutes. This operation requires two men working 2 to 3 hours if done manually. An improved version of the servo balance system has been built using gyros of higher accuracy and increased sensitivity. The electronic packaging has been improved and it should now be possible to obtain a finer balance than was accomplished with the breadboard system. Figure 43 displays the electronics package for the gyros and the servo amplifiers. Figure 44 shows the motor driven lead screw that positions the balance weight. One motor-lead screw-weight assembly is required for each axis.

The power supply which consists of the two battery packs, static inverter, and transformer-rectifier-filter package; the six-channel command receiver and the telemetering transmitter; and the servo balance system is considered as a permanent part of the simulator which is to be used as a laboratory test facility. The first control system under test will be the *Ranger* attitude control system. Figure 45 shows the cold gas actuator system that has been designed to represent flight type *Ranger* hardware. The micro-jet actuators are designed to operate in atmosphere at a regulated pressure of 50 psi providing a thrust of 3 to 3.5 grams depending upon the axis. These low thrust forces produce angular acceleration of the simulator of 2×10^{-4} rad/sec.^{2} The tanks have their volumes matched to 0.07% and are symmetrically placed about the center of rotation of the platform to eliminate mass unbalance as the tanks depressurize.

Sensors. The sensors to be used on the simulator will be essentially the same as used on the *Ranger* spacecraft. Four primary sun sensors will be mounted on the top of the simulator for the pitch and yaw axis. There will be no antenna drive aboard the simulator; therefore, the earth sensor will be body fixed to the simulator and will provide signals for control of the roll axis. Flight type low-damped Minneapolis-Honeywell gyros will be used as sensors during the early phases of sun and earth acquisition.

Air bearing. As tests were performed on the spacecraft simulator it became evident that some means of holding the simulator fixed and then releasing it without imparting any disturbing torques would be required. The spherical air bearing of the simulator pedestal permits the nylon ring to be raised to contact the sphere and provide

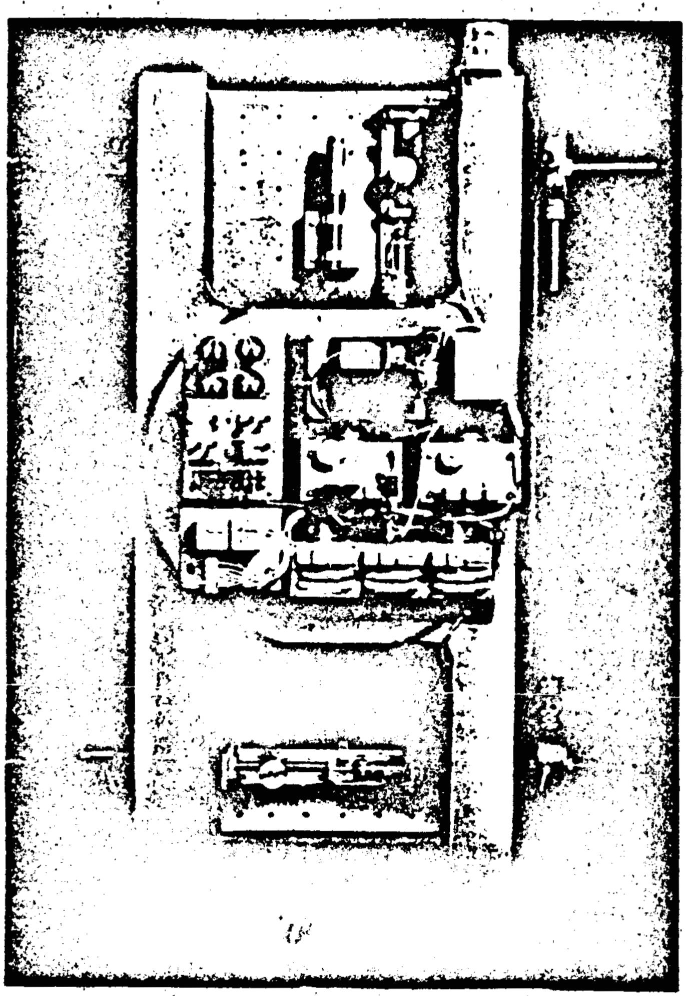

Figure 42. Automatic balance system

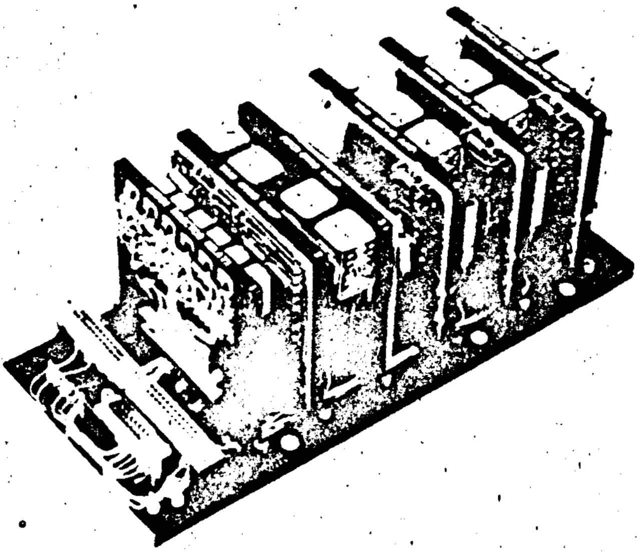

Figure 43. Balance electronics

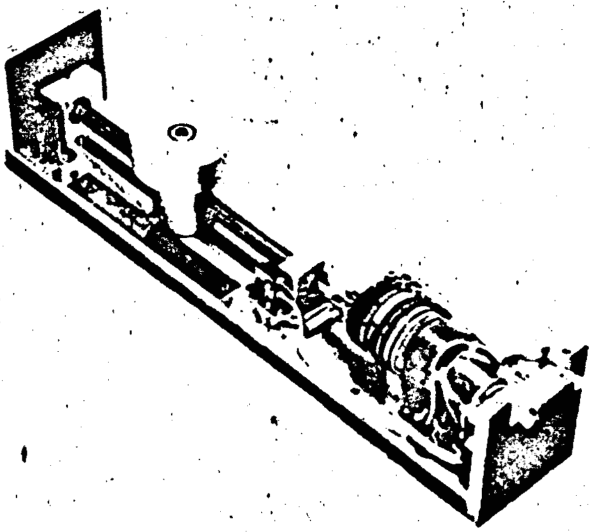

Figure 44. Balance mechanization

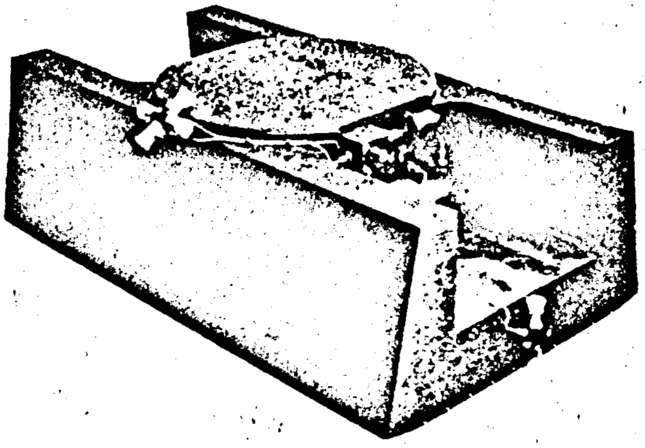

Figure 45. Cold gas actuator system

a friction brake while the simulator is floating on its air bearing. The ring can also be moved away from the sphere to release the simulator.

Another problem encountered during test was the presence of torque setup in the gas bearing. It is felt that this torque is due to an unsymmetrical gas flow between sphere and pad. If the top plane of the pad is not level or if the surface of the sphere or pad is not truly spherical, the sphere can move off the center of the pad and permit uneven flow of gas around the sphere, thereby creating bearing torque. To correct for this, reference levels are being installed on the pedestal to permit accurate leveling of the pad. A multiple orifice pad has been designed which will provide a bearing with increased lateral stiffness.

Heliostat. Extending vertically downward from overhead will be a 24-inch diameter sun beam bundle. This will be provided either by a heliostat reflecting the real sun or by an artificial sun source. The heliostat is composed of two 36-inch diameter mirrors (Fig 46). One of the mirrors is fixed with respect to the building. It is mounted so that its face makes an angle of 45 degrees with the local vertical. The other mirror is movable with two degrees of freedom.

An analysis of the heliostat was made to determine the motions required of the movable mirror. The movable mirror is mounted so that it can rotate about either of two axes. One axis of rotation is parallel to the earth's axis and will be called the hour axis. The other axis of rotation is perpendicular to and moves with the hour axis. This second axis is called the declination axis.

Let the center of a coordinate system be chosen at the center of the movable mirror. Let a right-handed mutually orthogonal system of axes be designated by $\bar{i}$, $\bar{j}$ and $\bar{k}$. The $\bar{i}$, $\bar{j}$, $\bar{k}$ system is fixed with respect to the earth. The unit vector $\bar{i}$ points in an easterly direction, the unit vector $\bar{j}$ points in a northerly direction, and the unit vector $\bar{k}$ lies along the local vertical. Let ϕ denote the latitude angle of the position of the heliostat on the earth. Designate another right-handed mutually orthogonal system of axes by $\bar{r}_1$, $\bar{r}_2$, and $\bar{r}_3$. The unit vector $\bar{r}_2$ lies in the $\bar{j}\,\bar{k}$ plane at the angle ϕ with the $\bar{j}$ axis (Fig 47). The $\bar{r}_1$, $\bar{r}_2$, $\bar{r}_3$ system rotates about $\bar{r}_2$ such that the sun always lies in the $\bar{r}_2\,\bar{r}_3$ plane. It is assumed here that the radius of the earth can be neglected. This rotation nullifies the earth's rotation. In the noontime position the unit vectors $\bar{j}$, $\bar{k}$, $\bar{r}_2$, $\bar{r}_3$, and the sun lie in the same plane. The rotation from the noontime position is denoted by θ. Let the ray from the sun which strikes the center of the movable mirror be represented by the unit vector $\bar{S}$. The vector $\bar{S}$ will lie in the $\bar{r}_2\,\bar{r}_3$ plane at all times. Let α be the angle between $\bar{r}_3$ and $\bar{S}$. Hence

$$\bar{S} = \sin\alpha\,\bar{r}_2 + \cos\alpha\,\bar{r}_3$$

The reflected ray from the center of the movable mirror must lie in the $-\bar{j}$ direction in order to intercept the center of the fixed mirror. The reference axes have been chosen such that $\bar{r}_2$ coincides with the hour axis of the movable mirror.

The perpendicular to the face of the movable mirror must always bisect the angle between $-\bar{j}$ and $\bar{S}$. Letting

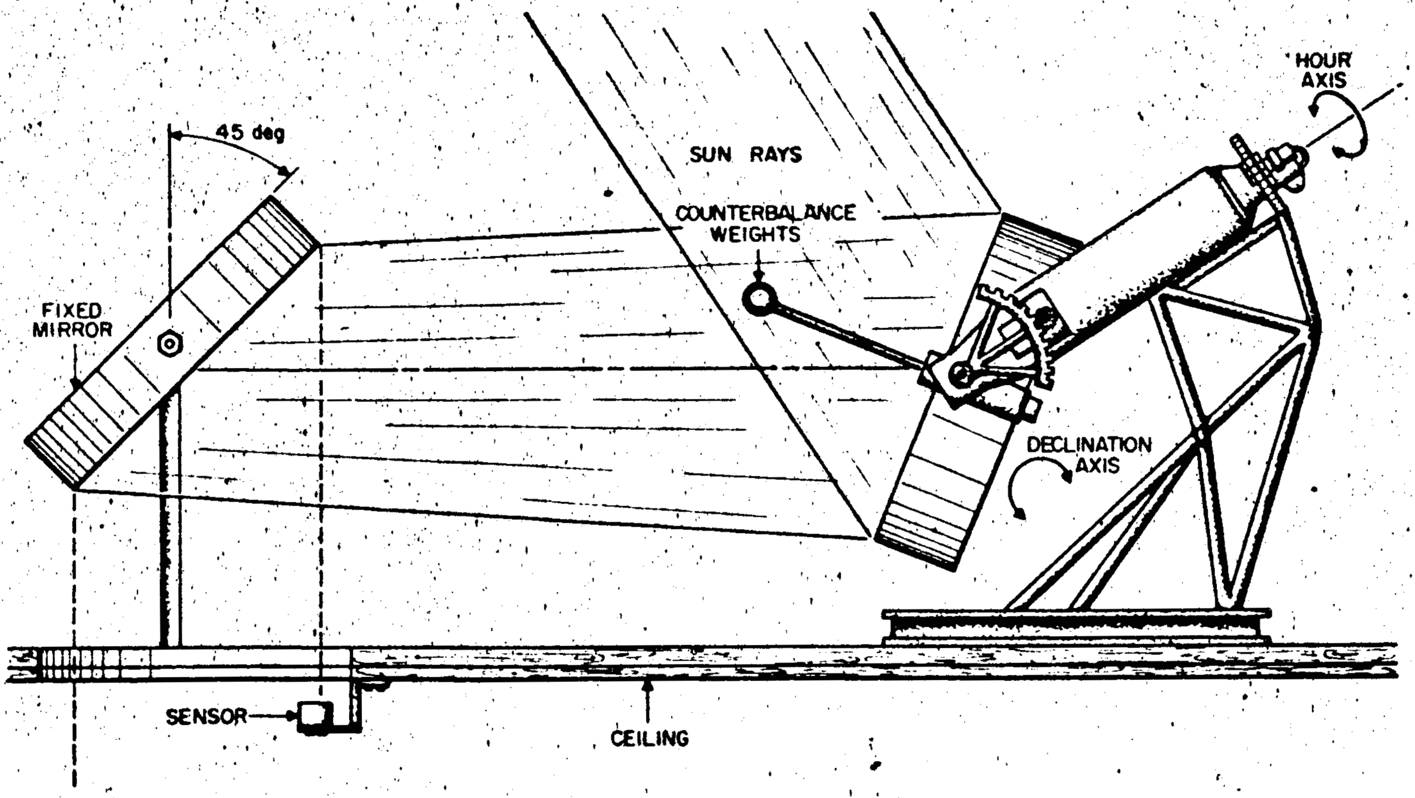

Figure 46. Heliostat

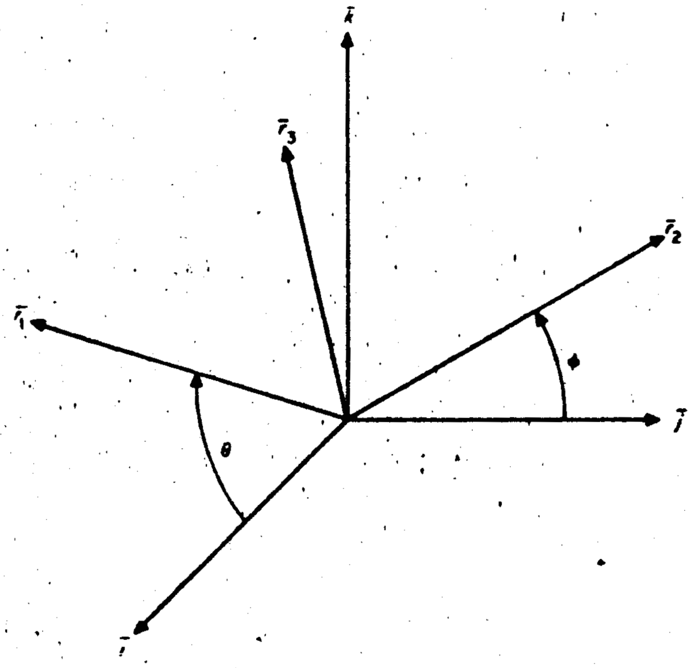

Figure 47. Heliostat coordinate system

the vector $\overline{P}$ lie in the direction of the perpendicular to the mirror

$$\overline{P} = -\overline{j} + \overline{S}$$

By expressing $\overline{S}$ in the $\overline{i}, \overline{j}, \overline{k}$ system, $\overline{P}$ is found to be

$$\overline{P} = -\cos\alpha\sin\theta\,\overline{i} + [-1 + \sin\alpha\cos\phi - \cos\theta\sin\phi\cos\alpha]\,\overline{j} + [\sin\alpha\sin\phi + \cos\theta\cos\phi\cos\alpha]\,\overline{k}$$

Let the direction of the declination axis be given by $\overline{DA}$. Since $\overline{DA}$ is perpendicular to both $\overline{r}_2$ and $\overline{P}$ it follows that

$$\overline{DA} = \overline{r}_2 \times \overline{P}$$

By expressing $\overline{P}$ in the $\overline{r}_1, \overline{r}_2, \overline{r}_3$ system the above cross product gives

$$\overline{DA} = [\cos\theta\sin\phi + \alpha]\,\overline{r}_1 + [-\sin\theta\sin\phi]\,\overline{r}_3$$

The rotation, η, of the mirror about the hour axis is

$$\eta = \theta + \tan^{-1}\frac{-\sin\theta\sin\phi}{\cos\theta\sin\phi + \cos\alpha}$$

Differentiating η with respect to time to obtain the angular velocity of the mirror about the hour axis

$$\frac{d\eta}{dt} = \frac{d\theta}{dt}\left[1 - \frac{\sin^2\phi + \cos\theta\sin\phi\cos\alpha}{\sin^2\phi + 2\cos\theta\sin\phi\cos\alpha + \cos^2\alpha}\right]$$

Plots of η and $d\eta/dt$ as functions of θ are shown in Figures 48 and 49. For convenience a time scale is also given where the noontime position is taken to be the instant at which $\theta = 0$.

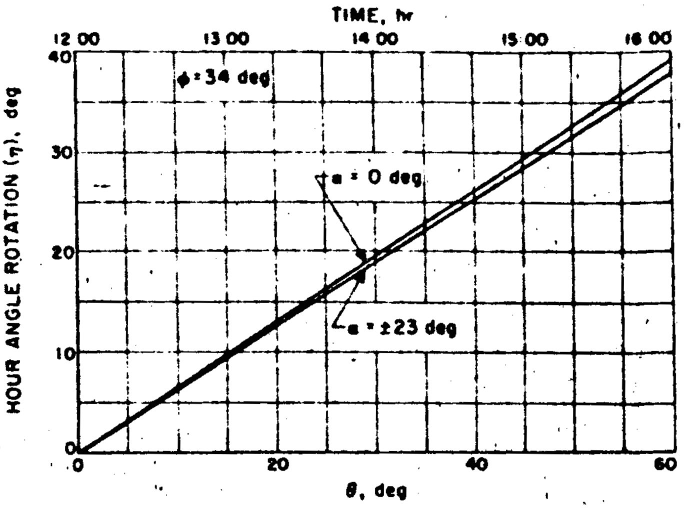

Figure 48. Rotation about hour axis

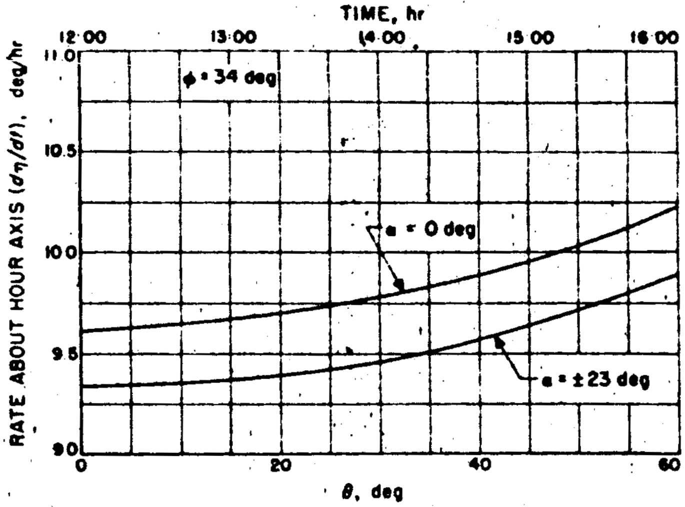

Figure 49. Rate about hour axis

Assuming the system is to be in operation from 8:00 am to 4:00 pm, during any 1-year period the maximum mirror speed necessary about the hour axis is 10.23 deg/hr and the minimum speed is 9.34 deg/hr. Hence, the mean speed is 9.78 deg/hr and the maximum variation from this speed is 4.5%.

The motion of the mirror about the declination axis must also be determined. A unit vector $\overline{\rho}$ in the $\overline{P}$ direction expressed in the $\overline{r}_1, \overline{r}_2, \overline{r}_3$ system is

$$\overline{\rho} = \sqrt{2}(1 - \sin\alpha\cos\phi + \cos\theta\sin\phi\cos\alpha)^{-\frac{1}{2}}[\sin\theta\sin\phi\,\overline{r}_1 + (\sin\alpha - \cos\phi)\,\overline{r}_2 + (\cos\theta\sin\phi + \cos\alpha)\,\overline{r}_3]$$

Let the angle between $\overline{r}_2$ and $\overline{\rho}$ be denoted by δ. This is indicated in Figure 50 where the system is shown in the

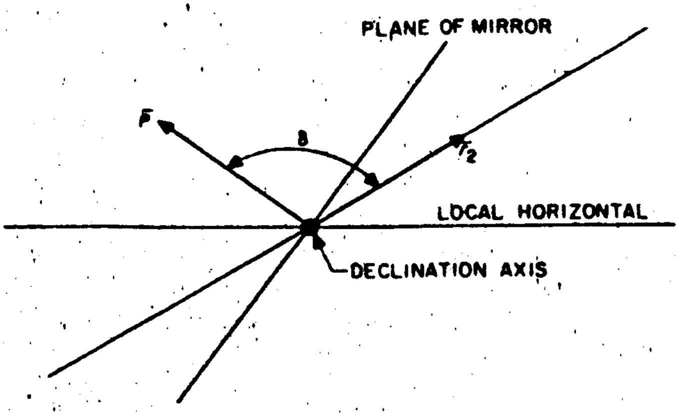

Figure 50. Definition of δ

noontime position. The coefficient of $\bar{r}_2$ in the $\bar{\rho}$ vector is the direction cosine. Hence

$$\delta = \cos^{-1} \frac{\sin\alpha - \cos\phi}{\sqrt{2}\,(1 - \sin\alpha\cos\phi + \cos\theta\sin\phi\cos\alpha)^{1/2}}$$

The angular velocity of the mirror about the declination axis is found by differentiating δ with respect to time.

$$\frac{d\delta}{dt} = -\frac{1}{2\sqrt{2}}\left\{\frac{(\sin\alpha - \cos\phi)(\sin\theta\sin\phi\cos\alpha)}{(1 - \sin\alpha\cos\phi + \cos\theta\sin\phi\cos\alpha)}\right.$$

$$\left.\times \frac{1}{[1 - \sin\alpha\cos\phi + \cos\theta\sin\phi\cos\alpha - 0.5(\sin\alpha - \cos\phi)^2]^{1/2}}\right\}\frac{d\theta}{dt}$$

Plots of δ and $d\delta/dt$ as functions of θ and time are shown in Figures 51 and 52.

It has been decided to use a servo system to drive the movable mirror (Fig 53). A sensor (error detector) placed below the fixed mirror gives a signal which is proportional to the angle between the reflected light beam and a vertical line. The sensor resolves this error into two components. One component is along an east-west axis and the other along a north-south axis. For each controlled axis of the mirror the error signal is integrated. The signal from the integrator is used to drive a voltage controlled oscillator (VCO). The frequency of the VCO determines the speed of a synchronous motor that moves the mirror about one axis.

A voltage controlled oscillator has been developed for use in the heliostat control loop. The circuit is a balanced multivibrator with the operating frequency controlled by an RC network. Preliminary tests at room temperature indicate that the long term frequency stability at room temperature is better than 1%, without selection of the control resistors and capacitors. Frequency stability should be greatly improved by utilizing balanced components. The frequency range of the oscillator is ±800 cps around the nominal frequency of 1200 cps. The transfer sensitivity of the oscillator is 100 cps/v(dc). Frequency dividers and a passive filter will couple the oscillator to the amplifier-drive motor.

The sun sensor used as the error detector in the control loop is a very simple device with no moving parts. It has a four element fully color corrected achromatic lens which reduces the sun image and projects it on a solar silicon cell which is divided into four quadrants.

Two types of coupling between the hour axis and declination axis exist in the heliostat. The first type is caused by the relative positions of the two mirrors. This is the condition that as the mirror moves about the hour axis, a motion about the declination axis is necessary to keep the reflected ray from the movable mirror directed toward the fixed mirror.

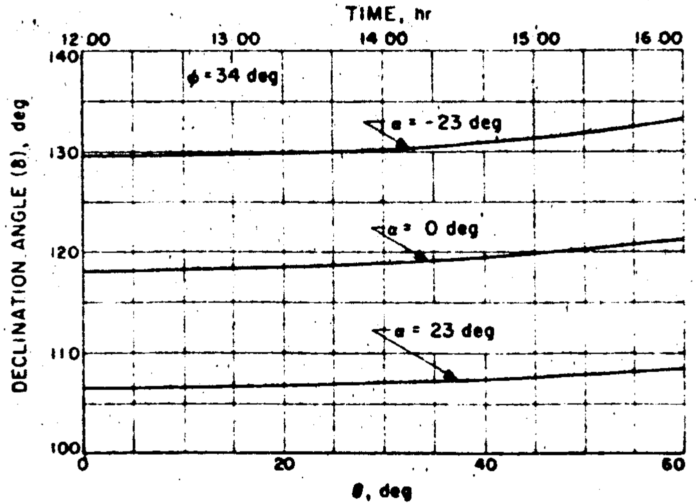

Figure 51. Declination angle.

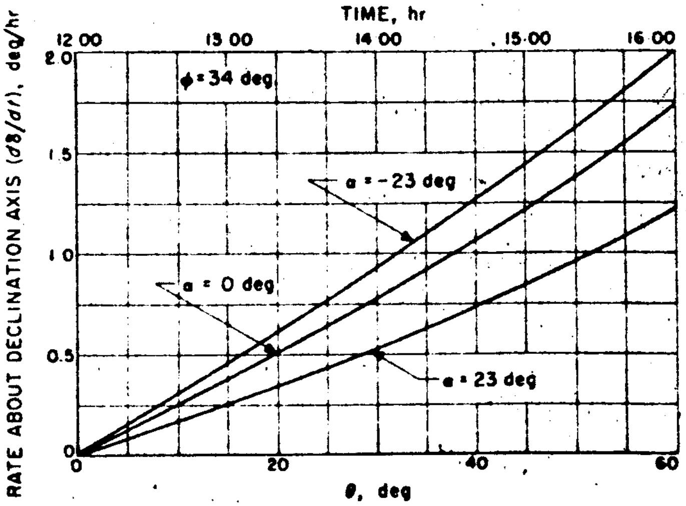

Figure 52. Rate about declination axis

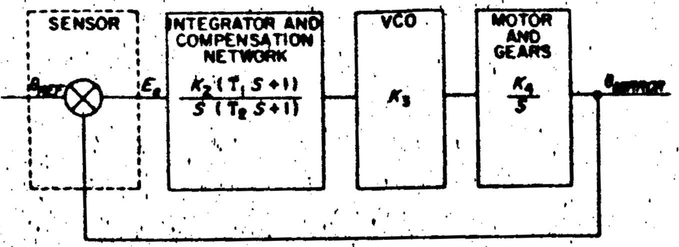
SENSOR
INTEGRATOR AND COMPENSATION NETWORK
VCO
MOTOR AND GEARS
θ_{REF}
E_e
$\frac{K_2(T_1S+1)}{S(T_2S+1)}$
K_3
$\frac{K_4}{S}$
θ_{MIRROR}

Figure 53. Single axis control loop

The second type of coupling arises in the control system of the mirror drives (Fig 54). In the noontime position a motion of the mirror about the declination axis produces an error only in the north-south sensor axis and a motion about the hour axis produces an error only in the east-west sensor axis. However, this is true only at noontime; i.e., when $\theta = 0$. At any other instant a motion about either the hour axis or the declination axis gives rise to an error signal in both the east-west and north-south sensor axes. If the sensor axes were rotated about a vertical line this type of coupling could be eliminated.

An analysis was made to determine the rotation μ of the sensor axes that would be necessary to eliminate the coupling in the control system. For an arbitrary position of the movable mirror let the reflected ray to the fixed mirror be denoted by

$$\bar{M} = D\bar{i} + E\bar{j} + F\bar{k}$$

when η and δ have the correct values both D and F vanish. For some small change $\Delta\delta$ in the declination angle from this nominal position the coefficients of the $\bar{i}$ and $\bar{k}$ terms of $\bar{M}$ become ΔD and ΔF, respectively (Fig 55).

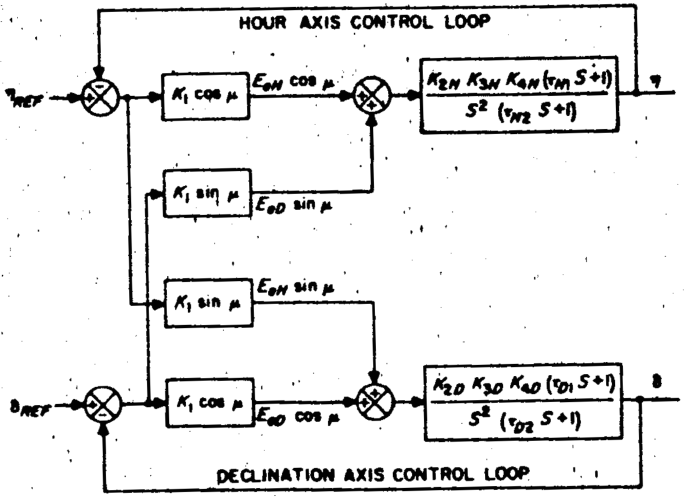
HOUR AXIS CONTROL LOOP
η_{REF}
$K_1 \cos\mu$
$E_{eH}\cos\mu$
$\frac{K_{2H}K_{3H}K_{4H}(\tau_{H1}S+1)}{S^2(\tau_{H2}S+1)}$
η
$K_1 \sin\mu$
$E_{eD}\sin\mu$
$K_1 \sin\mu$
$E_{eH}\sin\mu$
δ_{REF}
$K_1 \cos\mu$
$E_{eD}\cos\mu$
$\frac{K_{2D}K_{3D}K_{4D}(\tau_{D1}S+1)}{S^2(\tau_{D2}S+1)}$
δ
DECLINATION AXIS CONTROL LOOP

Figure 54. Two axis control with coupling

Then μ can be represented by

$$\mu \doteq \tan^{-1}\frac{\Delta D}{\Delta F}$$

for ΔD and ΔF small. Let

$$\gamma = \theta - \eta$$

and

$$\sigma = \delta - 90 \text{ deg}$$

For small changes in the declination angle about the nominal position the expression for μ

$$\mu = \tan^{-1}\frac{\frac{\partial D}{\partial \sigma}}{\frac{\partial F}{\partial \sigma}}$$

where

$$\begin{aligned}\frac{\partial D}{\partial \sigma} = &- \sin 2\gamma \sin 2\sigma \cos\theta \cos\alpha \\ &+ 2\cos 2\sigma \sin\alpha \sin(\theta - \gamma) \\ &+ 2\sin\theta \cos\alpha \cos^2\gamma \sin 2\sigma\end{aligned}$$

and

$$\begin{aligned}\frac{\partial F}{\partial \sigma} = &- 2\cos 2\sigma \sin\alpha \cos\phi \cos(\theta - \gamma) \\ &- 2\sin 2\sigma \cos\alpha \cos\phi \cos(\theta - \gamma)\cos\gamma \\ &+ 2\sin 2\sigma \sin\alpha \sin\phi \\ &- 2\cos 2\sigma \cos\alpha \sin\phi \cos\gamma\end{aligned}$$

Both $\partial D/\partial\sigma$ and $\partial F/\partial\sigma$ are evaluated in the nominal position. A plot of μ versus θ or time is shown in Figure 56. For this plot the values used for α and ϕ were $\alpha = -23$ degrees and $\phi = 34$ degrees. The effect of this type of coupling is being investigated on the analog computer. The system is represented by a linear model. Preliminary results indicate the performance of the control system is satisfactory without compensating for this coupling.

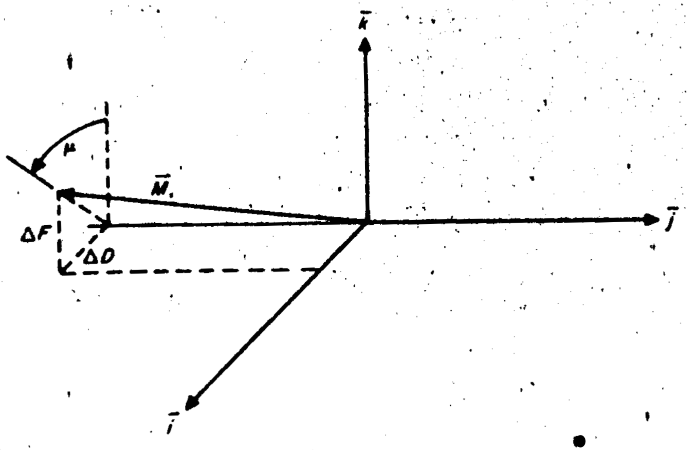
$\bar{k}$
$\bar{i}$
μ
$\bar{M}$
ΔF
ΔD
$\bar{j}$
$\bar{i}$

Figure 55. Definition of μ

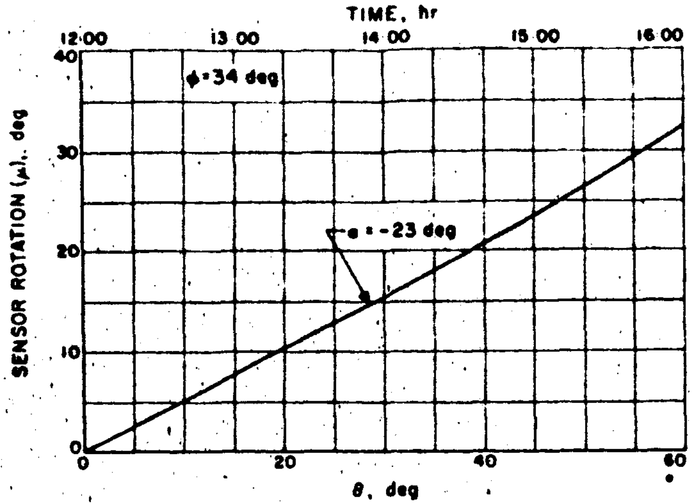

Figure 56. Sensor relation to uncoupled control axis

Artificial sun source. The artificial sun source will consist of a reflective optical system collimating the crater of a high-intensity carbon arc light. The lamp will be operated by a 225-ampere 115-volt direct current source.

The surface brightness of the sun is approximately 104,000 lumens/cm²/sterad. To stimulate both the angular diameter and flux of the sun at some specified distance, the source of radiation in the simulator must have a surface brightness at least as high as the sun. Preferably it should be higher, to compensate for losses within the optical system. At present, the best source seems to be a high-intensity carbon arc having a color temperature of 5800°K and a surface brightness of 71,000 lumens/cm²/sterad. Therefore, it will not be possible to simulate both the angular diameter and flux of the sun.

In order to attain an artificial sun source which is both compact and efficient, it is desirable to use reflective optics. A proposed design is an off-axis ellipsoidal condensing mirror, an aperture at the secondary focus, and an off-axis paraboloidal collimating mirror (Fig 57). The cone of radiation falling upon and passing through the aperture is an elliptical cone, due to the off-axis ellipsoid. The *f*-ratio in the plane is greater than the *f*-ratio perpendicular to that plane. In other words, the major axis of the elliptical cross section of the cone is perpendicular to the plane. It can be shown that this ellipticity can be removed by the correct tilt of the axis of the paraboloid with respect to the cone, but that for the design given, only at an angle that the collimated beam will not clear the aperture. Therefore, the paraboloid will be designed to work just off-axis (about 1 deg) to allow a clearance of the beam of about 1.7 inches when passing the aperture.

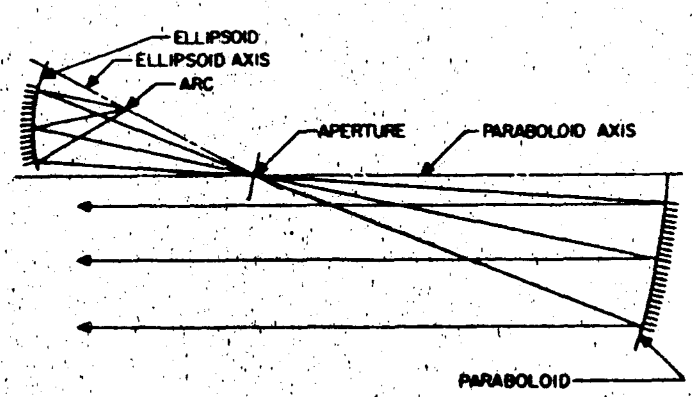

Figure 57. Off-axis ellipsoidal condensing mirror

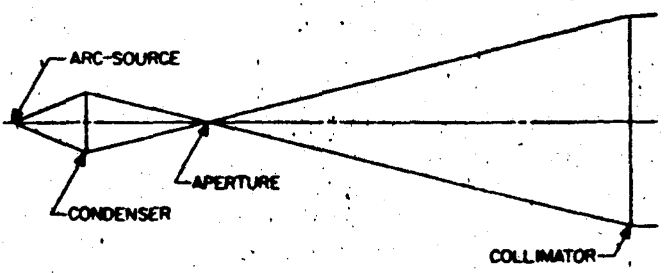

Figure 58. Arc collimation system

In the design being considered (Fig 58) the angle between the positive carbon rod and the ellipsoid axis is 26.222 degrees. The resulting elliptical cone falling on the aperture has an *f*-ratio of 4.00000 perpendicular to the plane of the system, and 4.06494 in the plane. The intersection of this cone with the paraboloid, if the axis of the 14.02869-degree cone is placed 15.02269 degrees from the axis of the paraboloid, will produce a beam which is the elliptical projection of the 24-inch diameter mirror. The dimensions of this elliptical beam will be 24.000 by 23.999 inches, producing an error signal for the polar sun sensors relative to the equatorial sun sensors of 0.001. A position can be found by rotating the sensors about the axis of the beam where this error signal goes to zero.

The angle at which the center of the ellipsoid is off-axis (26.222 deg) was chosen arbitrarily to work as closely on-axis as possible. The physical size of the arc housing may dictate what this dimension must be. The elements for a system with this angle equal to 31.222 degrees have been computed, and the resulting beam is slightly more elliptical, producing an error signal of perhaps 0.003. Again, this can be made to vanish by a proper rotation.

If the center of the 24-inch paraboloid is approximately 8.01 degrees off-axis (depending on the design) the distance from the center of the aperture to the center of the mirror, assuming an axial focal length of 96 inches, is

96.8102 inches. It is this distance that is used to determine the necessary aperture size. To obtain an angular diameter of 44.22 minutes of arc $d_{aperture} = 96.8102 \times \tan (44.22 \text{ min}) = 1.245$ inches. The basic elements of the proposed design are shown in Table 13.

Table 13. Proposed condensing and collimation system parameters

Parameter	Value
Condensing system	
Arc diameter	0.591 in.
Center of ellipsoidal mirror	26.222 deg off-axis
Diameter of ellipsoidal mirror	4.704 in.
Axis of elliptical cone	11.135 deg off-axis
Elliptical cone	14.027 deg
Diameter of aperture	1.245 in.
Distance, center of arc to center of ellipsoidal mirror	10.000 in.
Distance, center of ellipsoid to center of aperture	13.880 in.
Semi-major axis of ellipsoid	16.6375 in.
Eccentricity of ellipsoid	0.41714 in.
Collimating system	
Axial focal length of paraboloid	96.000 in.
Diameter of collimating mirror	24.000 in.
Center of mirror	8.013 deg off-axis
Distance, center of aperture to center of mirror	
Beam dimensions	24.000 × 23.999 in.
Center of aperture by 13.688 in.	

This design summary represents the dimensions of the initial design effort. Detail design of the collimation and condensing systems may require some changes in order to allow for mechanical clearances. The artificial sun source will be equipped with two arc light elements mounted in tandem arrangement. As one nears the end of its burning time (40 min) the other may be started, then pushed into position. This transfer will cause a light interruption of approximately 1 second. The lamp elements will travel on a guide rail.

Instrumentation. Instrumentation for the celestial simulation facility initially will consist of a communications system for the spacecraft simulator made up of two eight-channel on-off type command systems and a single seven-channel analog telemetry system, a monitoring theodolite for use in performing initial alignments and to make azimuth measurements as the tests proceed, and recording equipment to provide facility for recording desired data.

Command system. The command system is composed of two AM transmitters with eight audio tone generators in each unit used to modulate the respective transmitters. Each transmitter is capable of being modulated by two simultaneous audio tones. Therefore at the present time, there is the capability of sending four simultaneous on-off type commands and the over-all capability of performing 16 different on-off control functions on the spacecraft simulator. The receivers for the command system are mounted to the spacecraft simulator and are crystal controlled superheterodyne units.

Telemetry system. The telemetry system consists of seven voltage controlled oscillators and an AM transmitter as the sending unit on the spacecraft simulator and a superregenerative receiver with seven phase-locked discriminators as the information processor on the ground. The telemetry system has the capability of sending seven analog signals from the simulator and receiving them on the ground with an accuracy of approximately 1%. The over-all capability can be extended by using the command system to sample various signal inputs to the telemetry system on the spacecraft simulator and thus increase the total number of measurements.

B. Guidance and Control

The functional design of the guidance and control subsystems for the *Ranger* spacecraft program can be conveniently divided into two parts. The first part is concerned with the guidance and control subsystems for the first two flights which are intended as development tests of the basic spacecraft. The second part is concerned with the guidance and control subsystems for the last three flights which are planned as lunar rough-landing attempts, using the spacecraft plus a landing capsule. The following material describes work accomplished in the above areas during this report period.

1. Ranger RA-1 and -2

a. Sun sensors. Sun sensors for the *Ranger* program have been developed to a high degree of accuracy and reliability. RA-1 units have been flight acceptance tested and delivered to the attitude control system.

The sun sensors are optical devices which utilize a shadowing technique to develop error signals on two orthogonal axes. The sensors are divided into primary and secondary units. The primary units mount on the spacecraft frame and aid in determining the roll axis. The secondary units mount on the underside of the solar panel tips and complete the spherical field of view requirements during acquisition of the sun.

The problem of mounting the sun sensor detector has been solved by employment of quad-rings. The quad-rings bring support to bear on the strongest section of the glass detector envelope rather than complete support as provided by the potting compound. With ultilization of the quad-ring mounting, a sun sensor assembly can survive an extreme temperature range from −100 to +125°C without failure.

The primary sun sensor detector has been changed to cadmium sulphide (from cadmium selenide). Cadmium sulphide has a high temperature coefficient of resistance and a low hysteresis value. The sun sensor error analysis presented in *SPS 37-5* showed that a significant error could be caused by an asymmetrical temperature. This error is directly related to the detector temperature coefficient of resistance. A re-evaluation of sun sensor performance is presently being made.

b. Earth sensor. Earth sensor mechanization is much the same as the sun sensor in that a variable aperture (shadowing) technique is used. The detectors are three photomultiplier tubes (¾ in. diameter) arranged so that their outputs can be resolved into two-axis error signals (*SPS 37-5*).

Since last reporting, the earth sensor electronics have undergone several modifications to improve loop stability. These modifications have been effective and, at the present time, six earth sensors are operating satisfactorily. The RA-1 flight earth sensor has passed its flight acceptance tests and has been delivered to the attitude control system. Flight acceptance temperature has been changed to a nominal of 20 ±25°C for these units. Tests have shown the photomultiplier tubes can only survive 72°C non-operating and 45°C operating temperature. Exceeding these values produces a rapid and irreversible change in gain.

A backup design is being carried along concurrently with the hope that it can be included in *Ranger* RA-3, -4, and -5. This design (Fig 6) excites the photomultiplier tubes with pure dc instead of the dc and ac ripple presently used. Tests have shown that dc excitation improves photomultiplier gain stability. Therefore, the dc model should have improved null stability and threshold characteristics. The present dc model is in initial stages of development; however, preliminary tests on the modulator and preamplifier sections are very encouraging. The excitation to the tubes is filtered dc, giving dc outputs. These outputs are then mixed and modulated to give the hinge $(A - B)$, roll $(A + B - C)$, and control $(A + B + C)$ outputs. As in the ac version, the control output is used to control the tube excitation.

It is expected that this version will give null offsets of less than 0.5 degree, 3σ, in both axes, and have a sensitivity of 0.001 foot-candle or better.

At present, the electronics have been tested as a breadboard, and perform well from 0 to 100°C. Tests below 0°C show a gradual decrease in scale factors of the hinge and roll outputs. These scale factors are 25% low at −40°C. No testing has been done to date with photomultiplier tubes connected.

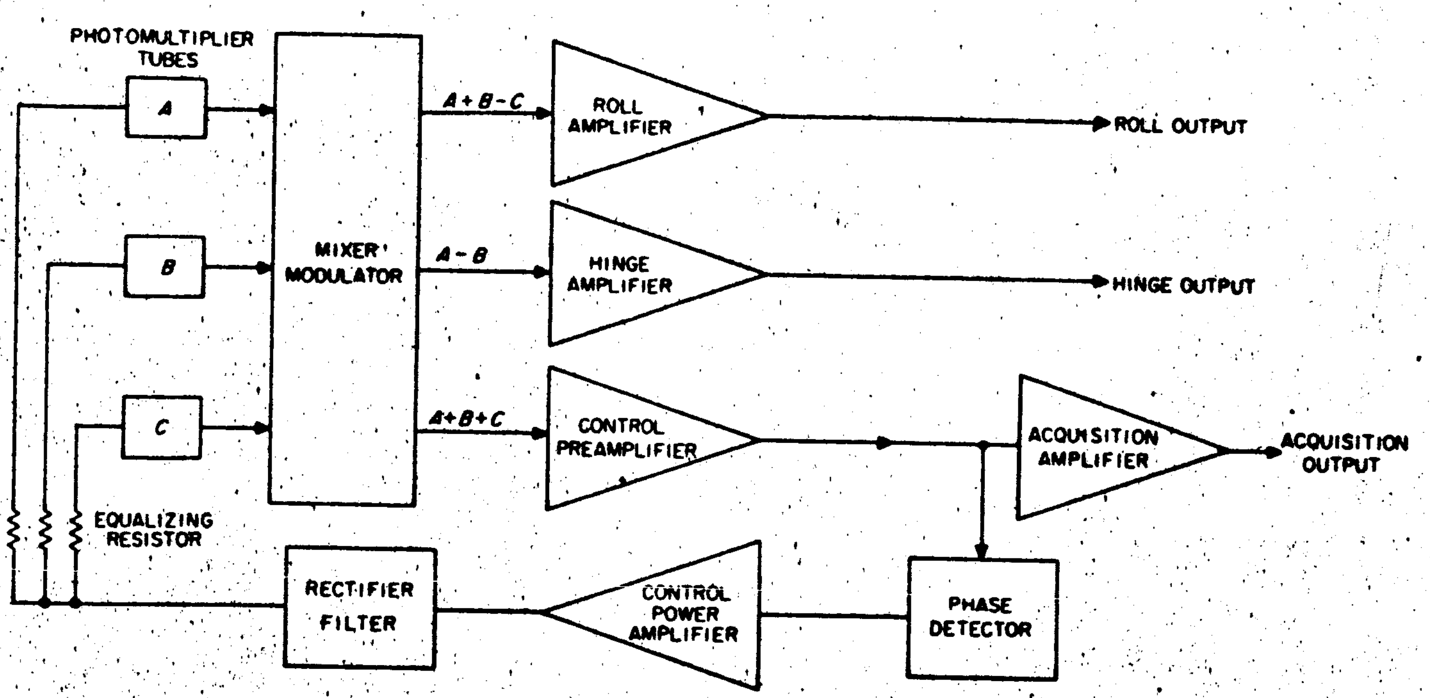
PHOTOMULTIPLIER TUBES
A
B
C
EQUALIZING RESISTOR
MIXER MODULATOR
A+B-C
A-B
A+B+C
ROLL AMPLIFIER
HINGE AMPLIFIER
CONTROL PREAMPLIFIER
ROLL OUTPUT
HINGE OUTPUT
ACQUISITION AMPLIFIER
ACQUISITION OUTPUT
RECTIFIER FILTER
CONTROL POWER AMPLIFIER
PHASE DETECTOR

Figure 6. Earth sensor

3. Electromechanical Devices

a. Horizon scanner. To provide information for orientation of the scientific instruments with respect to the destination planet, a horizon scanner is being developed. The horizon scanner provides two axis error signals to stabilize the scientific platform with respect to the planetary local vertical. An additional output of the horizon scanner may be planet angular diameter from which range data could be derived.

The performance requirements of the scanner are that both the position error signals and the angular diameter information be accurate to 0.1 degree, 1σ. The range of operation is from 8000 to 160,000 km distance from the center of the planets Venus or Mars. In addition, the sun edge planet limb minimum angular separation during tracking can be as small as 6 degrees.

A horizon scanner to meet these requirements is being developed for JPL by the Barnes Engineering Company. This device uses a single thermistor bolometer detector to detect the infrared thermal radiation discontinuity between the planet edge and the space background. This method allows the scanner to be independent of reflected solar radiation and, in fact, the planet can be tracked while the spacecraft is on the dark side of the planet.

The scanning mechanism consists of counter rotating prisms which sweep the ½ by ½ degree field of view of the detector over a 70 degree, four loop rosette pattern. When the scan intercepts the planet a rectangular pulse is generated. The leading and trailing edges of the pulse coincide with the planet edges. Angular position information is derived from the time of the pulse edges with respect to a reference pulse generated by the prism position. This technique of edge or horizon detection enables the accuracy of the device to be independent of thermal gradients across the planet disc. To provide acquisition and sun discrimination, the rosette pattern can be slowly rotated through a small angle when necessary.

b. Long range earth sensor. The long range earth sensor provides two axis pointing information for the purpose of directing the high-gain communications antenna toward the earth. The sensor is attached to the antenna structure and the optical axis of the sensor is boresighted with the antenna axis.

The sensor tracks the earth over the approximate range of 1.6×10^6 to 6×10^7 km by detecting the reflected solar energy of the earth with a single detector. No rotating mechanical parts are used in order to insure high reliability for continuous operation over long periods of time. Scanning of the 4×10 degree field of view to provide the two axis information is accomplished by a vibrating reed. The reed moves an aperture in the image plane of the optical system and modulates the earth's energy incident on the detector. Null accuracy is 0.2 degree, 1σ, in the spacecraft roll axis and 0.3 degree, 1σ, in the antenna hinge axis.

f. Earth sensor. Ranger earth sensor optical mechanization is much the same as the sun sensor in that a variable aperture (shadowing) technique is used.

As reported in *SPS 37-6*, both an (*A-C*) and a (*D-C*) earth sensor are being built. The (*D-C*) version has proved to be a much more sensitive and stable device than the (*A-C*) model and as a consequence will be used for all *Ranger* missions.

During the development period one modification has been made that significantly improved the life characteristics of earth sensor photomultiplier tubes in both

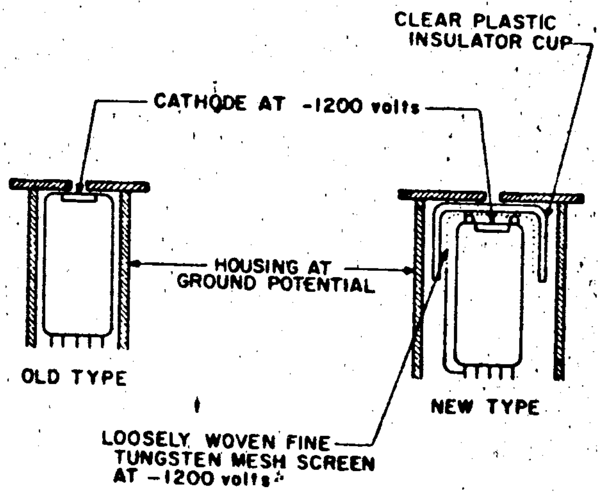
CLEAR PLASTIC INSULATOR CUP
CATHODE AT -1200 volts
HOUSING AT GROUND POTENTIAL
OLD TYPE
NEW TYPE
LOOSELY WOVEN FINE TUNGSTEN MESH SCREEN AT -1200 volts

Figure 18. Earth sensor

versions (*A-C* and *D-C*). This was the addition of an electrostatic shield around the cathode portion of the tube shown in Figure 18. This modification extends the life of the photomultiplier although the exact reason is not presently known. However, it seems likely that very minute currents were flowing in the tube housing causing migration of cesium from critical areas with resultant loss in sensitivity. The shield eliminates a large voltage gradient in the cathode and first dynode area.

f. Horizon scanner. The *Mariner* A scientific experiments are directed toward the destination planet by use of an infrared horizon scanner sensor. This sensor operates on the planet emitted radiation between 5 and 15 micron wavelength using germanium optics and a bolometer detector.

Approximately 200,000 miles from closest planet approach the horizon scanner is activated and a search pattern internal to the scanner begun. After planet acquisition, two-axis error signals are fed from the scanner to the planetary horizontal platform servos in order to direct the platform and its scientific experiments toward the planet. Figure 46 is a photograph of the first prototype horizon scanner. Figure 47 is a cutaway drawing of the horizon scanner.

In attempting to achieve reliability through simplicity of design, it became necessary to reduce the complexity of some of the processing circuitry. This redesign has required the rescheduling of delivery of the first prototype unit from April to May 1961.

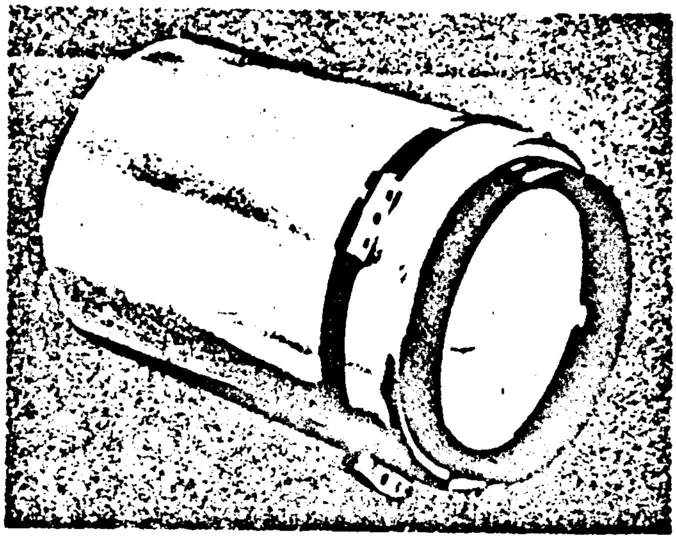

Figure 46. Prototype horizon scanner

The possible sources of errors contributing to the accuracy of the horizon scanner are shown in Table 12.

It is to be noted that the asymmetry in radiance of Mars with its relatively thin atmosphere will be the most

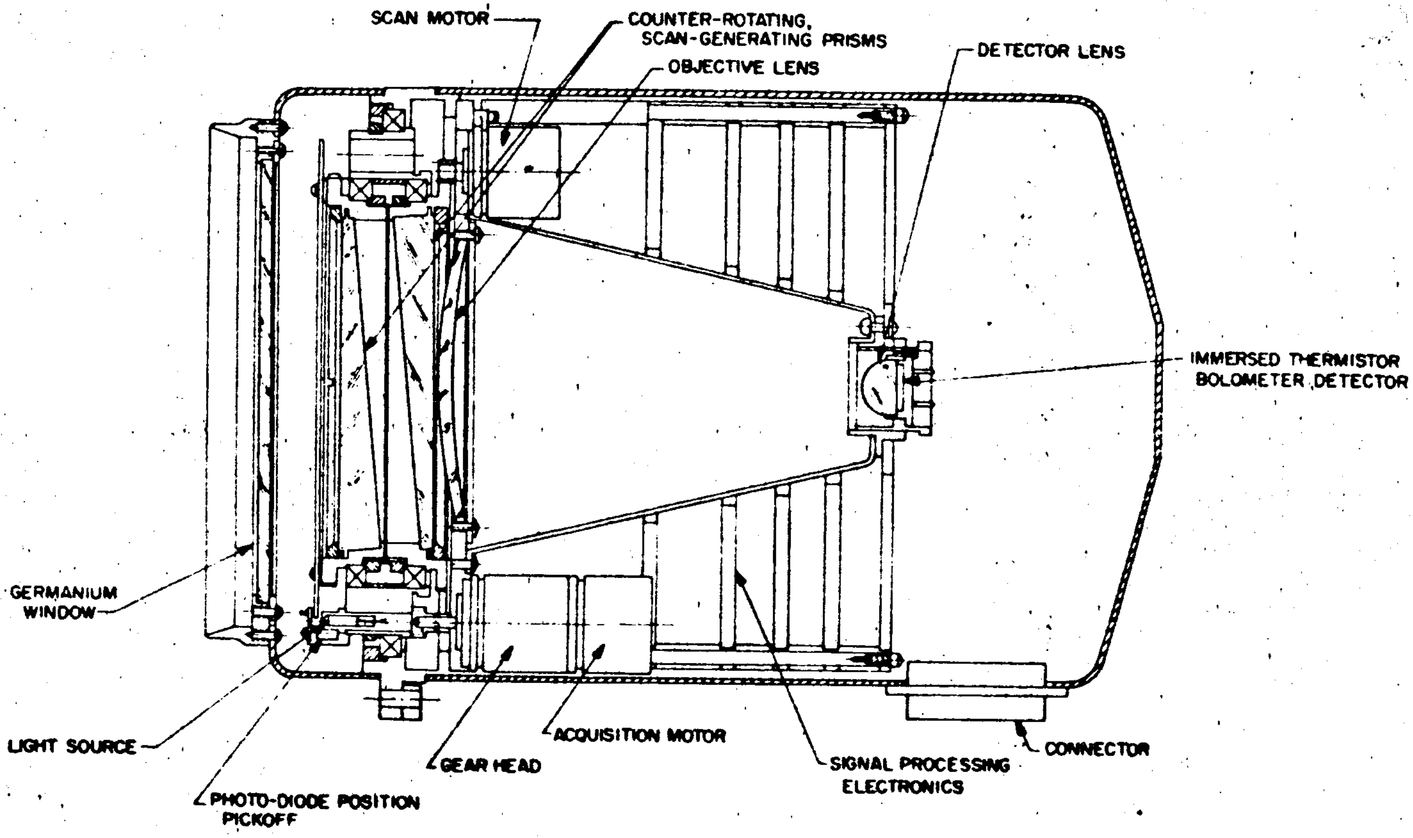
SCAN MOTOR
COUNTER-ROTATING, SCAN-GENERATING PRISMS
OBJECTIVE LENS
DETECTOR LENS
IMMERSED THERMISTOR BOLOMETER DETECTOR
GERMANIUM WINDOW
LIGHT SOURCE
PHOTO-DIODE POSITION PICKOFF
GEAR HEAD
ACQUISITION MOTOR
SIGNAL PROCESSING ELECTRONICS
CONNECTOR

Figure 47. Horizon scanner

Table 12. Horizon scanner error estimates

Mechanical alignment of external reference surfaces and optical axis	±0.02 deg
Stability of wedge position center crossing reference pulse	±0.02 deg
Asymmetrical shift of clipping levels with temperature variation	±0.05 deg
Difference in absolute radiance level*	
Venus	±0.01 deg
Mars	±0.1 deg
Rms of 1σ errors	
Venus	±0.06 deg
Mars	±0.12 deg

*From one limb of planet to the diametrically opposed limb.

significant effect in horizon scanner accuracy. The effect will be a bias toward the solar illuminated portion of the planet.

g. Infrared planet simulator. This simulator is used to test the capabilities of the planet horizon scanner at temperatures ranging from −20 to 60°C. This will allow testing of the scanner through the range of internal temperatures which are expected during flight.

The basic unit is a modified Tenney TTUF-40240 temperature chamber. This forms the scanner compartment as shown in Figure 48. The space background chamber is adjacent to the scanner compartment sharing one wall which is cut through to allow the scanner to see through to the infrared target displayed just beyond the far wall of the space chamber. The aperture in the space chamber wall through which the targets are seen can be varied by choosing one of several annular inserts. This allows presentation of targets ranging from 0.5 to 30 degrees in diameter. Two adjacent targets of different temperature may be presented to simulate a planet terminator. A 1000 C source will also be provided to simulate the sun. This source will be displayed through small holes in the space chamber wall which can be covered when not in use. All three targets are standard infrared sources.

A germanium lens approximately 10 inches in diameter is used to collimate the target energy and also isolates

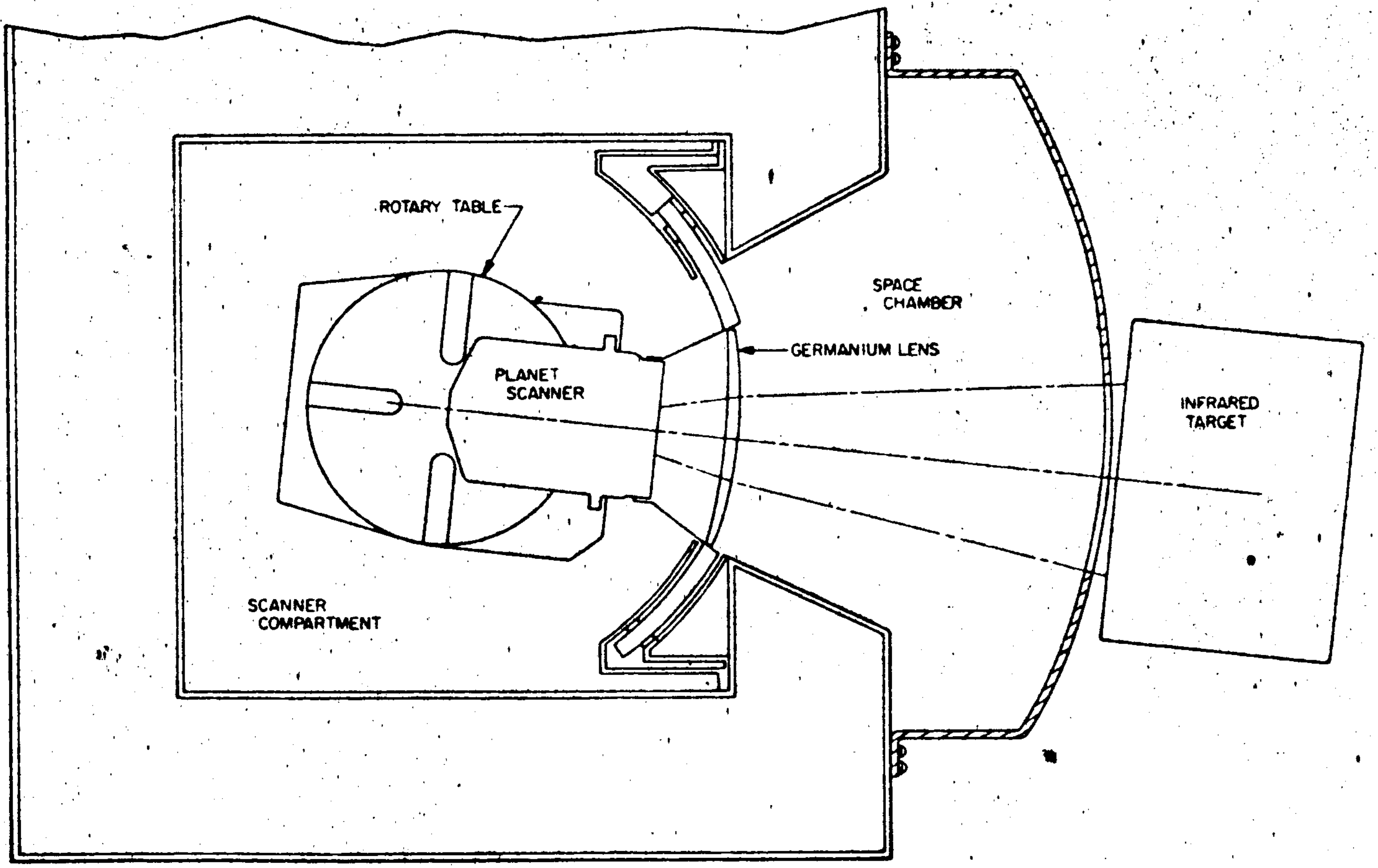

Figure 48. IR planet simulator

the scanner compartment from the space chamber. To simulate off axis targets up to 20 degrees, the scanner and collimating lens may be rotated by means of the rotary table to which they are mounted. A sliding seal which moves with the lens assembly preserves the integrity of each compartment.

h. Planet source. The planet source shown in Figure 49 will be used during spacecraft systems tests where the planet horizon scanner requires a target. These tests will be conducted in the celestial simulator building which contains two traveling cranes. The planet source will be mounted to one of the cranes which will provide means of moving it through various maneuvers to simulate flight conditions.

The source consists of a 16-inch diameter aluminum plate which is electrically heated over the back surface by means of a resistive coating. The front surface of the plate which is placed toward the scanner, is painted with a high emissivity paint to allow maximum radiation. Two annular masks are provided to reduce the effective angular diameter of the source from 4 to 1 degree depending on the particular test requirement. When used, the mask is mounted a short distance in front of the source and has a layer of insulation attached to its rear surface to prevent transmission of heat to the front surface where it would be reradiated toward the scanner.

The planet source will be capable of operation at 50 ± 25°C. Two source assemblies are being fabricated, one of which will be for laboratory bench testing of the planet scanner. During bench testing the temperature of the source will be controlled by a built-in miniature thermostat. A closed loop temperature control circuit is also being developed for use during system tests. It is expected that bench testing will begin approximately May 15, 1961.

i. Fine sun sensor. *Mariner* A utilizes a coarse–fine sun sensor mechanization. During initial sun acquisition the coarse mode, which has a 4π steradian field of view, is used. Disturbances to the accurately calibrated null due to sunlight reflected from many articulating devices necessitate switch out of the coarse sun sensor after initial sun acquisition. At this time the fine sun sensor, which has a narrow field of view, is switched on. Articulating members can easily be kept out of the small (14 degrees by 14 degrees) field; thus, the accurate null is undisturbed.

The *Mariner* fine sun sensor operates on the same shadow vane principle as the *Ranger* sun sensors and uses the same cadmium sulfide detectors manufactured by Clairex Corp. The circuit used is shown in Figure 50.

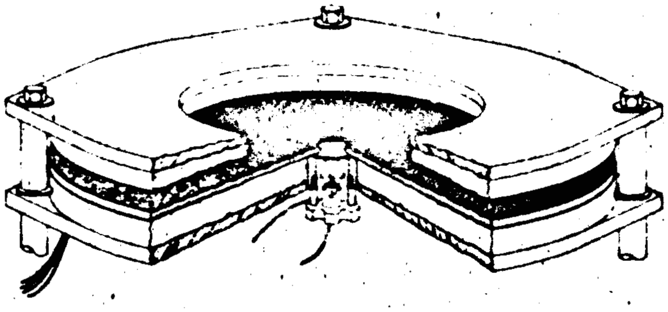

Figure 49. Planet source

which also includes the sun gate circuitry. The resistance of the detectors in each axis is closely approximated by Equation (1).

$$R_{1,2} = A\varepsilon^{\pm b\Delta\theta} \qquad (1)$$

where

R_1 and R_2 = resistance values of the detectors

$\Delta\theta$ = angular deviation, in degrees, of sensor from null

The voltage output expressed as a function of angle from null is:

$$E_o = \frac{2E\sinh(b\Delta\theta)}{2\cosh(b\Delta\theta) + \frac{A}{R_L}} \qquad (2)$$

where

R_L = load resistance ≃ 51000 ohms

A = individual detector resistance at null ≃ 6000 ohms

E = excitation voltage ≃ 16 volts

By differentiating Equation (2) an expression for the signal slope through null can be obtained:

$$\frac{\partial E_o}{\partial \Delta\theta} = \frac{2Eb\left(\frac{A\cosh b\Delta\theta}{R_L} + 2\right)}{\left(2\cosh b\Delta\theta + \frac{A}{R_L}\right)^2}$$

$$\left.\frac{\partial E_o}{\partial \Delta\theta}\right|_{\Delta\theta = 0} = \frac{2Eb}{\frac{A}{R_L} + 2} \qquad (3)$$

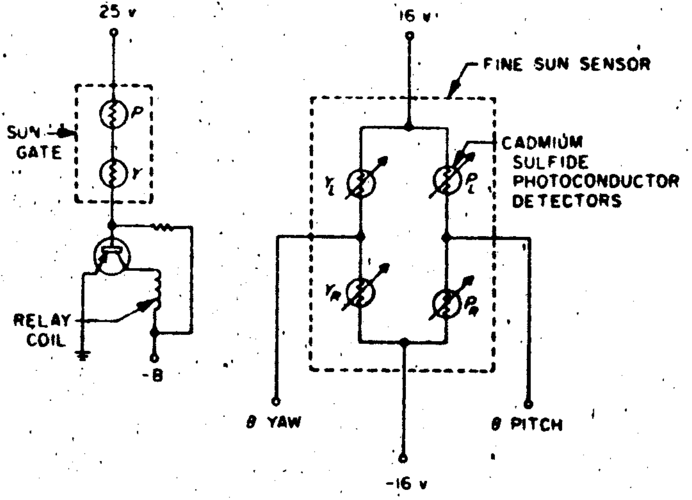

Figure 50. Sun gate circuitry

j. Sun sensor occulting array. The occulting array as shown in Figure 51 is designed to prevent scale factor changes caused by sun image growth as the spacecraft sun distance changes. The configuration used on the *Mariner* A sensor will eliminate gain change up to 1 milliradian displacement from null.

Figure 51 depicts a two-axis detector and occulting configuration; however, for simplicity, only a single axis employing Detectors X and Y will be considered in the following explanation. The sun image at earth distance is represented by the circle defined by r_1 and is 1 milliradian off-null. Under this condition Detector X generates the output signal which is proportional to the energized area, shown as Area A. If the sun image grows until its radius becomes r_2 an additional area (Area B) of detector X is energized. However, Area C which is equal to Area B energizes Detector Y. The outputs of Detectors X and Y are summed and, since they are of opposite polarity, Areas B and C cancel. This causes the effective error signal to be proportional to Area A as in the first case.

Null stability of this sun sensor is greatly enhanced by use of the occulting principle. For the 1-milliradian spillover example shown, a 50% reduction in gain of either detector will only cause a 0.03 milliradian null shift. With even larger gain reduction (approaching 100%) the null shift can never exceed the spillover, or, in this case, 1 milliradian.

k. Experimental model. An experimental model of the sun sensor has been fabricated. Typical output and cross-coupling characteristics are shown in Figure 52. The positive output of one axis (yaw) is shown for zero, 1 minute, and 2 minutes of pitch error. The output is low by approximately 30% because of the energy lost through the coelostat mirrors and earth's atmosphere. Figure 53 is the schematic diagram of the sun sensor.

l. Sun gate sensor. The *Mariner* sun gate sensor is provided to actuate attitude control and or search functions depending on whether the spacecraft roll axis is within 2.5 degrees of the sun line. It is a very simple

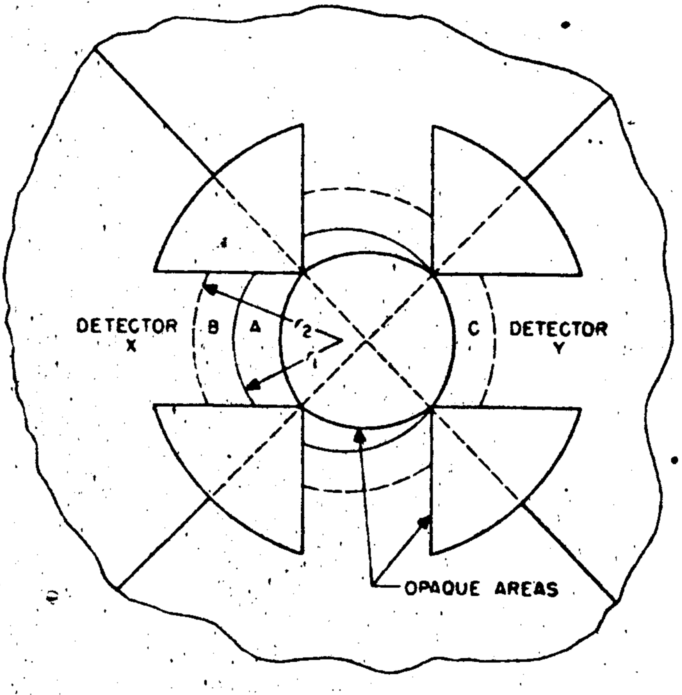

Figure 51. Two-axis detector

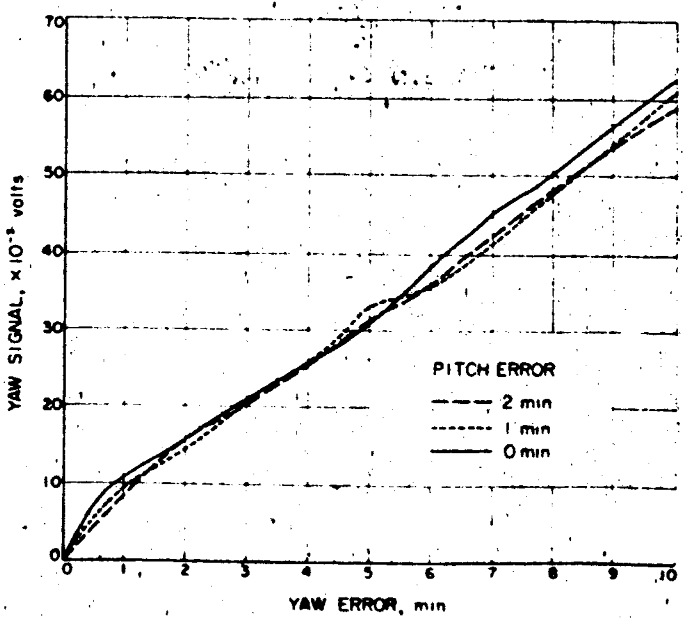

Figure 52. Sun sensor characteristics

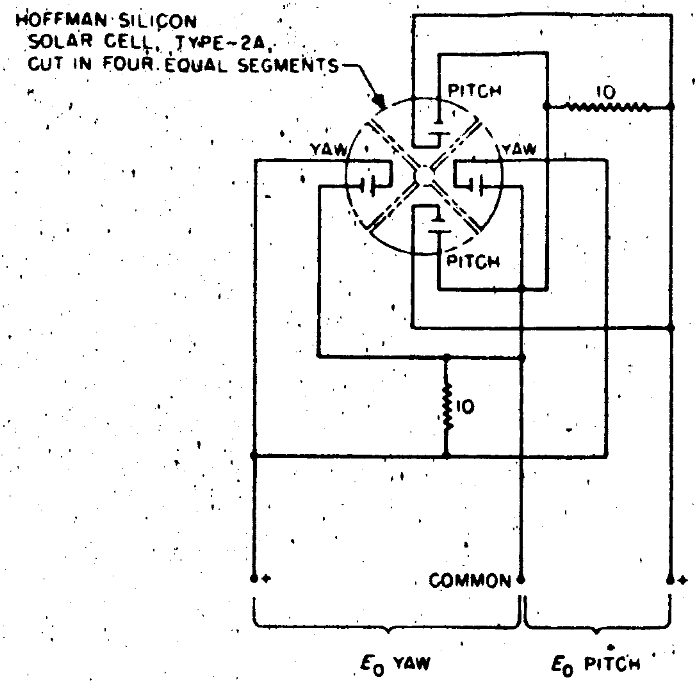
HOFFMAN SILICON SOLAR CELL, TYPE-2A, CUT IN FOUR EQUAL SEGMENTS
PITCH
10
YAW
YAW
PITCH
10
COMMON
+
+
E_0 YAW
E_0 PITCH

Figure 53. Sun sensor

device using a pair of small cadmium sulfide detectors. The first experimental plot of sun gate output is shown in Figure 54.

m. Long range earth sensor. The sensitivity of the *Mariner* A short range earth sensor limits its usefulness to distances below approximately 2 million miles. For ranges greater than this, the long range earth sensor is switched in. The development of the long range earth sensor (LRES) has been described in *SPS* 37-6 and -7. Many of the subsystem elements have been breadboarded but the prototype has not been completed. An error analysis based largely on estimates of subsystem performance is shown in Table 13 and a sketch of the assembled unit is shown in Figure 55.

n. Planet–moon simulator. The short and long range earth sensors are both devices that utilize the solar energy reflected from the earth. In addition, the sensors to be developed for star tracking and planet approach guidance may also use this portion of the electromagnetic spectrum. To simulate a planet or moon for the testing and evaluation of optical sensors, development has been initiated on an off-axis collimator. The simulator will provide a spectral distribution of the planet collimated energy over the range of 3500 to 8000 Angstroms such that the energy in any 1000 A band will not deviate by more than ±30% from the energy distribution of the sun outside of the earth's atmosphere.

Table 13. Long range earth sensor null offset analysis

Error source	Roll		Hinge	
	Random	Predictable	Random	Predictable
Moon position		1.03 mr at 10^8 miles		1.03 mr at 10^8 miles
Earth diameter		0.79 mr at 10^8 miles		0.79 mr at 10^8 miles
Phase shift in data processing	0.44 mr, 1σ	↑	0.44 mr, 1σ	↑
Calibration	1.0 mr, 1σ	These errors go to zero at Venus distance	1.0 mr, 1σ	These errors go to zero at Venus distance
Cross coupling	0.5 mr, 1σ		0.5 mr, 1σ	
Electronic drift	1.0 mr, 1σ		1.0 mr, 1σ	
Totals	1.56 mr, 1σ	1.82 mr (at 10^8 miles)	1.56 mr, 1σ	1.82 mr (at 10^8 miles)

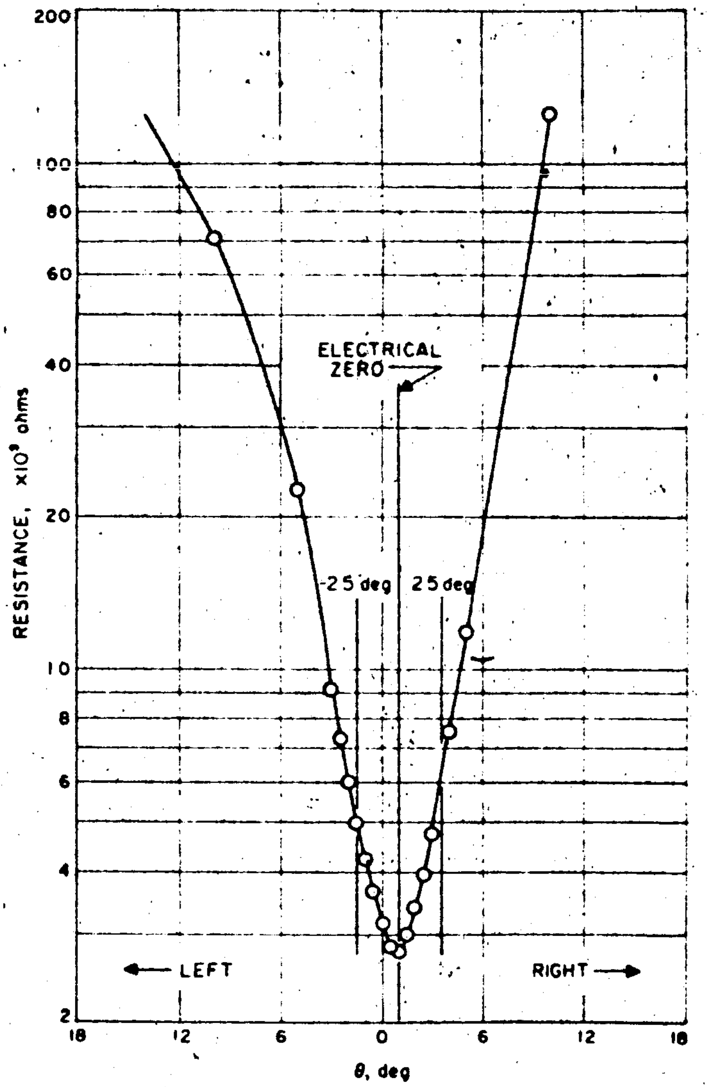

Figure 54. Sun gate output

Figure 56 shows the design configuration of the planet-moon simulator. By changing field stop discs, any size planet up to a maximum of 5.4 degrees can be simulated.

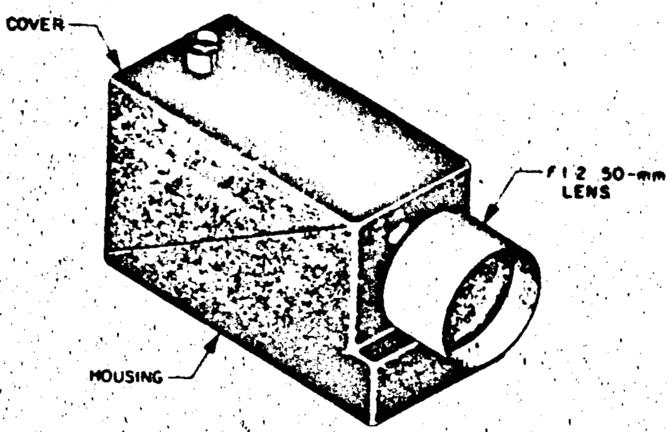
COVER
f/2 50-mm LENS
HOUSING

Figure 55. Long range earth sensor

In addition, with the smaller size planet simulations, a moon can be simultaneously simulated adjacent to the planet at reduced radiance consistent with its actual albedo. Use of a high pressure xenon arc source will allow the radiance level to be continuously variable over a wide range with negligible shift in the spectral distribution of the energy. The mosaic lens system will maintain uniform distribution of the radiance over the planet image, regardless of changes in arc size, as the total radiance level is changed.

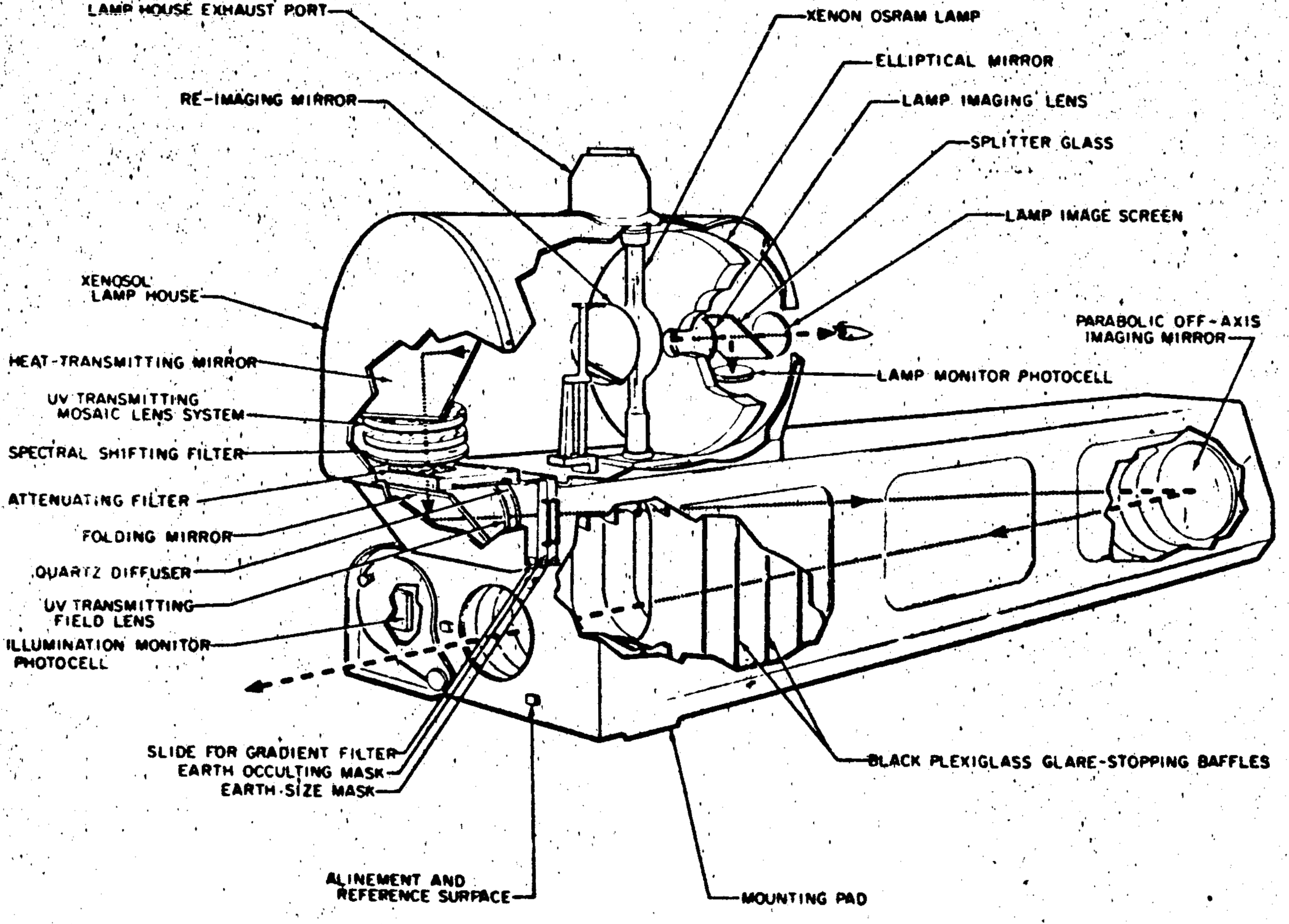
LAMP HOUSE EXHAUST PORT
RE-IMAGING MIRROR
XENON OSRAM LAMP
ELLIPTICAL MIRROR
LAMP IMAGING LENS
SPLITTER GLASS
LAMP IMAGE SCREEN
XENOSOL LAMP HOUSE
PARABOLIC OFF-AXIS IMAGING MIRROR
HEAT-TRANSMITTING MIRROR
LAMP MONITOR PHOTOCELL
UV TRANSMITTING MOSAIC LENS SYSTEM
SPECTRAL SHIFTING FILTER
ATTENUATING FILTER
FOLDING MIRROR
QUARTZ DIFFUSER
UV TRANSMITTING FIELD LENS
ILLUMINATION MONITOR PHOTOCELL
SLIDE FOR GRADIENT FILTER
EARTH OCCULTING MASK
EARTH SIZE MASK
BLACK PLEXIGLASS GLARE-STOPPING BAFFLES
ALINEMENT AND REFERENCE SURFACE
MOUNTING PAD

Figure 56. Planet—moon simulator

3. Sun Simulator

Progress has been made toward the design of a true Sun simulator adequate for the testing of accurate Sun sensors.

One difficult Sun simulation problem has been the change in brightness across the xenon arc lamp source. To reduce this differential, only the brightest portion of the arc adjacent to the cathode is utilized. Although the diameter of this spot is less than 1 mm, the brightness from the upper to the lower edge varies by a factor of two. If uncorrected this effect would create a simulated Sun of nonuniform brightness, which would introduce large pointing errors when Sun sensors (which seek the radiant center), were tested.

There are two apparent solutions to this problem. One is the utilization of a light pipe scrambler upstream from the aperture as shown in Figure 10.

The light pipe would consist of a cylindrical rod of quartz having flat polished ends. Radiation would exit from the rod end at the same cone angle that it entered, assuming no errors in the geometry of the rod. However, the internal reflections acting on a given ray will cause it to exit at a random circular angle dependent on the length and diameter of the rod. It is this characteristic that causes the scrambler to integrate the energy received and present a more uniform intensity at its output end.

The second solution to this problem involves the use of fiber optics. In this case the scrambler would consist of an incoherent fiber optics bundle. This scrambler would receive energy from a given point or fiber at one end, and transmit this energy to a random point at its output end. The effectiveness of this device would depend primarily upon the diameter of the fibers and how well they could be placed in random orientation at one end compared to the other.

A contract has been let for the design and fabrication of an optical system utilizing the light pipe scrambler first described. These optics will be used in conjunction with a 5000-w xenon arc lamp for the construction of the Mod. II Sun simulator.

As a backup design the fiber optics bundle is being considered, with the mechanical design and construction being done at JPL. The Mod I simulator using standard optical components and a 900-w xenon lamp is also being designed and constructed at JPL. This is a portable unit designed to energize Sun sensors while they are being environmentally tested as well as to test their output characteristics at ambient conditions.

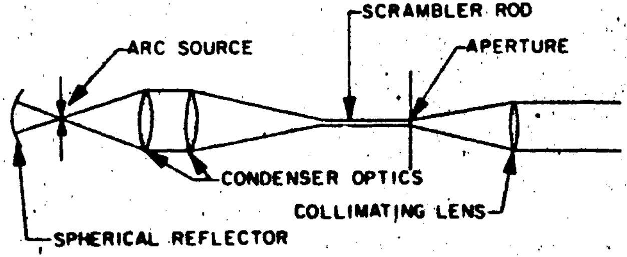

Figure 10. Sun simulator utilizing light-pipe scrambler

4. Long Range Earth Sensor

The long range Earth sensor (LRES) used on *Mariner* R uses a single photomultiplier tube together with a lens, a fixed aperture, and a modulating mask. The modulating mask is attached to a vibrating reed with a frequency of approximately 22 cps. The electronics associated with the reed (Fig 11) and the reed itself operate closed loop with a position pickoff device such that the reed oscillates at a constant amplitude. Frequency of oscillation is determined by the mechanical resonance of the reed only. Figure 12 shows the relative position of the optical elements. The knife edges on the modulating mask are in the focal plane of the optical system. The photomultiplier tube serves only as a light detector and has no position discrimination by itself.

The vibrating reed moves through a sufficient arc to completely uncover the fixed aperture at the extremes of motion. The output, therefore, is a series of pulses. A shift in the position of the Earth image in hinge causes a variation in the output pulse width. Similarly, a shift in roll causes a variation in the phase (or time) of the output relative to the reed motion. The electronics senses these properties in the pulse chain and at the output produces a dc voltage proportional to this error. Also present at the output are signals which indicate that an object is being tracked by the sensor and the amount of light being sensed.

The threshold of the unit is approximately 5×10^{-11} w/cm^2 (bolometric at a color temperature of 6000°K). The maximum intensity is a function of photomultiplier

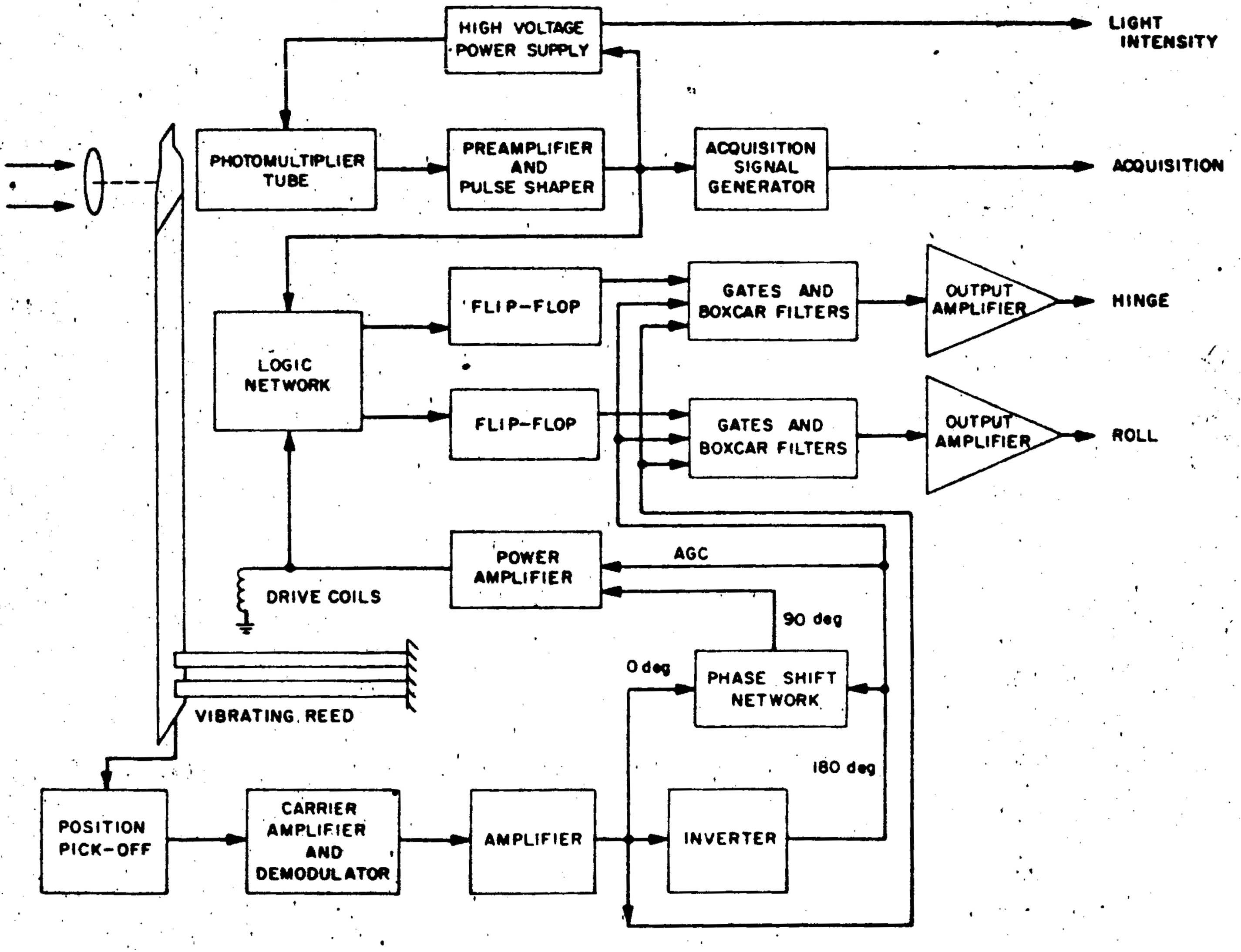
HIGH VOLTAGE POWER SUPPLY
LIGHT INTENSITY
PHOTOMULTIPLIER TUBE
PREAMPLIFIER AND PULSE SHAPER
ACQUISITION SIGNAL GENERATOR
ACQUISITION
FLIP-FLOP
GATES AND BOXCAR FILTERS
OUTPUT AMPLIFIER
HINGE
LOGIC NETWORK
FLIP-FLOP
GATES AND BOXCAR FILTERS
OUTPUT AMPLIFIER
ROLL
POWER AMPLIFIER
AGC
DRIVE COILS
90 deg
0 deg
PHASE SHIFT NETWORK
VIBRATING REED
180 deg
POSITION PICK-OFF
CARRIER AMPLIFIER AND DEMODULATOR
AMPLIFIER
INVERTER

Figure 11. LRES circuit

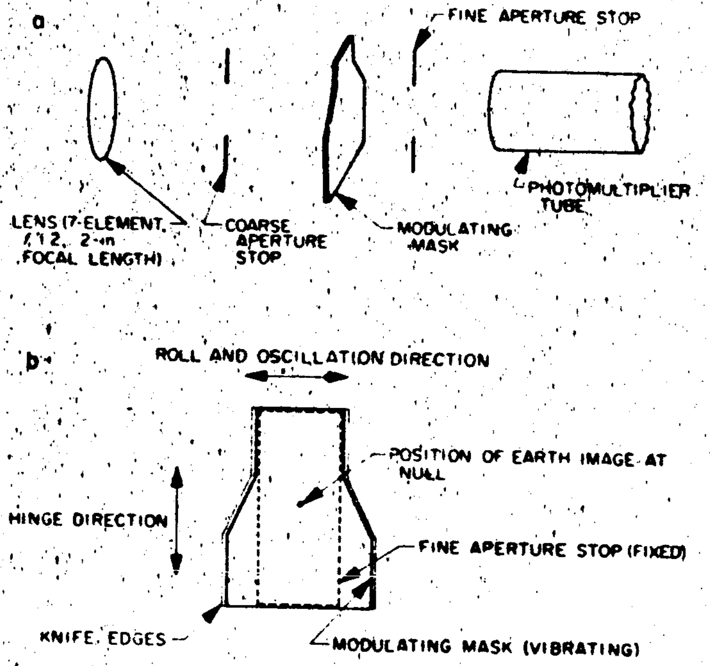
a
FINE APERTURE STOP
PHOTOMULTIPLIER TUBE
LENS (7-ELEMENT, f/1.2, 2-in FOCAL LENGTH)
COARSE APERTURE STOP
MODULATING MASK
b
ROLL AND OSCILLATION DIRECTION
POSITION OF EARTH IMAGE AT NULL
HINGE DIRECTION
FINE APERTURE STOP (FIXED)
KNIFE EDGES
MODULATING MASK (VIBRATING)

Figure 12. Relative position of LRES optical elements

tube life and has been defined as 5×10^{-7} w/cm^2. Intensities much higher than this will not affect the tube for short periods of time. With power off, the sensor may be pointed directly at the Sun for extended periods.

The accuracy of the LRES is ±0.1 deg in roll and ±0.25 deg in hinge over the range of 0 to +100°F. Expected inflight stability is approximately ±0.02 deg in roll and ±0.05 deg in hinge. Power dissipation is approximately 6.5 w and total assembled weight is 6.2 lb.

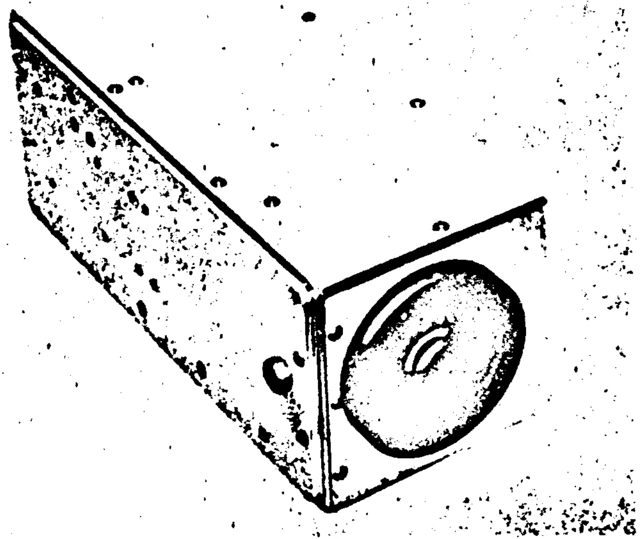

Fig. 12. Long-range Earth sensor

Function	Property
Null drift (expected in flight)	±0.02-deg roll ±0.05-deg hinge
Roll scale factor	4 v/deg ±10%
Hinge scale factor	2 v/deg ±10%
Roll saturation	4 v ±10%
Hinge saturation	4 v ±10%
Acquisition signal	7 ±1 v dc
Light intensity readout	0 to −3 v dc
Collecting optics	7 element *f*/1.2 2-in. focal length

3. Long-Range Earth Sensor

The long-range Earth sensor (LRES), previously described in *SPS 37-14*, is now qualified and ready for flight (Fig. 12). A functional block diagram is shown in Fig. 13. Functional properties of the LRES are as follows:

Function	Property
Field of view	±2-deg roll and ±5-deg hinge
Radiant input range (bolometric at 6000°K)	5×10^{-11} w/cm^2 to approximately 5×10^{-7} w/cm^2
Power dissipation	6.5 w
Weight	6.2 lb
Null stability (absolute, with reference to external mounting pads)	0.1-deg 3 σ roll 0.25-deg 3 σ hinge

The LRES is affected by off-axis disturbances to some degree. Extensive testing was performed to estimate and correct this defect. Results of the testing are shown in Figs. 14, 15, 16, 17, 18 and 19. During these tests, additional problems associated with properly simulating the space environment arose. Extraneous light was also reflected from test equipment, dark room walls, and operating personnel so that the results as shown should tend to be on the pessimistic side.

Testing of the LRES is done with an Earth–Moon simulator and a Griswold optical dividing head. The test setup and rack are shown in Fig. 20. During initial testing a problem arose due to the front surface of the vibrating reed being highly reflective. Light was reflected from

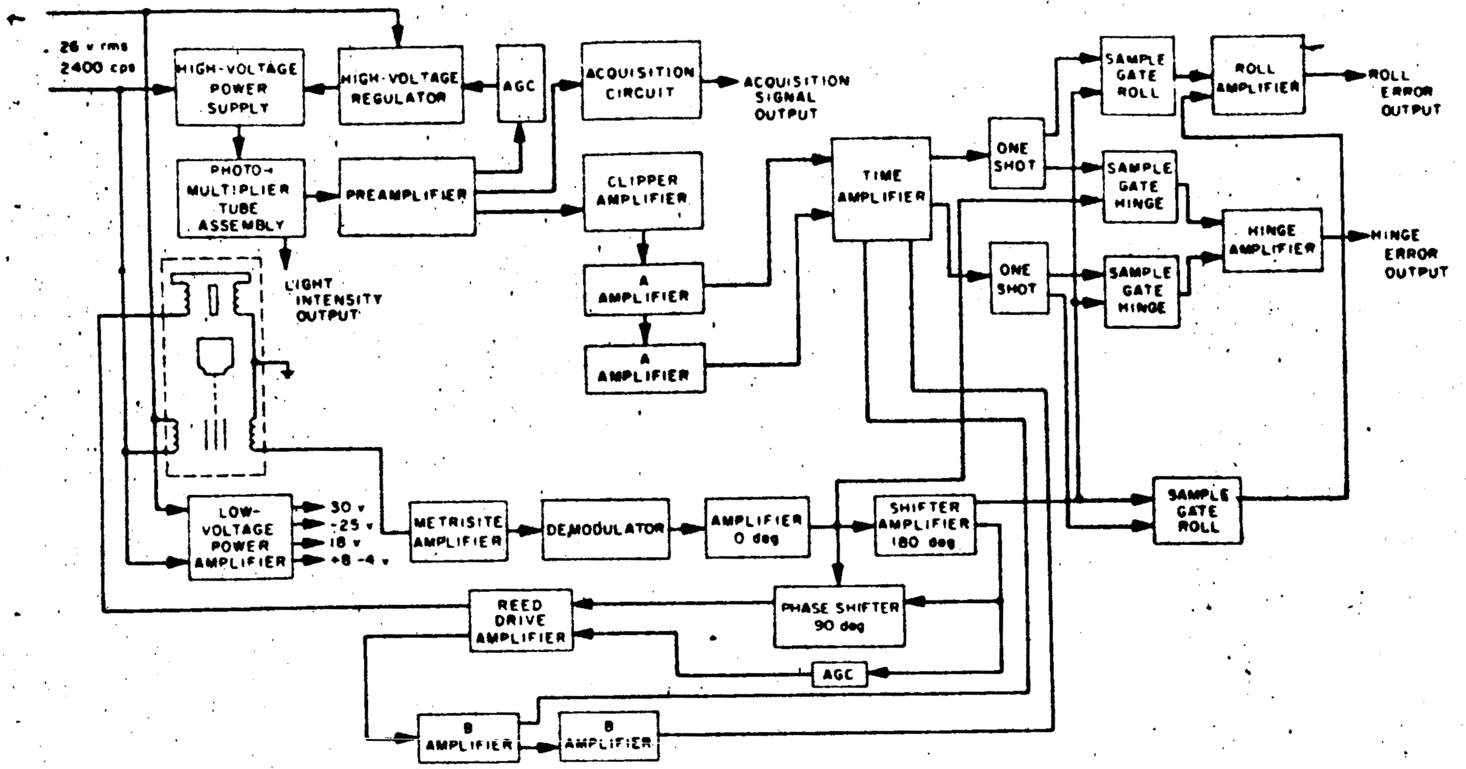
26 v rms
2400 cps
HIGH-VOLTAGE POWER SUPPLY
HIGH-VOLTAGE REGULATOR
AGC
ACQUISITION CIRCUIT
ACQUISITION SIGNAL OUTPUT
PHOTO-MULTIPLIER TUBE ASSEMBLY
PREAMPLIFIER
CLIPPER AMPLIFIER
A AMPLIFIER
A AMPLIFIER
LIGHT INTENSITY OUTPUT
TIME AMPLIFIER
ONE SHOT
ONE SHOT
SAMPLE GATE ROLL
SAMPLE GATE HINGE
SAMPLE GATE HINGE
ROLL AMPLIFIER
ROLL ERROR OUTPUT
HINGE AMPLIFIER
HINGE ERROR OUTPUT
LOW-VOLTAGE POWER AMPLIFIER
30 v
-25 v
18 v
+8 -4 v
METRISITE AMPLIFIER
DEMODULATOR
AMPLIFIER 0 deg
SHIFTER AMPLIFIER 180 deg
SAMPLE GATE ROLL
REED DRIVE AMPLIFIER
PHASE SHIFTER 90 deg
AGC
B AMPLIFIER
B AMPLIFIER

Fig. 13. Long-range Earth sensor functional block diagram

ROLL ANGLE, deg	LOSS OF ACQUISITION, w/cm²	REGAINED ACQUISITION, w/cm²
90	3.08×10^{-2}	2.52×10^{-2}
85	2.94×10^{-2}	2.38×10^{-2}
80	2.78×10^{-2}	2.09×10^{-2}
75	2.52×10^{-2}	1.82×10^{-2}
70	2.09×10^{-2}	1.40×10^{-2}
65	1.68×10^{-2}	1.12×10^{-2}
60	1.26×10^{-2}	9.60×10^{-3}
55	1.07×10^{-2}	7.00×10^{-3}
50	7.00×10^{-3}	4.49×10^{-3}
45	4.22×10^{-3}	1.82×10^{-3}
40	2.52×10^{-3}	1.68×10^{-3}

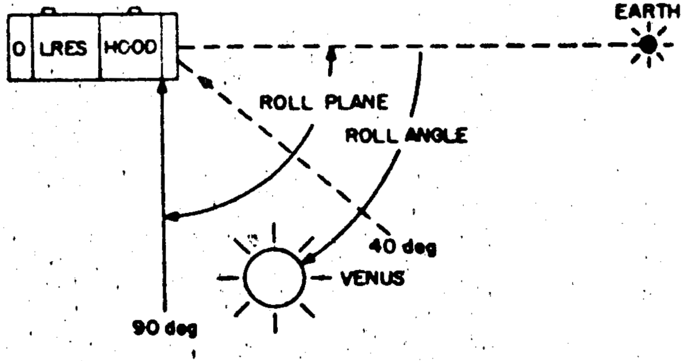
O
LRES
HCOD
EARTH
ROLL PLANE
ROLL ANGLE
40 deg
VENUS
90 deg

Fig. 14. Roll plane test

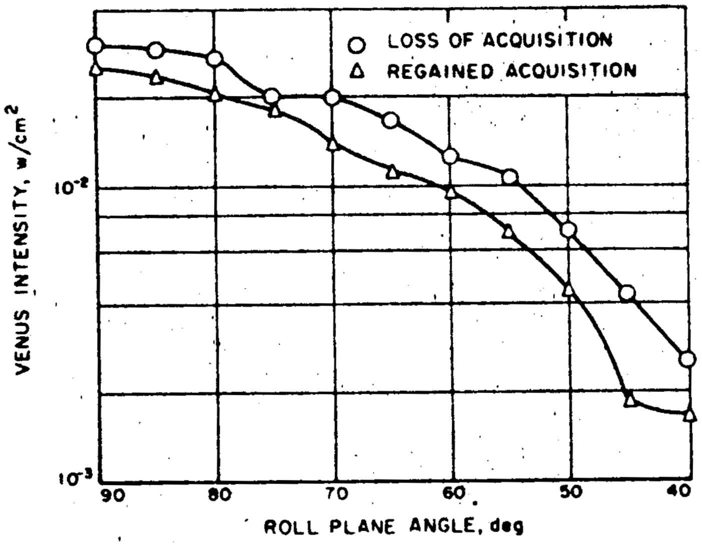

Fig. 15. Roll plane test, Part II

the reed 45-deg bevel to the black phototube housing and from there diffusely reflected to the photomultiplier. In simulated acquisition tests the Earth sensor would deliver an "acquisition" signal even though the Earth was as much as 20 deg out of the geometric field of view. The phase of the error signal at this time was also inverted so that Earth lock would have been prevented. This prob-

HINGE ANGLE, deg	LOSS OF ACQUISITION, w/cm^2	REGAINED ACQUISITION, w/cm^2
90	7.85×10^{-3}	6.25×10^{-3}
85	7.85×10^{-3}	6.25×10^{-3}
80	7.00×10^{-3}	5.05×10^{-3}
75	4.50×10^{-3}	3.36×10^{-3}
70	3.93×10^{-3}	3.22×10^{-3}
65	3.65×10^{-3}	2.52×10^{-3}
60	2.80×10^{-3}	1.68×10^{-3}

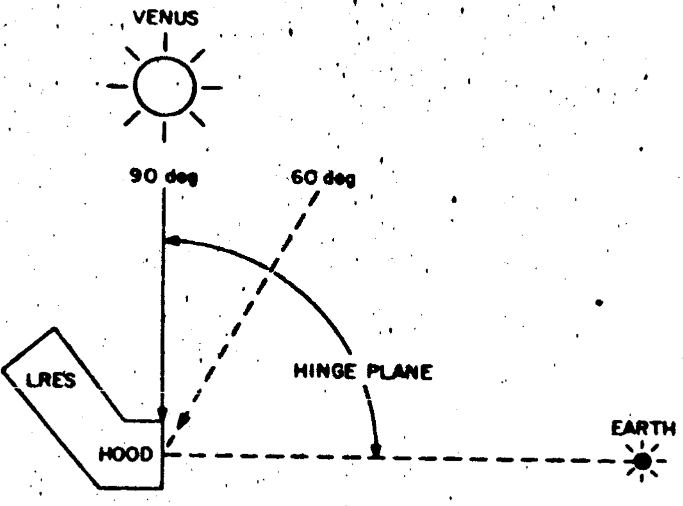
VENUS
90 deg
60 deg
LRES
HOOD
HINGE PLANE
EARTH

Fig. 16. Hinge plane test

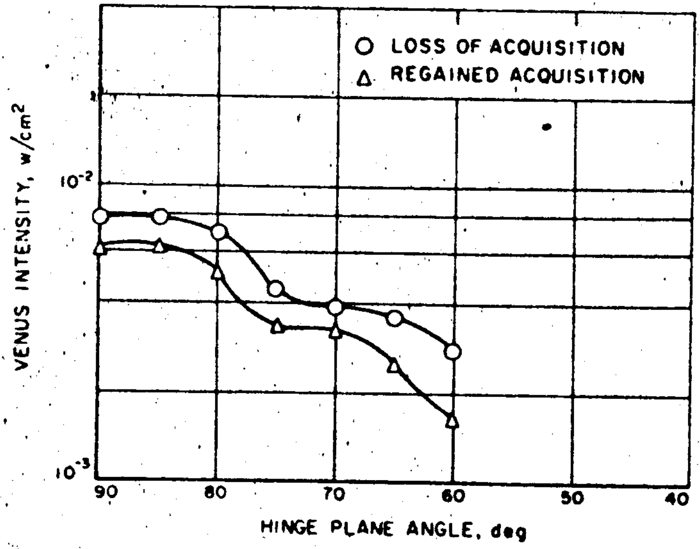

Fig. 17. Hinge plane test, Part II

lem was associated only with the high-intensity Earth. Solution was twofold:

(1) Blacken the reed, especially the 45-deg bevel.

45-deg PLANE DEVIATION, deg	LOSS OF ACQUISITION, w/cm^2	REGAINED ACQUISITION, w/cm^2
90	2.80×10^{-2}	2.11×10^{-2}
85	2.52×10^{-2}	1.54×10^{-2}
80	2.24×10^{-2}	1.40×10^{-2}
75	1.96×10^{-2}	1.40×10^{-2}
70	1.68×10^{-2}	1.08×10^{-2}
65	1.40×10^{-2}	1.08×10^{-2}
60	1.26×10^{-2}	9.62×10^{-3}
55	1.12×10^{-2}	7.53×10^{-3}
50	7.55×10^{-3}	6.18×10^{-3}
45	3.93×10^{-3}	3.08×10^{-3}
40	3.08×10^{-3}	2.52×10^{-3}

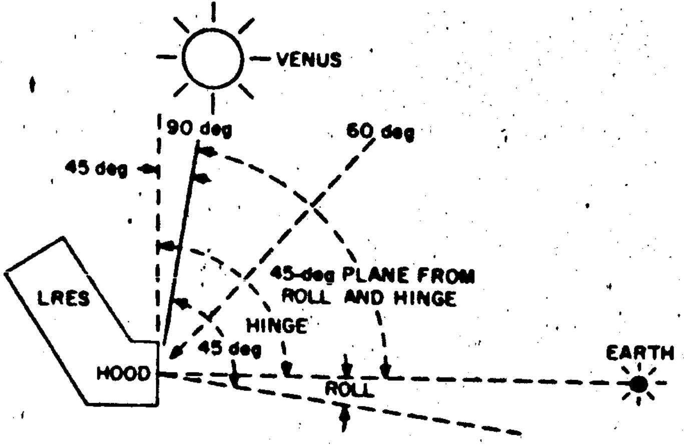
VENUS
90 deg
60 deg
45 deg
LRES
HOOD
45-deg PLANE FROM ROLL AND HINGE
HINGE
45 deg
ROLL
EARTH

Fig. 18. 45 deg from both hinge and roll plane test

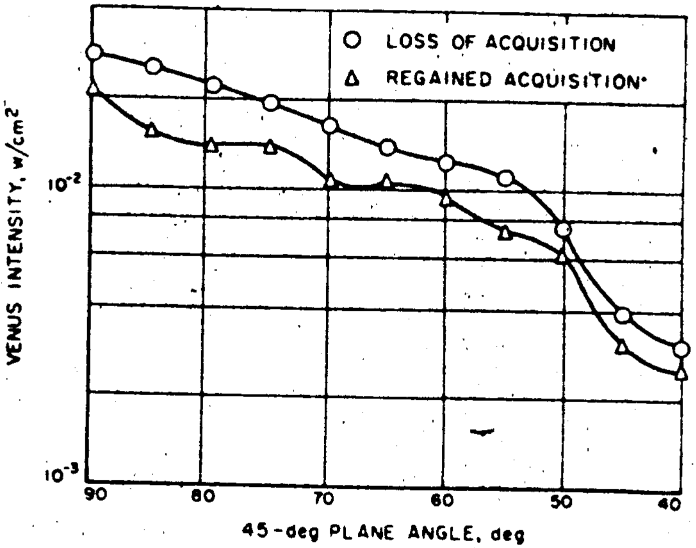

Fig. 19. 45 deg from both hinge and roll plane test, Part II

(2) Introduce wave-shape discrimination into the acquisition channel.

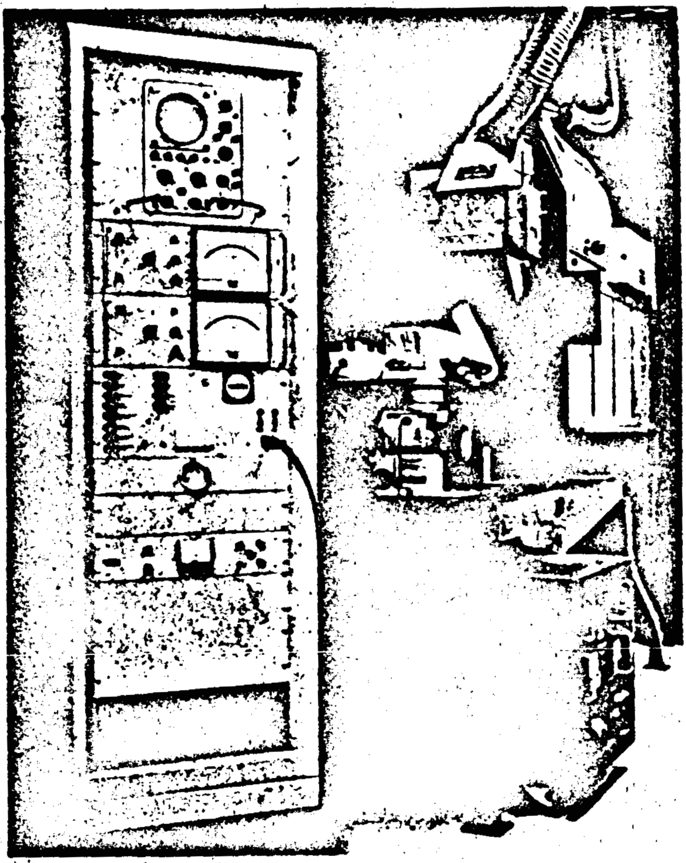

Fig. 20. LRES test equipment

An additional electronic problem was discovered. Electric motors operating in the vicinity of the Earth sensor caused erratic performance. This difficulty was traced to three fast-switching diodes in the reed drive loop. The three fast diodes (FD100) were changed to general purpose (IN457) to solve the difficulty.

4. Earth–Moon Simulator

The Earth–Moon simulator (Figs. 21, 22) is a device designed and fabricated by Nortronics to present a simulation of the Earth, Moon and Earth, or a star. The simulator provides the means with which to determine accuracy of alignment and flux level response. Continuous variable levels of irradiance are available for discrete distances from the Earth. There are provided five different Earth-phase positions for the larger size diameter Earth. The simulator provides a 5-in. diameter collimated light which is good to 5-sec-of-arc accuracy with reference to the point source. The integrated intensity of the flux density in the beam (per cm^2) from the simulator does not vary more than 5% over the center 3-in. diameter of the beam and not more than 10% over the entire 5-in. diameter. Earth diameters from 5.411 to 0.000452 deg can be simulated (in discrete steps). Color temperature between 0.35 and 0.8 μ approximates a 5200°K black body. Variations in flux are possible over a range of 159.7×10^{-6} w/cm^2 to 1.12×10^{-12} w/cm^2. The angular position of the Earth's geometric center is within 1 min of arc normal to the simulator external alignment surface. The outer edge of the simulated Earth is circular within 0.1% of the angular diameter plus 5 sec of arc.

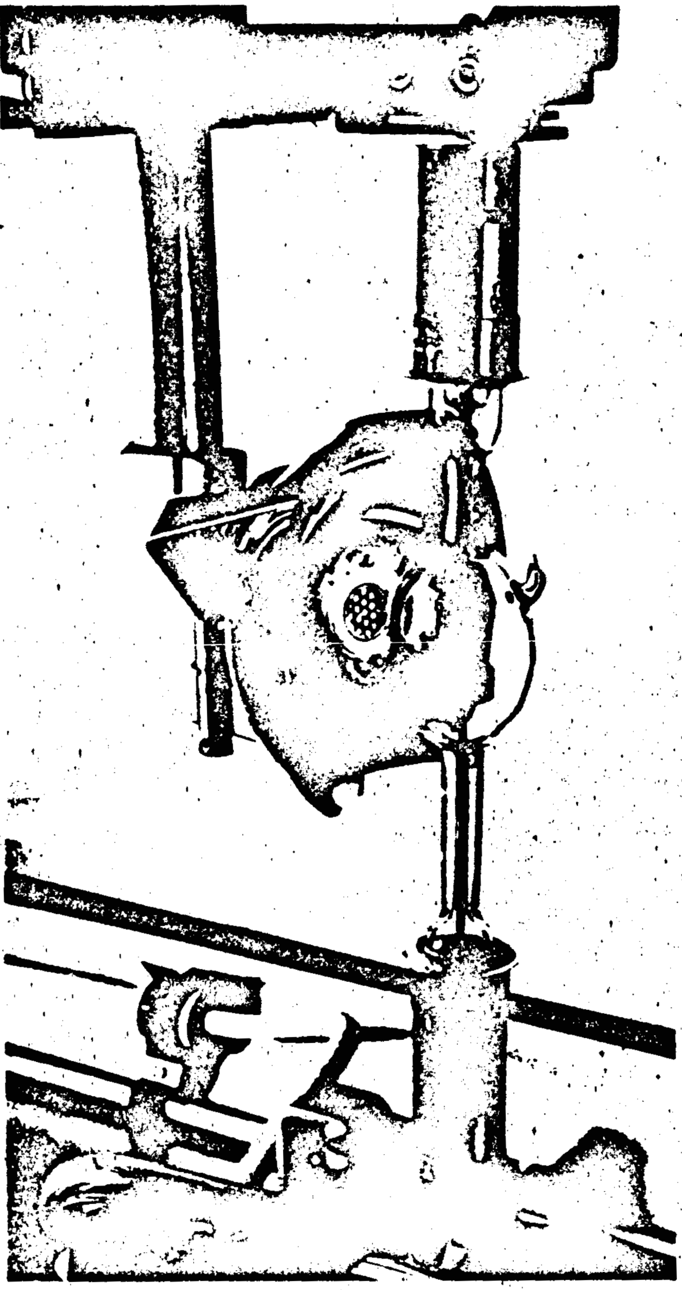

Fig. 21. Earth–Moon simulator light source and reflector

The light source is an Osram, 900-w xenon lamp, as shown in Fig. 21, with the parabola reflector mounted directly behind it. The light is projected through several lenses and reflected by three mirrors before it comes out of the simulator in the desired image. The intensity is varied with neutral density filters inserted in the upper sliding frame as shown in Fig. 22. Also in the same figure, the lower sliding frame is used to hold the different aperture plates which simulate the different sizes and configurations of the Earth and Moon. Swung out of the way from the front opening is a cover with a photocell mounted on it to measure the flux density which is present. The photocell is connected to the microammeter on the side of the simulator case and the reading is converted into flux density. The Earth–Moon simulator can also be made to simulate stars, such as Canopus, with some minor modifications.

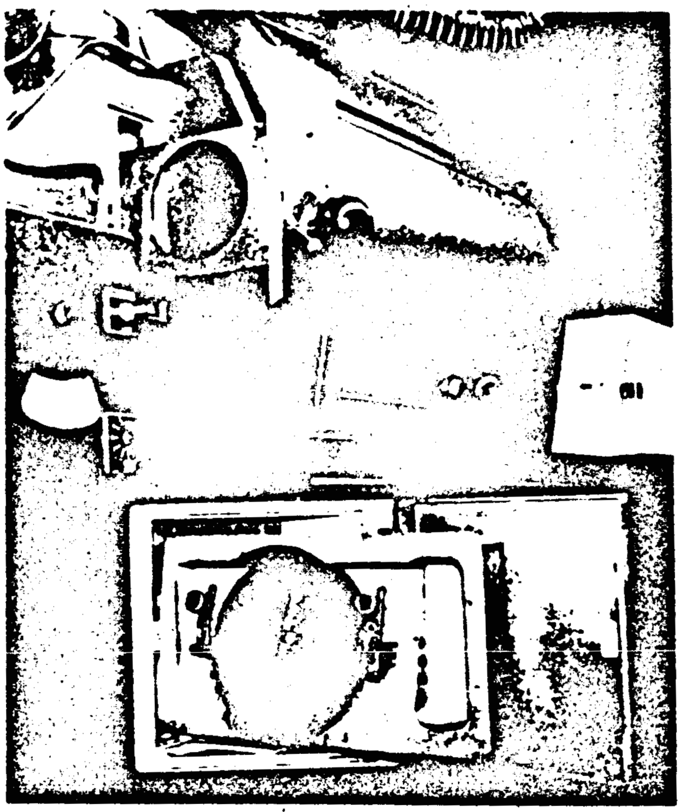

Fig. 22. Earth–Moon simulator

3. Integrated Guidance Package Design

a. Configuration. Design aims included:

(1) All guidance sensors should be in one package that can be aligned and tested independent of the spacecraft.

(2) The package should go into the spacecraft in the same location for all *Mariner* B missions.

(3) Modification to sensors in the package to accommodate mission geometry changes should not involve gross mechanical redesign or cabling changes.

Fields of view of the three guidance sensors are responsible for the general configuration of the package and the location of the package on the spacecraft. The Sun sensors must look through the solar panel and the Canopus tracker must be far from the plane of the solar panel, so that solar panel tips are out of its field of view. The solar panels force the package to be long. Venus-type one cone angles are less than 90 deg, so the guidance planet tracker must look through the solar panel and be located close to it. Even though Mars cone angles are nominally 150 deg, the Guidance Planet Tracker (GPT) can still be located near the solar panel. It must be, because its large size would cause mechanical interference with the folded solar panels if it were located any appreciable distance above the fixed solar panel. Nominal Mars clock angles of 90 deg require the package to be located on the minus *X* side of the spacecraft.

The GPT as presently envisioned has a 4-deg field of view which is gimbaled by means of two single-axis mirrors so that its dynamic range is a 20-deg included angle cone. To accommodate the widely varying nominal planet directions associated with *Mariner* B missions, a mounting flange will be used to support the GPT. This flange will be tailored to suit the mission.

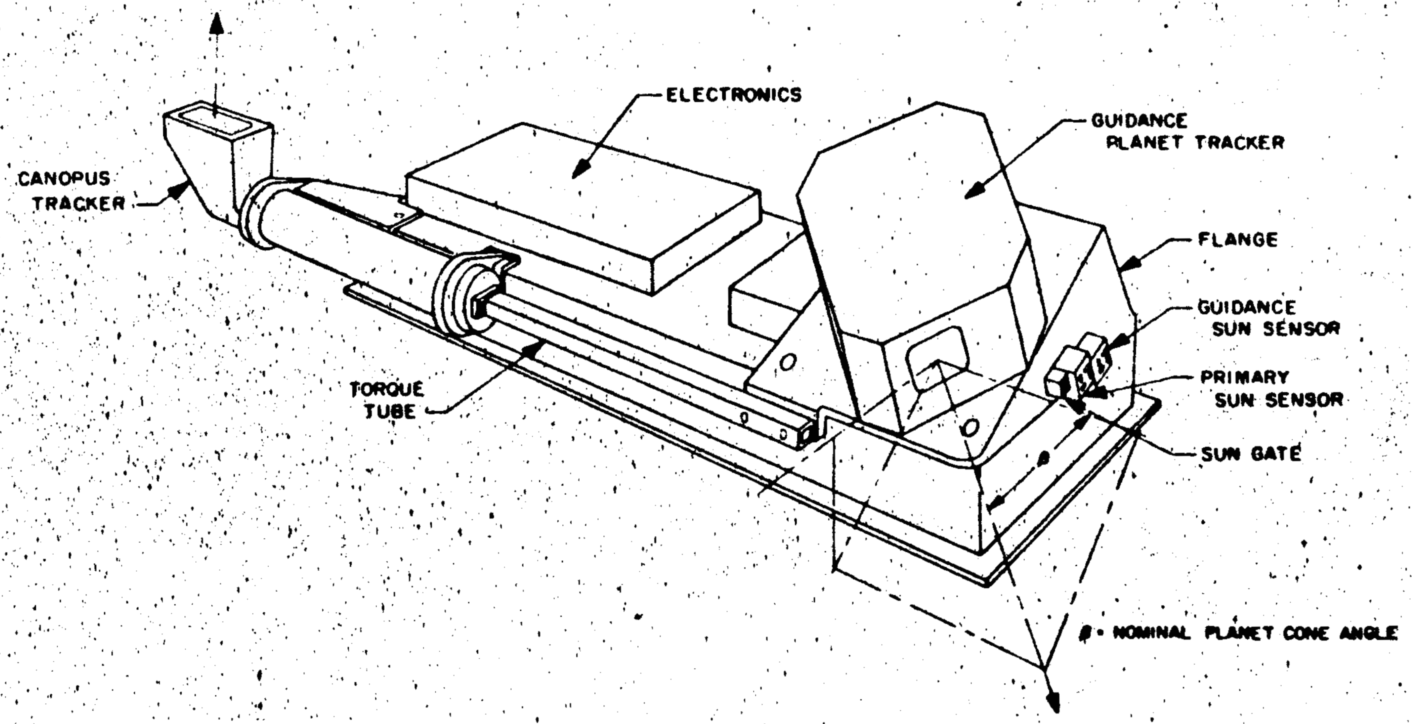

Fig. 31. Integrated guidance package

There are 2 deg of freedom needed for mounting the GPT in an arbitrary position. Cone-and-clock-angle degrees of freedom turn out to be quite convenient. The clock-angle degree of freedom is set by the flange and the cone angle is set by the rotation of the GPT on the flange face. By using this scheme the flange is simplified and one axis of the mirror gimbaling deflects the field of view along a meridian of spacecraft-centered cone-clock angle coordinates. The only compromise involved is a constraint on the mechanical configuration of the GPT: the window must be on a face which is perpendicular to the mounting surface. This constraint does not appear to be a great disadvantage. Using part of this flange for the Sun sensor mounting surface has the advantage of minimizing the number of machining tolerances between the Sun direction and the GPT.

Figure 31 shows the general configuration of the guidance package.

Relative alignment between optical sensors is most critical during the approach-guidance phase of the mission. Although an error analysis has not been completed, it is felt that relative measurement, better than 1 min of arc, will be required. During approach-guidance measurements, the zero-roll direction defined by Canopus tracker and the roll axis defined by the guidance Sun sensor must be held quite closely. This means structural bending between the GPT and Sun sensors must be minimized, and torsional warping between the GPT and the Canopus tracker must be minimized. Bending is of secondary importance in the alinement between the GPT and the Canopus tracker. The bending component in the Sun–probe–Canopus plane has no effect and the component out of this plane causes only small errors in the roll attitude. This error is approximated by the following equation:

$$a = A(\sin b_{\max} - \sin b_{\min})$$

where

a = error in roll

A = angular misalignment of Canopus tracker optical axis with Sun sensor

b = Canopus cone angle

The range of the Canopus cone angle during approach guidance is roughly 2 deg. Therefore, $a = 0.035\ A$. Roughly ¼ deg absolute accuracy is needed between Sun direction and the Canopus tracker optical axis.

Bending misalignments can be caused in several ways:

(1) Thermal gradients (static and dynamic).

(2) Creep.

(3) Residual stresses established on assembly.

(4) Change in gravitational environment between time of assembly and zero-g flight.

(5) Machining tolerances.

Torsional misalignments are caused basically in three ways:

(1) Torsion loading.

(2) Differential bending.

(3) Machining tolerances.

Both bending and torsional misalignments can be minimized by keeping the package compact. Unfortunately, this is impossible, due to field-of-view constraints. However, it is fortunate that the GPT and Sun sensors are close together, since their alignment is critical in bending. To maintain the torsional alignment between the Canopus tracker and the GPT, the Canopus tracker is supported in bearings (minimizing torsional loading) and is coupled to the GPT through a single torque tube (eliminating the possibility of differential bending). The torque tube may in fact be supported in bearings at points along its length, since bending does not effect the torsional alignment of the ends. The ¼-deg absolute alignment required between the Canopus-tracker optical axis and the Sun direction must be adjusted at the time of assembly. It is reasonable to assume that thermal warping will not be serious enough to destroy this alignment.

4. Field of View Calculations

The field of view of optical sensors is determined by means of shadowgraphs. Generation of the shadowgraph has been simplified by setting up a 1620 Fortran program. Calculation of the cone and clock angles of spacecraft solar panels, science experiments, etc., as viewed from the *Mariner* B Canopus tracker is illustrated by the shadowgraph (Fig. 32). A roll-attitude degree of freedom is required by *Mariner* B, so it is convenient to make the zero-cone axis parallel to the spacecraft roll axis (roll of spacecraft then does not affect the shadowgraph outline). Canopus tracker field is shown for a roll attitude of 114 deg. Figure 32 shows that roll attitudes may be chosen between 6 and 114 deg or between 143 and 170 deg. Between 114 and 143 deg the ion chamber interferes with tracker cone of sensitivity.

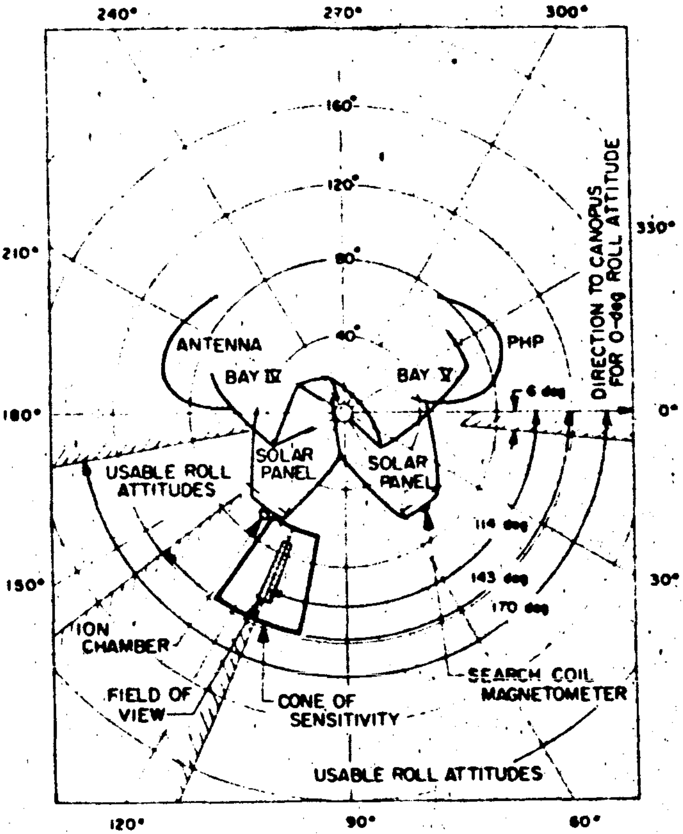

Fig. 32. Shadowgraph of *Mariner* B from the Canopus tracker

5. Sun Simulators and Sensors

a. Sun simulators. The design of the Mod I simulator as described in *SPS 37-14* has been completed. The optical system, which is comprised of standard optical components, has been set up on an optical bench. Preliminary tests indicate that the collimation accuracy is well within the design goal of ±15 sec of arc. The support structure, which has retractable casters for portability, has been fabricated. This structure supports a standard lathe bed, which in turn supports the rest of the simulator. It is estimated that all other parts necessary to assemble the simulator will be available by June 20, 1962.

The contract for the design and fabrication of the optical system for the Mod II simulator has been completed. Tests show that the collimation accuracy of this optical system also is well within the design goal of ±15 sec of arc. The over-all design of the simulator is 90% complete. All drawings should be released by June 30.

Fabrication of the lathe bed support assembly has been completed. The electronic equipment to operate the 5000-w xenon lamp has been procured.

It is expected that all parts will be fabricated by July 30, allowing the assembly of the unit to proceed.

b. Sun gate. The Sun gate used on *Mariner* B is of the same design used on *Mariner* R (Fig. 33). Its output signal is used to terminate the acquisition mode whenever the spacecraft roll axis is within 2.5 deg of the Sun line. The excitation voltage to the secondary Sun sensors is removed upon acquisition. This eliminates any secondary sensor outputs which would degrade the accuracy of the primary Sun sensors since both outputs are connected to a common point.

c. Primary Sun sensor. The primary Sun sensor operates on the same principle as do the *Ranger* Sun sensors. The major difference is that the four cadmium-sulfide detectors are located in one assembly rather than at four different points on the spacecraft. This is made possible by a reduction in the field of view which prevents obstructions caused by adjacent spacecraft components. As shown in Fig. 33, a single-aperture plate provides a shadow bar for each detector. The aperture is designed to give the sensor a 44-deg total angle field of view about both the pitch and yaw axes (44 deg in pitch and 28 deg in yaw for the pitch axis and 44 deg in yaw and 28 deg in pitch for the yaw axis).

d. 4π steradian Sun sensor. The 4π steradian Sun sensor is required for *Mariner* B to give a readout of the attitude of the spacecraft relative to the Sun. The sensor has a 4π steradian field of view which allows a readout signal to be generated regardless of the position of the spacecraft.

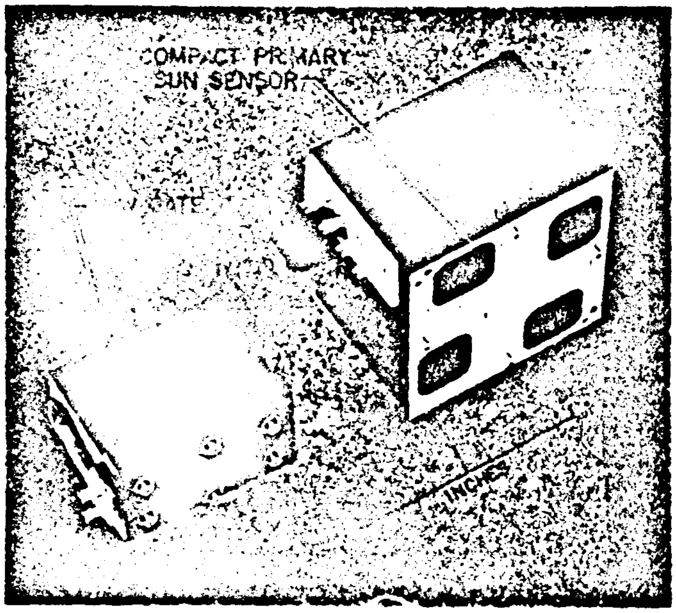

Fig. 33. *Mariner* B Sun gate

The principle of this sensor can best be understood by visualizing it as a cube having a silicon solar cell on each surface. Cells on opposing surfaces are connected to a load resistor so that the signal voltage across the resistor is plus when one cell is illuminated and minus if the opposite cell is illuminated. The system then provides three separate outputs which will be telemetered from the spacecraft. If the faces of the cube are alined perpendicular to the spacecraft axes, then the three outputs would be V_{pitch}, V_{yaw} and V_{roll}. The formulas for the angles between the Sun line and spacecraft axes (assuming a Lambert detector response) then become

$$\theta_{pitch} = \tan^{-1}\frac{Vz}{Vy}$$

$$\theta_{roll} = \tan^{-1}\frac{Vy}{Vx}$$

$$\theta_{yaw} = \tan^{-1}\frac{Vx}{Vz}$$

These calculations will be done by a ground-based computer. The actual computations will be more complex since the cell faces of the sensor will not be perpendicular to the yaw and pitch axes of the spacecraft, and the cells are not Lambert in their response.

The 2π steradian field of view required by each of the six elements of the 4π-steradian Sun sensor can only be met by placing the elements on the extremities of the spacecraft. Even then, objects in the local area of the elements may remain in the field of view. On the *Mariner* B spacecraft, science experiments on the solar panel tips make it impossible to locate three mutually perpendicular pairs of cells on the structure of the spacecraft.

To solve this problem, each element is split in two, and back-to-back mirrors are erected perpendicular to the plane of the cells (Figs. 34, 35, 36). The two mirror-cell units are now separated so that the troublesome object is occulted to the two cells by the mirrors, as shown in Fig. 35. The output currents of the two cells are summed and the sum is treated the same as the output from a simple cell. The current lost because cell No. 2 is partly or completely shaded is made up for by the increase in intensity on cell No. 1 caused by the mirror. Design requirements are:

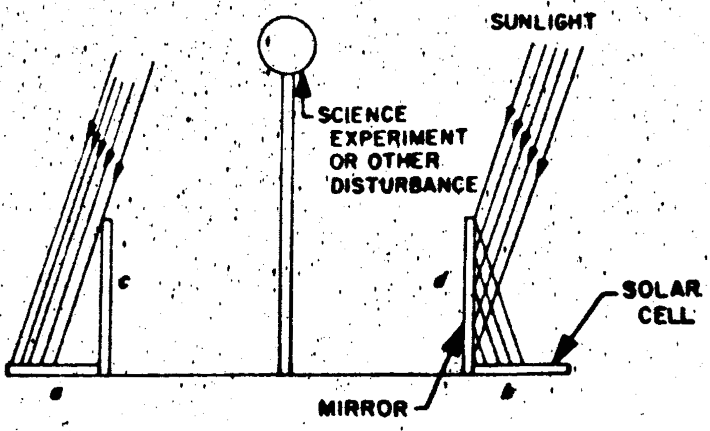

Fig. 34. 4π steradian Sun-sensor occulting method

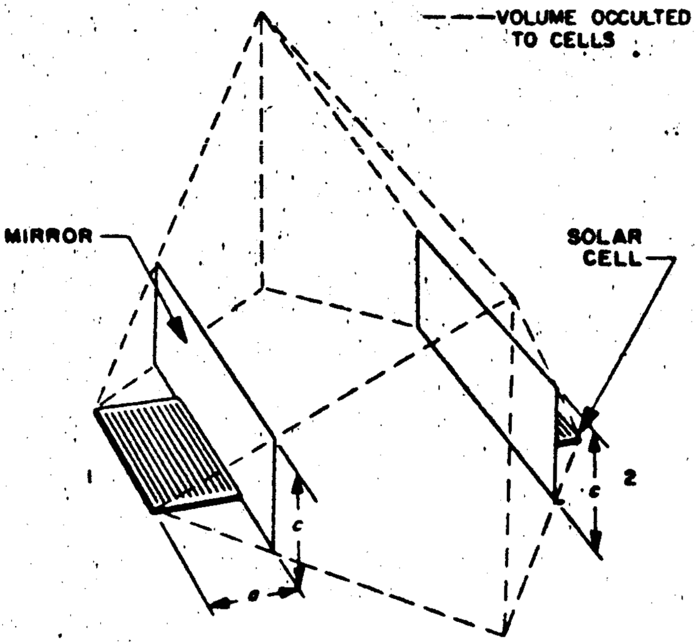

Fig. 35. 4π steradian Sun sensor experiment occultation

(1) The shape of mirrors and cells must be identical.

(2) The cells must be perpendicular to the mirror.

(3) The mirrors must be parallel.

(4) Nothing may be in the 2π steradian field of view of either cell except its associated mirror.

(5) Cell current must be a linear function of intensity.

Errors can be expected from several geometric sources:

(1) Error is contributed the system by nonperpendicularity of the elements faces (Fig. 36): maximum system error = *e*.

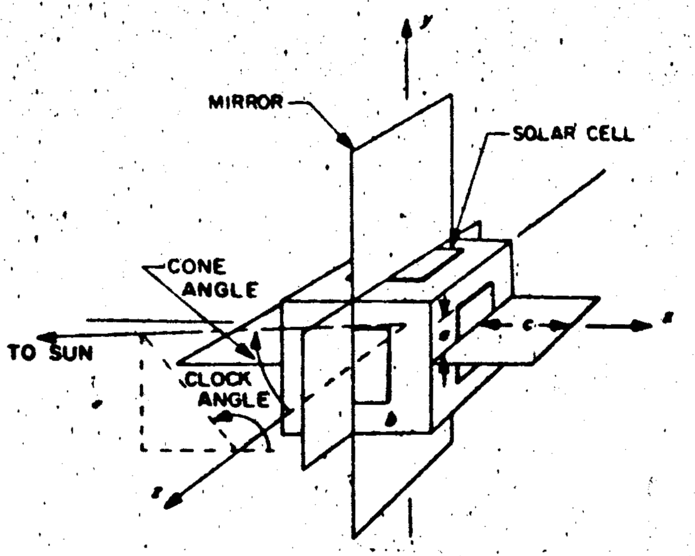

Fig. 36. 4π steradian Sun sensor, showing coordinates

(2) Misalignment of half an element: maximum system error = ¼ *e*.

(3) The lack of a mirror (with 100% reflectance) will introduce a certain amount of error to the system. However, by making the mirrors large compared to the size of the cells, large areas of the celestial sphere will be free from error caused by reflectance since the reflectance cancels out the system equations. Shown in Fig. 37 is a polar projection of the areas for which the error cancels for the geometrical configuration shown in Fig. 38 (errors cancel in dark regions). For mirrors with 90% reflectance, the maximum error for large values of c/a will be 1.5 deg.

Test models of the cell and mirror configuration are being fabricated for testing and evaluation. Errors will also be contributed by reflected solar energy from the Earth while the spacecraft is near the Earth. When the range from the Earth's surface exceeds 4000 mi, or when the phase angle exceeds 75 deg, this error will fall below 6 deg.

e. Secondary Sun sensors. The secondary Sun sensor system for *Mariner* B is functionally the same as for *Ranger* and *Mariner* R. The physical configuration will be entirely different, however, with four of the eight detectors integrated into the 4π steradian Sun-sensor assemblies; the other four detectors, plus two of the 4π steradian detectors, will be mounted in two secondary assemblies containing two cells each and their shadow

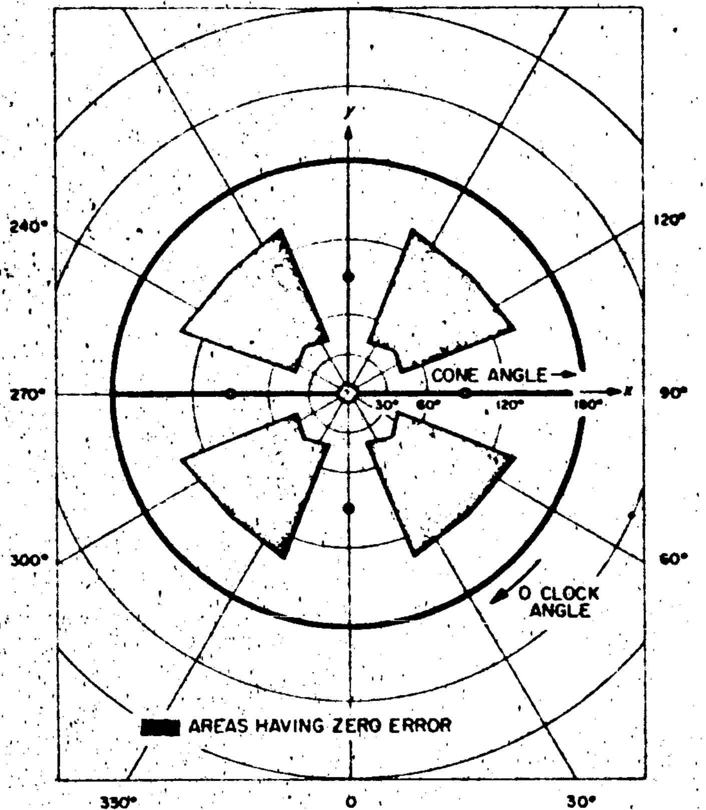

Fig. 37. 4π steradian Sun sensor error diagram

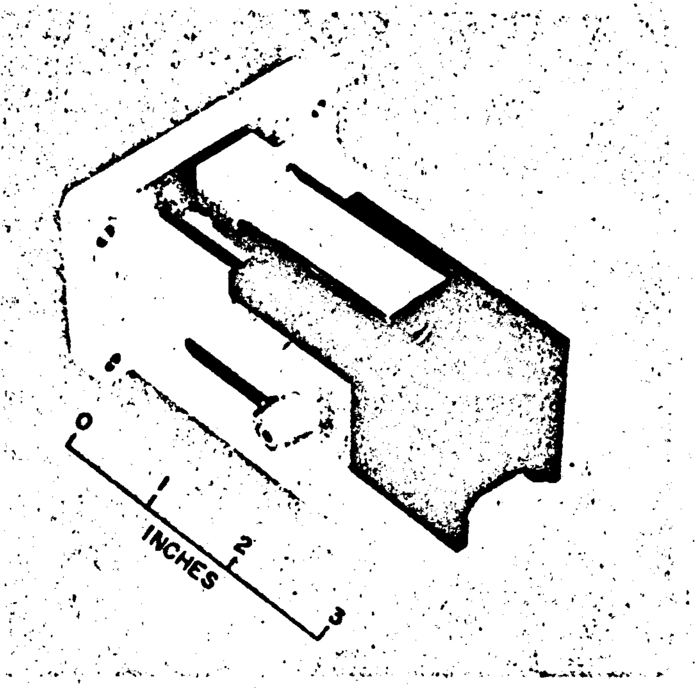

Fig. 38. Sun sensor test fixture

bar. These assemblies will be located on the dark side of two opposed solar panels. Integration of these two sensor systems will result in savings of both space and weight.

f. Guidance Sun sensor. The guidance Sun sensor will be flown aboard *Mariner* B for use during planet approach. Its function is to provide an accurate readout of the angle between the spacecraft roll axis and the Sun line. The angle between the spacecraft roll axis and the spacecraft planet line is determined by the approach planet scanner. These two angles are added to obtain the Sun probe planet angle. Starting approximately 10 days prior to planet encounter, this information will be sampled for use in determining the trajectory correction maneuvers.

The sensor is required to have an output which is linear to ±10% 3 σ over a range of ±10 min. Figure 38 shows a Sun sensor test fixture having an adjustable length shadow bar. This device will be used to determine the optimum length between the cadmium-sulfide cell and the edge of the shadow bar which casts its shadow on the cell. The sensors scale factor increases as the shadow bar length is increased, but not proportionally. This is caused by the fact that the Sun is not a point source and its finite diameter causes the shadow to be less sharp when the shadow bar is moved away from the cell.

Although the test fixture in Fig. 38 is a single-axis device, the flight guidance Sun sensor will be designed to provide error signals about both the pitch and yaw axes.

6. Canopus Simulation

Adequate testing and calibration of the star sensor for use on the *Mariner* B spacecraft requires that a precise simulation be made of the star Canopus. The simulation should provide good collimation. The absolute spectral energy distribution should be within specified limits. The irradiance should be uniform, within specified limits, over the area to be used by the star sensor in testing.

Work has been initiated to provide a laboratory simulation of Canopus with the required characteristics. In a parallel effort, a program has been initiated to more precisely define the spectral irradiance of Canopus outside the Earth's atmosphere. Data from previous spectral measurements made of Canopus and other reference stars from the southern hemisphere are being reduced. It is anticipated that the spectral irradiance of Canopus between 3800 and 5500 A will be specified to an accuracy better than 5%, while outside this region the accuracy will be better than 10%.

The simulator will utilize a high-pressure xenon arc for a source. The spectrum of the source will be modified by suitable filters to more nearly approximate the Canopus spectral distribution. The condenser optics will be all quartz and an off-axis parabola will be used for collimation. The collimated star bundle will be 5 in. in diameter.

To calibrate the spectral irradiance of the Canopus simulator components are being procured to build a spectroradiometer. The spectroradiometer will utilize a Leiss double monochrometer to compare the simulator irradiance with the irradiance from a reference lamp spectrally calibrated by the National Bureau of Standards.

7. Horizon Scanner

Testing of the horizon scanner, previously reported in *SPS 37-9*, has continued. Figure 39 shows the horizon scanner, with the rear cover removed, mounted in a test fixture. This fixture allows precision alignment of the horizon-scanner mounting flanges with respect to a distant simulated planet. By using this fixture the optical axis can be adjusted to coincide with the mechanical axis. The fixture rotates the horizon scanner about its front nodal point to enable calibration of the error-output scale factor.

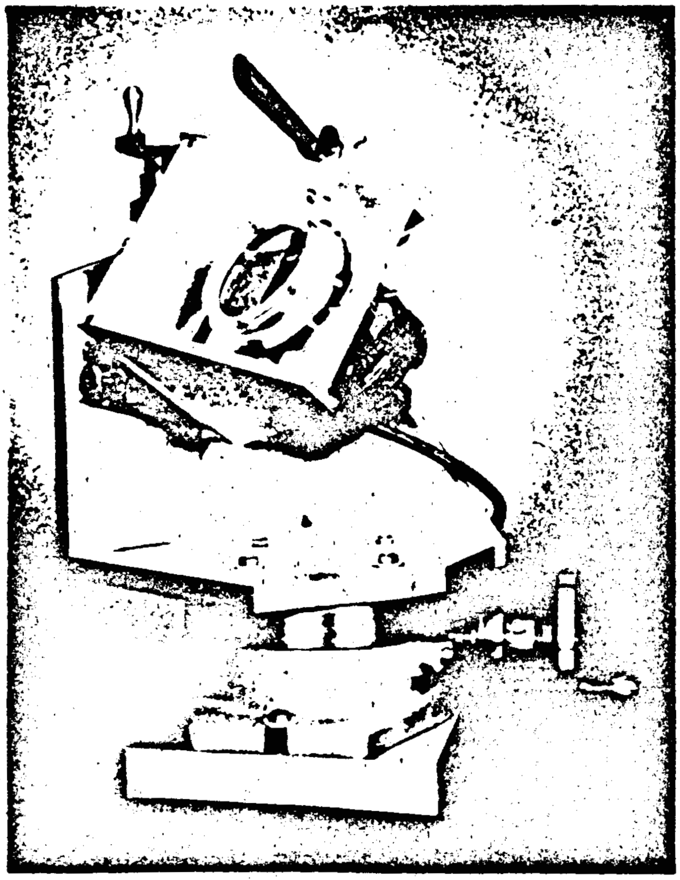

Fig. 39. Horizon scanner

For testing of the horizon scanner for functional performance with environmental simulation, a space background simulator, has been designed and fabricated. Figure 40 shows the horizon scanner mounted in the space background simulator. The simulator consists of an outside wall of foam insulation, a liquid nitrogen shroud, and an interior cavity which can be evacuated to less than 10^{-5} torr pressure. The interior of the cavity is treated to have a high emissivity. The interior surface area is large with respect to the uncooled area where the horizon scanner looks in, thus the simulator appears to be a black body with close to unity emissivity at a temperature of 77°K. The window of the horizon scanner also serves as the window to the simulator. To simulate a planet's radiance against the space background, a small heated conical cavity is located inside the large cooled cavity. The heated cavity can be set at any desired temperature for testing and absolute radiometric calibration of the horizon scanner.

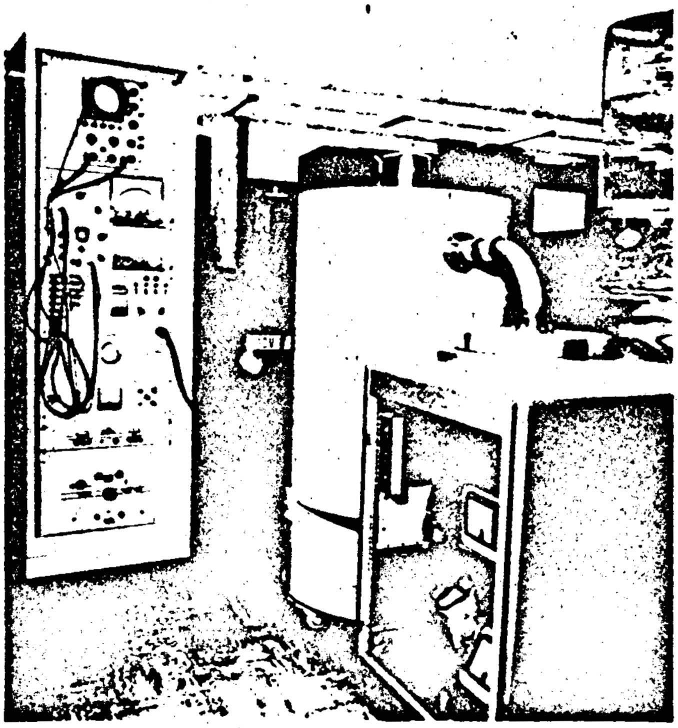

Fig. 40. Horizon scanner test

Preliminary tests with the simulator have confirmed the existence of a space background problem. The nature of the problem is that the over-all efficiency of the optical system (containing five elements of germanium: window, two wedges, objective and detector emersion element, all low-reflectance coated to peak at 12 μ) is approximately 20% for 300°K radiation. When the horizon scanner is looking at a homogeneous background, at a different temperature than the instrument is internally, any variation of the optical efficiency as a function of the wedge angle will result in a change of energy on the detector. This change will give an unwanted signal described as aperture modulation. The effect of this aperture modulation is to reduce the horizon scanner sensitivity by increasing the noise level. An investigation as to the cause of this aperture modulation as a function of wedge angle is being made. In addition, several approaches to compensate for the modulation, such as selected masking of the wedges and/or limiting the spectral response to the region of maximum transmission, are being investigated.

Additional environmental tests have included vibration and acceleration testing of the horizon scanner. Preliminary results indicate no mechanical failures in these tests.

8. Image Dissector

Three image dissectors, previously described in *SPS 37-12*, have been received from the contractor to date. Both functional and environmental testing is proceeding on the tubes. Figure 41 shows the test equipment for functional testing. The image dissector is mounted on a pair of rotary tables in such a manner that each table provides rotation in one axis about an identical point. This point is chosen to be coincident with the center of curvature of the photocathode. An optical image in focus on the curved photocathode will thus remain in focus as the tube is repositioned. A microscope objective is used to form a reduced image, from the slide projector, on the face of the photocathode. For sensitivity measurements, the microscope objective and projector are removed. Light from a National Bureau of Standards calibrated source, located in the lamp housing shown at the end of the bench, is allowed to illuminate the photocathode.

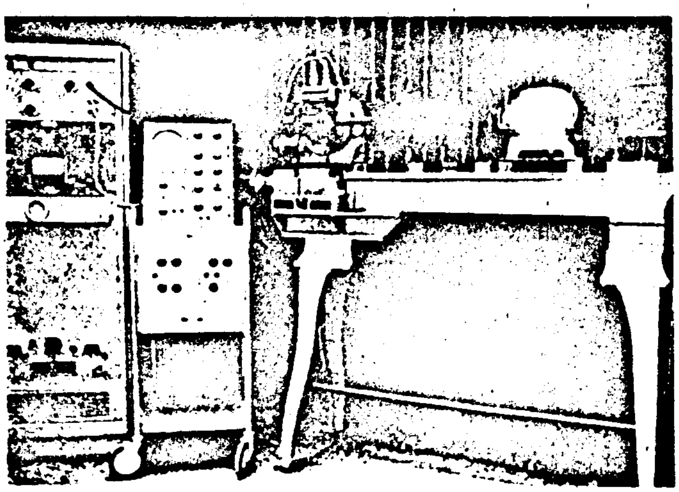

Fig. 41. Image dissector test

Preliminary functional tests have given the following results. The deflection linearity over a ½-in. area of the photocathode is better than 1%. The resolution at the center of the photocathode is sufficient to give 30% modulation of a Bar chart with 2-mil spacing between the alternate black and illuminated bars. At ¼ in. from the center the modulation has decreased to 10% and degenerates badly further out. The useful area of the photocathode is thus considered to be approximately ½ in. and will be more specifically defined by the resolution requirements of the particular application of the tube. Since the sensitive area of the photocathode is approximately 1 in. in diameter, the useful area is determined by the electron optics limitations. The resolution does not appear to be improved by increasing the electron optics accelerating voltage in excess of 600 v.

An image dissector mounted in its housing has been subjected to the design qualification type approval vibration environment. No effects due to this environment were noticeable on subsequent retesting of the tube.

Work on development of a high-temperature photocathode for the image dissector was initiated. The purpose of this development was to provide a tube that would have the capability of withstanding sterilization temperatures (125°C for 36 hr) with no subsequent loss in sensitivity. Several tubes were constructed, using a bialkali photocathode of sodium potassium. These tubes did not meet the required sensitivity, having a response of 5 to 10 μamp lumen (2870°K color temperature incident light) as compared to the 50 μamp lumen from a typical S-11 photocathode. A change in the *Mariner* B design requirements has eliminated the need for sterilization capabilities in the initial systems using the image dissectors. These changes, together with the initial high-temperature photocathode difficulties, have resulted in a decision to proceed with the S-11 photocathode and to continue the high-temperature development effort on a reduced long-term basis.

Some initial studies have been made on the problems of the design of an optical system, with field corrector, to work with the curved (1¼-in. radius) photocathode. These studies have indicated that the use of a fiber optics face plate for the photomultiplier would ease the optical design problem and would also result in improved image quality. Work has been initiated to incorporate a fiber optics face plate into the image dissector.

9. Canopus Tracker

The Canopus tracker is designed to furnish the third axis reference for the *Mariner* B attitude-control system. It is a no-moving-parts device that promises to have the long lifetime necessary for planetary missions.

The heart of the system is an image dissector tube, developed under JPL Contract 950096 by CBS Laboratories. This tube permits a slit-shaped portion (0.004 × 0.070 in.) of a photocathode (0.500-in. diameter) to be instantaneously examined by a 12-stage photomultiplier.

In use, an area of space equivalent to 4 × 32 deg is imaged on the face of the tube by a fast, wide-angle optical system. The 32-deg view angle is positioned on the spacecraft to include all possible Sun–probe–Canopus angles for trajectories roughly within the ecliptic plane. The portion of the cathode along the 32 deg is determined by the Canopus cone angle generator from inputs by CC&S predetermined program and by two modes of ground command backup.

The slit is effectively swept perpendicular to its long axis through 4 deg peak-to-peak by a 20-cps triangular wave. The tube output is a pulse train of 40 pulses/sec whose phase relationship to the sweep voltage determines the error signal about the roll axis. This roll error signal (Fig. 42) is produced by sampling the sweep voltage at the moment of the star pulses and holding this voltage between pulses. The triangular wave shape permits a high degree of rejection of offsets caused by sampling delays, variations in pulse characteristics, and variations in amplitude and frequency of the sweep voltage.

Figure 43 shows the tracker block diagram. Note that an internal signal representing star "color" for additional "identification" is *not* generated. S-11 magnitude and star cone angle (and to some extent cone-angle rate) are the only information used for Canopus identification (available to the star tracker itself). The threshold gates will be set at approximately a factor of ±2.5 from nominal calculated Canopus amplitude. In the event that the wrong celestial object is acquired, command access through the omnidirectional antenna is available as a backup. In this event, a roll override command will be given and the spacecraft will begin a roll search for the next "acceptable" bright object.

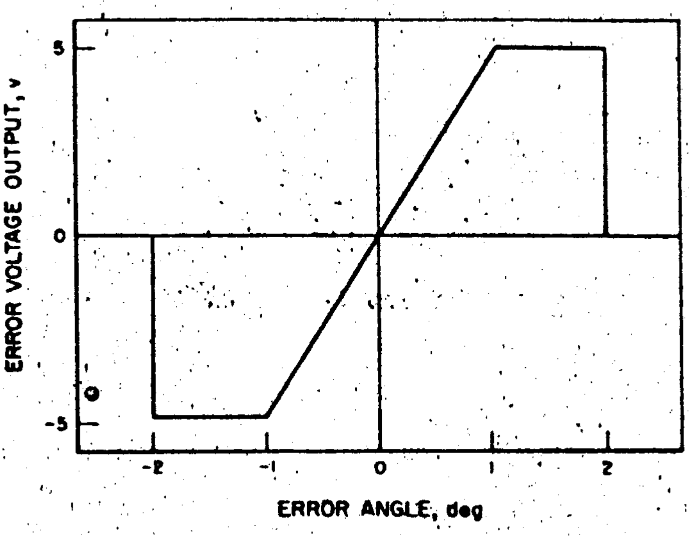

Fig. 42. Roll error signal

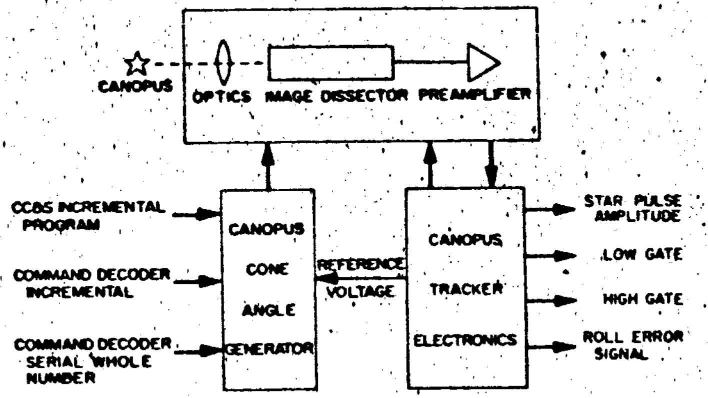

Fig. 43. Canopus tracker block diagram

The Canopus tracker is mechanically packaged in three portions with a total weight of about 7 lb. The tracking head containing the image dissector, optics, 45-deg mirror and lens shade, preamplifier and high-voltage supply is mounted to the side of the integrated guidance package in a special carrier designed to maintain alignment to the planet approach scanner. The two electronics portions, the Canopus cone angle generator and the Canopus tracker electronics are each packaged in *Mariner* B 1.25-in. standard modules. The electronics requires about 4 w of 2400 cps, 50 v rms. The entire tracking head can be rotated to permit different roll null positions and thus different nominal roll attitudes of the spacecraft.

The problems associated with development of the Canopus tracker have mostly concerned the image dissector because of the complexity of the device and the stringent requirements placed on its performance. A problem with optics because of the curved photocathode has been solved with a fiber optics faceplate. A problem with variations of sensitivity of the tube across its face may eventually require a specially graduated filter in front of the tube. A problem with voltage breakdown across the tube base has been solved.

Other problem areas where solutions are in sight are the fast wide-angle optics, mechanical stability and alinement of the tracking head, and electronic stabilities. Stability requirements of all kinds are very severe, not only for attitude control, but primarily for successful solution of planet approach guidance.

The development work has all been done at JPL or under JPL contracts. These include contracts to CBS Laboratories for image dissectors, the Te Company for optics, and DI/AN Controls for the Canopus cone angle generator. During development effort, a request for bids was initiated, with Barnes Engineering Company being the successful bidder for the fabrication and testing of complete Canopus trackers. During the final development effort, Barnes Engineering has their project engineer resident at JPL to ensure a smooth and rapid transition into the production phase for the Canopus tracker.

10. Relating Detector (or Sensor) Response From One Radiant Source to Another Through an Intermediary Standard

If an optical sensor such as a star tracker is to be accurately threshold-calibrated and it is not possible or is inconvenient to calibrate on the actual star, a simulator must be used. Ideally the simulator should have the same absolute spectral "output" as the star outside the Earth atmosphere. This is difficult, since present sources have spectral characteristics much different than a typical star. The following calculations indicate a practical approach of relating tracker response on one source to that on another source through an intermediate calibration (which would logically be the ft-candle or other convenient standard).

Assumptions.

Star or celestial reference "output" at the tracker location

$$k_2 f_2(\lambda) \quad \frac{\text{w}}{\text{cm}^2\mu}$$

Laboratory simulator output

$$k_1 f_1(\lambda) \quad \frac{\text{w}}{\text{cm}^2\mu}$$

Tracker response versus wavelength

$$k_3 f_3(\lambda) \quad \frac{\text{amp}}{\text{w}}$$

Area of collecting optic

$$A \quad \text{cm}^2$$

Star or celestial reference output in ft-candles at the tracker location

$$[930]\, 685 k_2 \int_0^\infty f_2(\lambda)\, V(\lambda)\, d\lambda$$

Simulator output in ft-candles

$$[930]\, 685 k_1 \int_0^\infty f_1(\lambda)\, V(\lambda)\, d\lambda$$

Eye response normalized to 1 at peak

$$V(\lambda)$$

Computations.

For tracker output when operated against simulator to be equal to the same as its output against the star

$$A k_1 k_3 \int_0^\infty f_1(\lambda) f_3(\lambda)\, d\lambda = A k_3 k_2 \int_0^\infty f_2(\lambda) f_3(\lambda)\, d\lambda \qquad (1)$$

and if simulator ft-candle flux equals R times the star ft-candle flux then

$$[930]\, 685 k_1 \int_0^\infty f_1(\lambda)\, V(\lambda)\, d\lambda = [930]\, 685 R k_2 \int_0^\infty f_2(\lambda)\, V(\lambda)\, d\lambda \qquad (2)$$

which implies

$$k_1 = \frac{R k_2 \int_0^\infty f_2(\lambda)\, V(\lambda)\, d\lambda}{\int_0^\infty f_1(\lambda)\, V(\lambda)\, d\lambda} \qquad (3)$$

substituting (3) into (1) yields

$$R = \frac{\int_0^\infty f_1(\lambda)\,V(\lambda)\,d\lambda \int_0^\infty f_2(\lambda)\,f_3(\lambda)\,d\lambda}{\int_0^\infty f_2(\lambda)\,V(\lambda)\,d\lambda \int_0^\infty f_1(\lambda)\,f_3(\lambda)\,d\lambda} \tag{4}$$

The simulator should therefore be set at a ft-candle level that is *R* times the star ft-candle level. When this is done, the sensor response to the simulator will be equal to its response on the star.

Typical values of *R* are shown in Table 9, and are subject to individual variation in detector response, assumed Canopus curve, etc. They are, therefore, correct for published nominal values only.

Table 9. Typical values of *R*

Simulator source type	Tracker response	Celestial reference	R
Xenon	S-11 photomultiplier	Earth	1.334
Xenon	S-11 photomultiplier	Mars	0.876
Xenon	S-11 photomultiplier	Canopus	1.3
Xenon	S-11 photomultiplier	Sirius	1.47
Xenon	S-11 photomultiplier	Vega	1.75
Xenon	S-11 × LRES optics	Earth	1.33
Xenon	S-11 × LRES optics	Mars	0.9
Xenon	S-11 × LRES optics	Canopus	1.28
Xenon	S-11 × LRES optics	Sirius	1.43
Xenon	S-11 × LRES optics	Vega	1.64
Xenon	S-4 × LRES optics	Canopus	1.34
Xenon	S-4 photomultiplier	Canopus	1.31
Xenon	silicon cell × LRES optics	Sun	0.828
Xenon	silicon cell	Sun	0.442
2750°K black body	S-11 × LRES optics	Canopus	2.31
6000°K black body	S-11 × LRES optics	Canopus	1.155
2750°K black body	S-11 photomultiplier	Earth	2.68
6000°K black body	S-11 photomultiplier	Earth	1.162

2. Attitude Control

a. Earth sensor. The *Ranger* Earth sensor is a device which utilizes a variable aperture shadowing technique on three photomultiplier tubes so arranged that their current outputs can be resolved into 2-axis error signals. Previous *SPS* reports have traced the development of the Earth sensor in detail (*SPS* 37-4, -5, -6, -7, and 9): The following discussion is a current look at the *Ranger* Earth sensor noting in particular the test equipment, some test data, performance in *Rangers* 1 through 4, and the development of an Earth sensor light hood.

Figure 29 shows the equipment used to check out the *Ranger* Earth sensor at AMR; Fig. 30 is a block diagram of the test equipment. The short range Earth simulator simulates the Earth at its color temperature, various sizes, and light intensities of the Earth at mid-course and terminal maneuvers. The long range Earth simulator has the added feature of providing various phase angles of the Earth. The short range Earth sensor is mounted on top of a mechanical alinement fixture and a T-2 theodolite (Fig. 29). The Earth sensor can be rotated to any desired angle with respect to the Earth by means of the theodolite, and the mechanical null position of the Earth sensor with respect to the Earth can be determined with the mechanical alinement fixture. The small telescope on the mechanical alinement fixture is adjusted parallel to the mounting reference surfaces on the Earth sensor using autocollimation techniques. Voltage outputs of the Earth sensor are read out of the dynamics meters after the signal has passed through demodulators and simulated loads as would be in the attitude control subsystem. Figure 31 is the final circuit diagram of the *Ranger* Earth sensor.

Figure 32 is the actual Earth sensor plot of roll and hinge voltage outputs versus angle. Table 14 shows typical

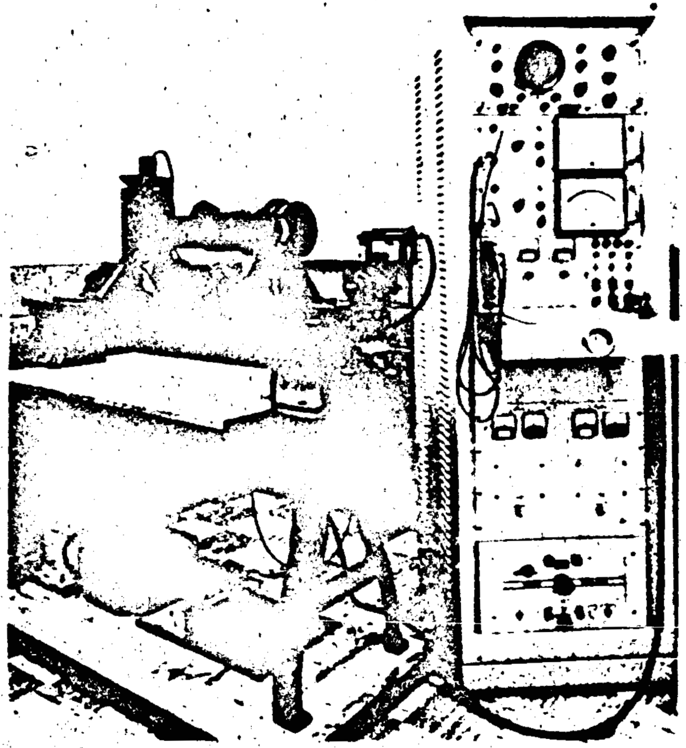

Fig. 29. *Ranger* Earth sensor test equipment

Table 14. Values for third quarter trajectories for *Rangers* 3 through 7

Maneuver	Diameter of Earth, deg	Sun–Earth–probe angles, deg
First acquisition of Earth sensor	12	90 to 140
Mid-course maneuver	4.4	80 to 130
Terminal maneuver	1.9	70 to 130

third quarter values (*Rangers* 3 through 7) of Earth diameter and Sun–Earth–probe angles when the Earth sensor is first turned on, during mid-course maneuver, and at terminal maneuver. The long range Earth simulator was used to simulate the Earth at its approximate color temperature, a Sun–Earth–probe angle of 90 deg as shown in the sketch on the plots, the corresponding light intensities during the respective maneuvers, and the approximate Earth diameters. The rounding of the curves near the saturation points is due to the finite size of the Earth. If the Earth were a point of source of light, the curves would be a straight line saturating at 1.25 deg for roll and 2.5 deg at hinge. The finite size of the Earth causes these intersecting lines to curve in a region of plus and minus the radius of the Earth from the saturation points of a point source. This is readily seen in Fig. 32(a).

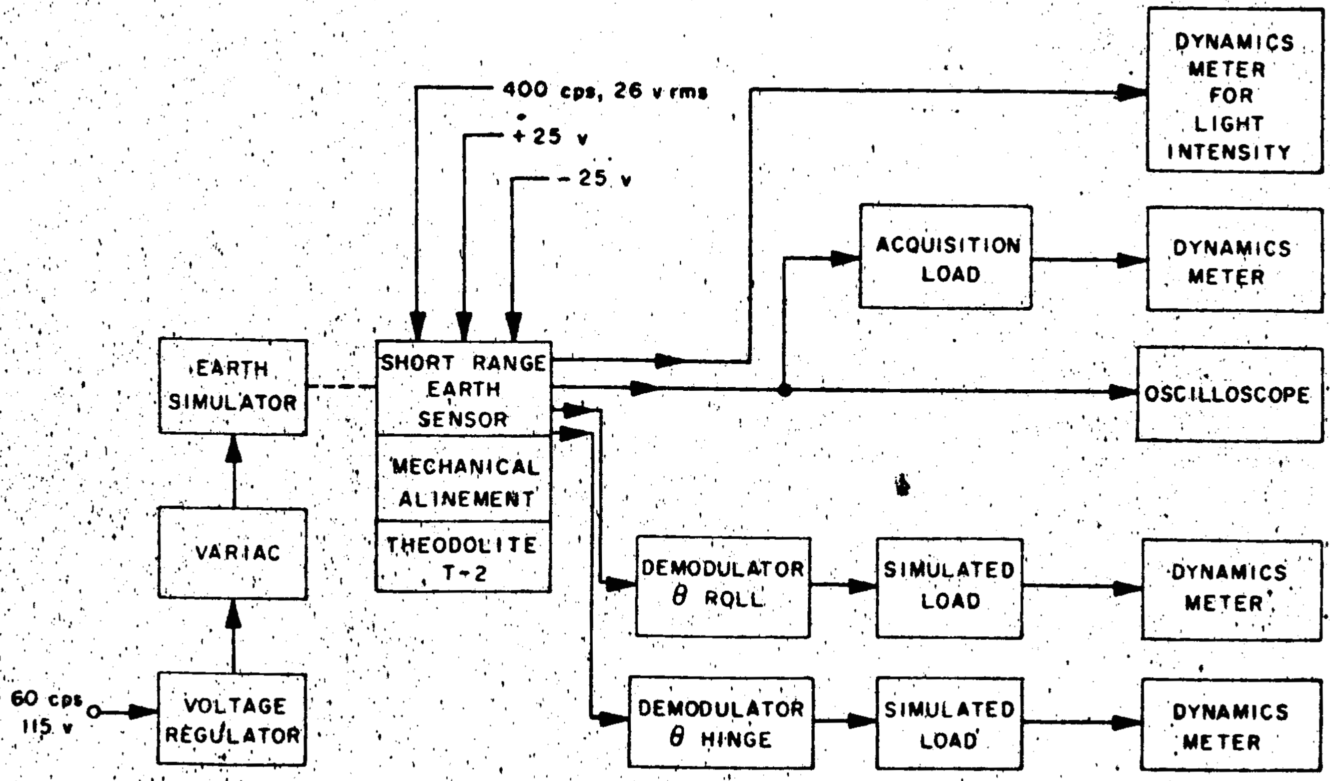
400 cps, 26 v rms
+25 v
−25 v
DYNAMICS METER FOR LIGHT INTENSITY
ACQUISITION LOAD
DYNAMICS METER
EARTH SIMULATOR
SHORT RANGE EARTH SENSOR
MECHANICAL ALINEMENT
THEODOLITE T-2
OSCILLOSCOPE
VARIAC
DEMODULATOR θ ROLL
SIMULATED LOAD
DYNAMICS METER
60 cps 115 v
VOLTAGE REGULATOR
DEMODULATOR θ HINGE
SIMULATED LOAD
DYNAMICS METER

Fig. 30. Test facility for short range Earth sensor

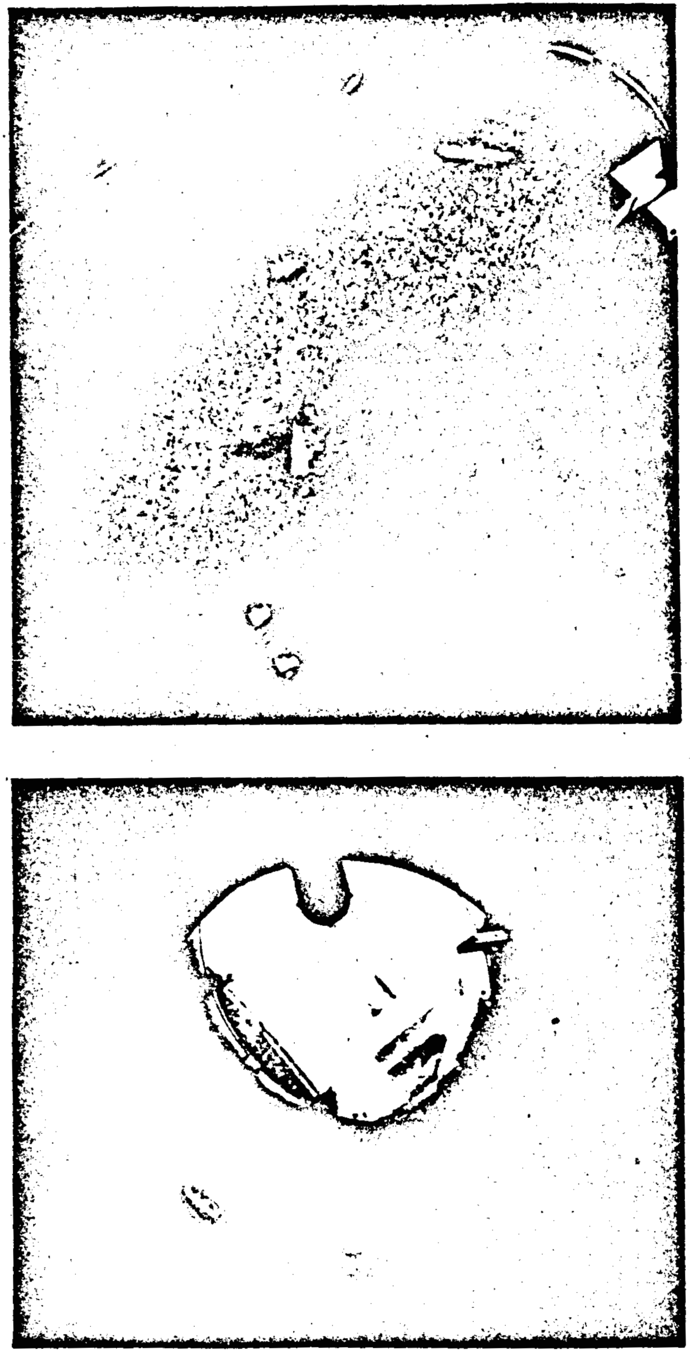

Fig. 48. Mirror (45 deg)

ing when the sky is overcast, and when higher levels of ultraviolet are needed than can be obtained from the Sun through the Earth's atmosphere.

The lamp housings are equipped with removable water cooled apertures; the water cooling is to keep the apertures near room temperature during lamp operation so they do not appear as bright infrared sources.

At present, there are three different apertures available, which simulate the Sun's diameter at Venus, Earth, and at Mars. The highest intensity level is obtained with no aperture on the lamp housing. Intensity levels are:

Aperture	Measured intensity, ft-candles	Percent of desired
None	5500	–
Sun–Venus	3500	12.0
Sun–Earth	2300	18.6
Sun–Mars	1100	16.7

The arc crater is at the primary focus of an elliptical reflector inside the lamp housing, and the aperture is at its secondary focal point. The aperture is also at the focal point of an off-axis parabola, which is 24 in. in diameter. The crater image is then reflected to the front surfaced 45-deg mirror and down to the cement pad in the dome. Figures 48 and 49 show the 45 deg and the parabolic

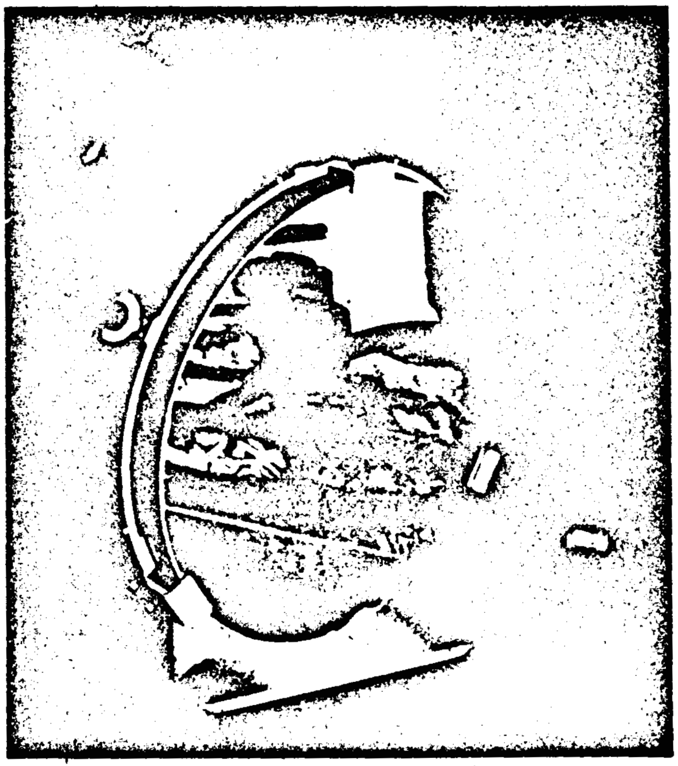

Fig. 49. Off-axis parabolic mirror

Because there is only a half illuminated Earth in the hinge direction in Fig. 32(b), this effect is very much diminished.

The Earth sensor functioned in *Rangers* 1, 2, and 3. On *Ranger* 4 the Earth sensor was never energized. *Rangers* 1 and 2 operated in a low Earth orbit and the Earth sensors indicated acquisition on lighted objects with *Ranger* 1 giving more information, in general. The Earth sensor appeared to be operating correctly even though its temperature was close to the maximum allowable Earth sensor temperature, and the intensity of the Earth was 10 times brighter than expected on normal *Ranger* trajectories.

Ranger 3 provided the first good inflight evaluation of Earth sensor performance. This evaluation indicated that the sensor performed as intended during flight. A spurious pitch command at terminal (Moon distance) caused the spacecraft to pitch in the direction of Earth, eventually bringing the Sun shade between Earth sensor and Earth. This caused a loss of Earth acquisition. From this point on, the spacecraft performance became quite confused and further Earth sensor performance cannot be adequately stated.

Figure 33 is a plot of simulated Earth sensor light intensity data calculated for the *Ranger* 3 flight and light intensity telemetered back from the *Ranger* 3 Earth sensor during flight. The correlation between the two sets of data is good. The simulated data was calculated considering the Earth to be a perfectly diffuse (Lambert) reflector with an Earth albedo of 0.4.

Asymmetrical snow and cloud cover coupled with finite size of the Earth will cause the Earth sensor to have a roll axis error. (Hinge errors are unimportant to guidance.) An estimate of these errors indicates them to be approximately 5% (3σ) of the Earth apparent diameter (approximately 0.1 deg at terminal and 0.25 deg at midcourse.)

The *Ranger* Earth sensor needs a light hood to shade its optics during terminal maneuver for Earth–probe–Sun angles less than 93 deg. The light hood would experience the following rather wide range of temperatures: a maximum temperature needed for heat sterilization of 326°F for 2 hr to a minimum temperature during the cruise phase of flight of −300°F. The light hood must be deformed in shape to fit into the Earth sensor cavity in the *Agena* B adapter. The light hood, combined with all other factors, cannot cause a tipoff rate larger than 3 deg/sec during *Agena* B–*Ranger* separation. Figure 34 is a picture of the *Ranger* 4 light hood in the *Agena* B adapter Earth sensor cavity. Another constraint is that if a light hood is larger than the one used on *Ranger* 4, the light hood will come in contact with the Earth sensor Sun shield when the high-gain antenna is rotated 180 deg to be clear of the mid-course motor firing. Figure 35 is a picture of the *Ranger* 4 light hood at an antenna angle approaching 180 deg. A last constraint is that the Earth sensor must be able to track the Earth to a maximum antenna angle of 145 deg.

The *Ranger* 4 light hood is made out of silastic rubber with thin strips of Teflon film bonded to it at the areas that touch the walls of the Earth sensor cavity in the *Agena* B adapter. This light hood permits ±180-deg yaw angles and an Earth–probe–Sun angle of 73 deg or larger. This hood had undergone a rather thorough test evaluation prior to the *Ranger* 4 flight, and is the most logical light hood to be used on *Rangers* 5, 6, and 7. From preliminary trajectory information, the *Ranger* 4 light hood would permit firing on 17 days out of a possible 21 days.

Other light hoods which would permit more firing days have been and are being designed. A prototype model of a metallic light hood, which would permit an Earth–probe–Sun angle of 65 deg or larger and ±180-deg yaw angles, is being evaluated.

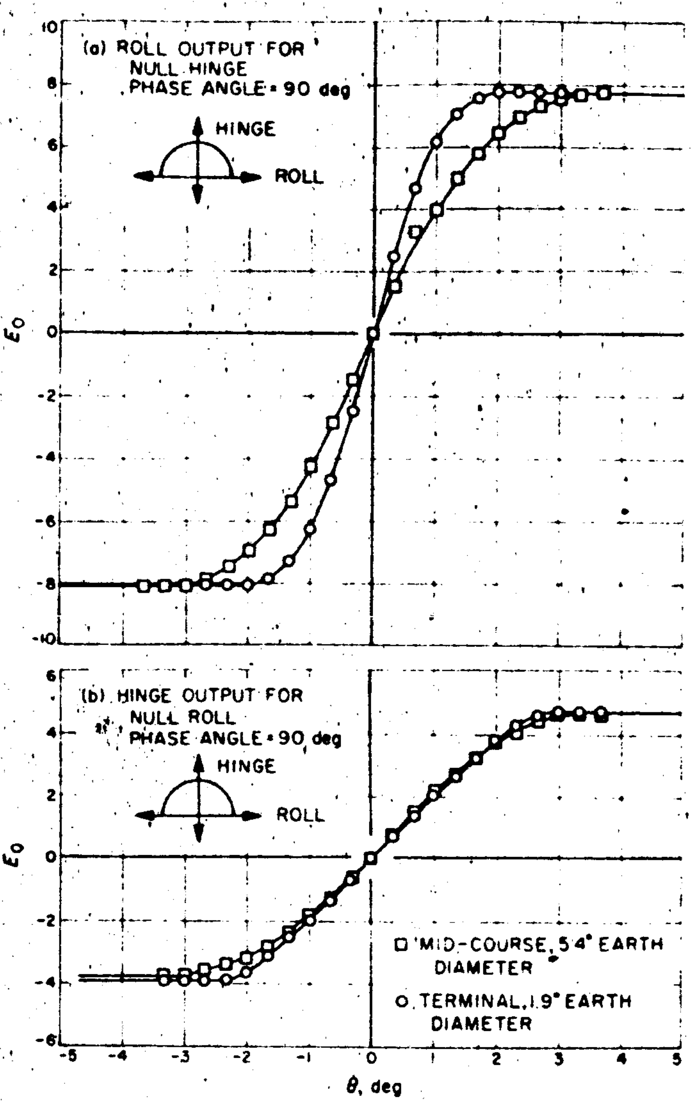

Fig. 32. Roll and hinge output versus θ for Earth sensor

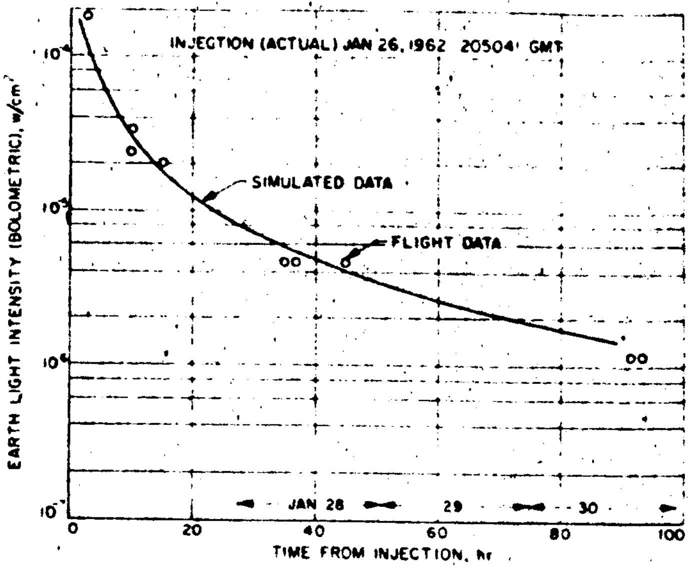

Fig. 33. Simulated and flight data of Earth-light intensity for *Ranger 3*

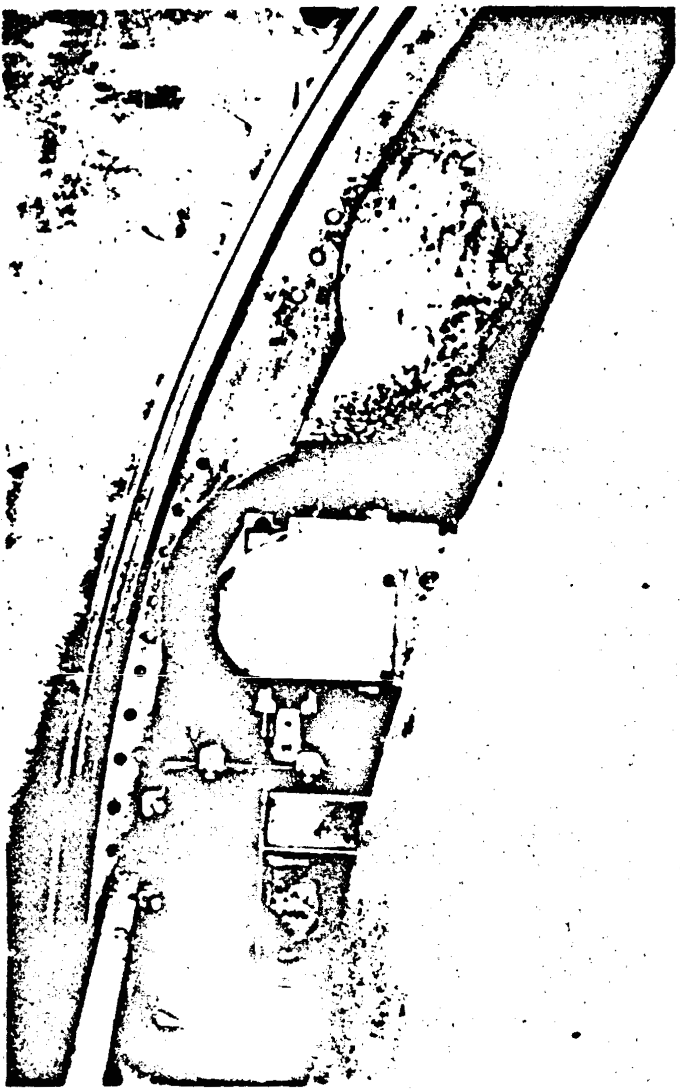

Fig. 34. *Ranger* 4 light hood in the *Agena B* adapter Earth sensor cavity

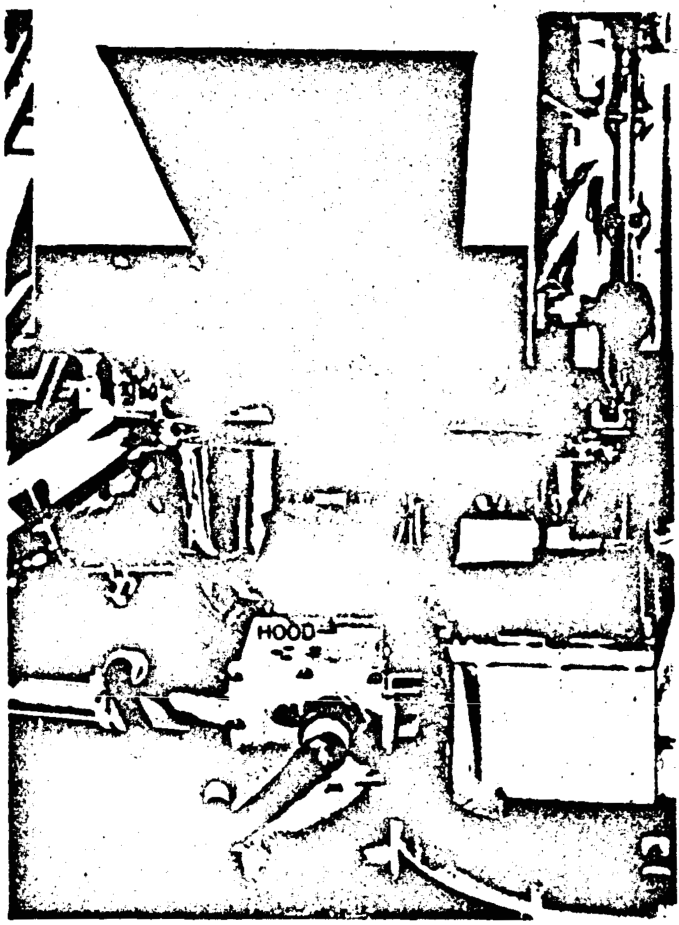

Fig. 35. *Ranger* 4 light hood at an antenna angle approaching 180 deg

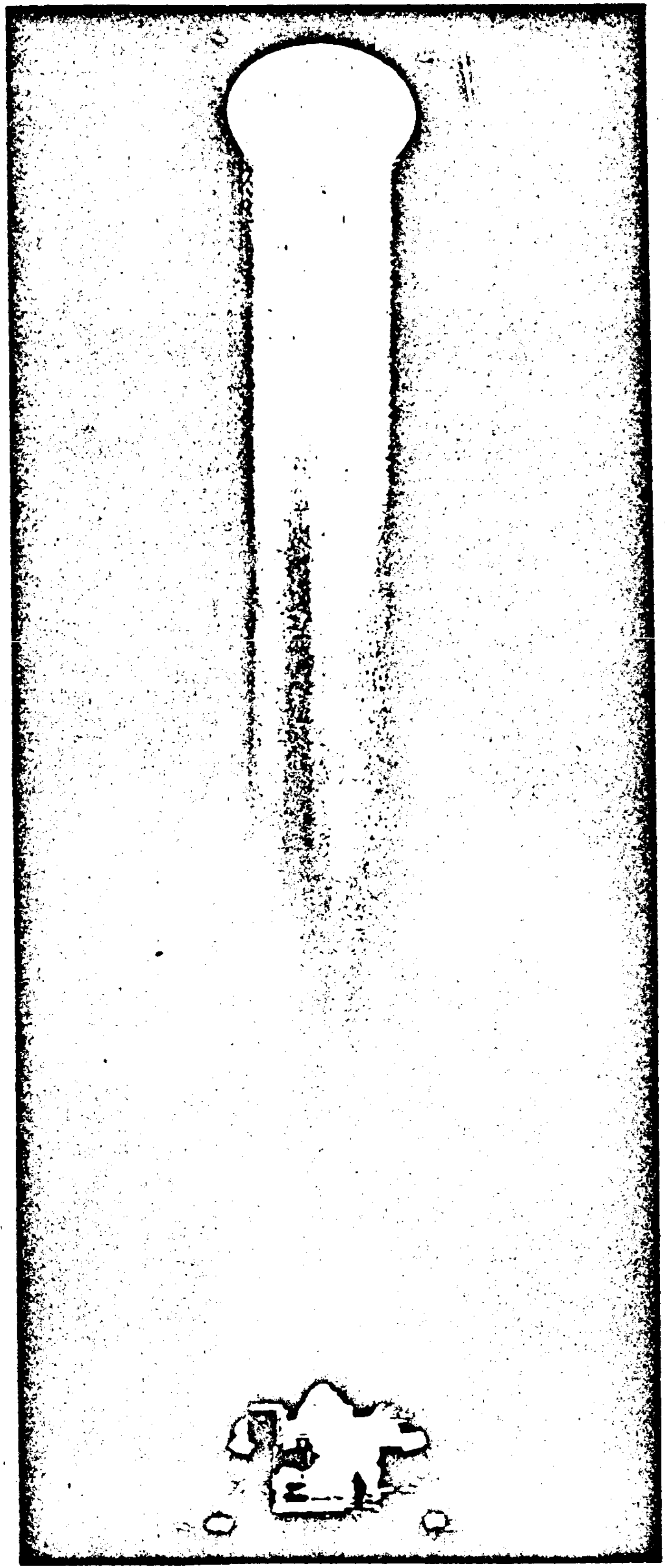

Fig. 46. Illuminated dust particle shaft, celestial simulator building

2. Celestial Simulator Laboratory Test Facility

The celestial simulator building (*SPS 37-5*) has a very high dust particle count. The 24-in. D beam of sunlight, when directed down through the air, results in a bright shaft of illuminated particles (Fig. 46). This particle illumination has interfered with certain critical sensor tests when the sensor is being checked for stray light sensitivity. An indication of the brightness of these particles is given in Table 16.

This level of brightness even at the 0-deg elevation is sufficient to cause the *Ranger* short-range Earth sensor to deliver an acquisition signal. Calculations show that if sensor viewing path lengths are to be held down to 10 cm (sensor within the light beam and looking out), and dust particle background illumination is to contribute only 10% of the Earth sensor threshold level, the brightness must be reduced to 0.03 ft-lamberts (looking through the 24-in. beam). This reduction should be possible through several modifications currently being planned. The modifications are:

(1) Installation of a 3000-ft^3/min blower (10-min air change) to create a positive pressure in the dome, drawing air out at the bottom of the dome, passing it through a bank of 99% efficient filters (at 0.3μ) and returning it to the dome near the top.

(2) Removal of black carpet and installation of black tile floor; since little or no air is introduced into the dome at present, it is felt the carpet is the major cause of the dust problem.

A slight positive pressure seems to exist at present in the dome room since dust particles rise up through the Sun opening in the top. As these particles strike the 45-deg front surfaced mirror, many of them adhere to it, contaminating the surface. Reducing the dust level should reduce the amount of cleaning required for the mirror. This is important since the mirror is not over coated, and its surface is easily scarred by cleaning.

Table 16. Brightness levels as a function of view elevation[a]

View elevation, deg	Early morning brightness, ft-lamberts	Mid-afternoon brightness, ft-lamberts
0	0.10	0.18
30	0.20	0.30
45	0.48	0.62

[a] Solar flux input level = 3500 ft-candles.

3. Sun Sources

a. Heliostat system. Although no spectral distribution curve has been taken as yet, for either the real Sun (heliostat system) or the artificial carbon arc Sun source, foot-candle levels have been measured at the cement pad on the floor in the dome room. Atmospheric contamination determines how accurately the heliostat servosystem will follow the Sun across the sky. The tracking error has been observed to vary from 6 sec of arc on a smog free day to from 30 to 60 sec of arc on a heavy smog day. On days of heavy air pollution, the edge of the Sun's image is not sharply defined, thus the servosystem hunts in seeking the zero error. The flux level using the heliostat system is approximately 3500 ft-candles, or 27.8% of the free space solar constant in ft-candles. This is significantly better than can be produced by the carbon arc simulator at the correct Sun diameter.

Figures 47 and 48 show that the heliostat mirror and the 45-deg mirror are extremely dirty. The heliostat mirror is not pitted to any significant extent, thus cleaning should return it to its original condition. The 45-deg mirror, however, seems to be pitted in spots, and may have to be resurfaced.

b. Carbon arc artificial Sun source. This artificial Sun source was installed to allow tests to be run in the build-

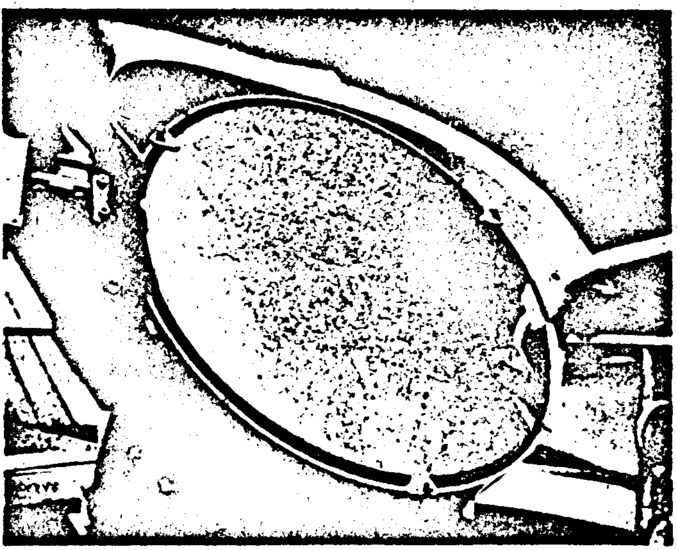

Fig. 47. Heliostat mirror

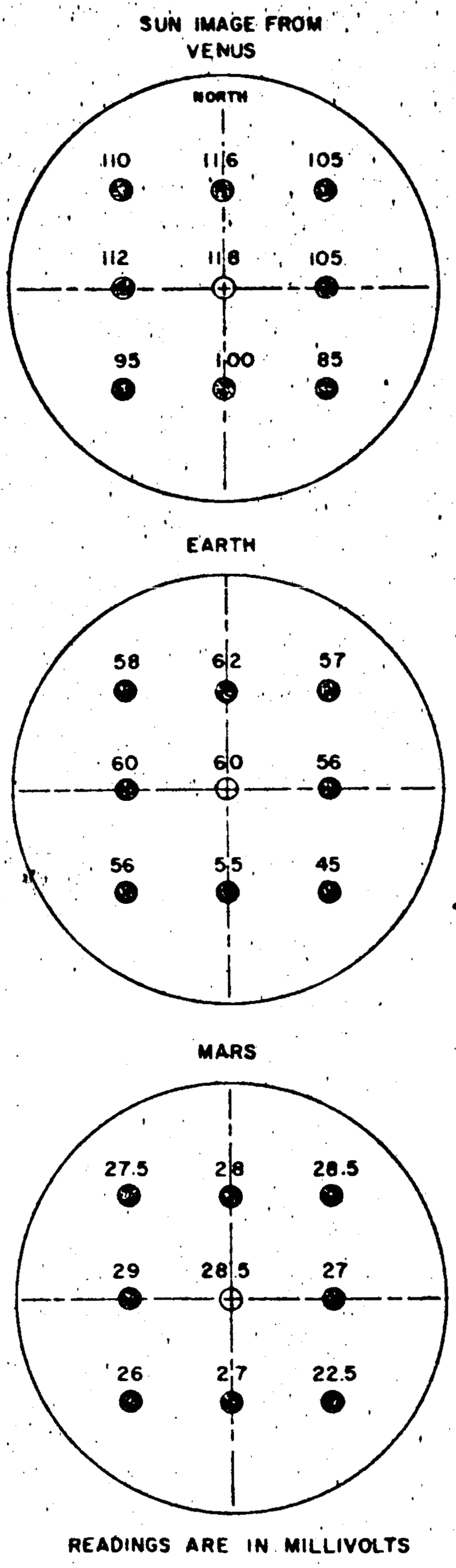

Fig. 50. Variations in flux across simulated Sun source beam

mirror being used with the arc lamps. It is interesting to note that these mirrors, which have not been specially coated to increase reflectance at any particular wavelength, are only 75 to 85% efficient (per mirror) in the silicon solar cell region.

Figure 50 shows relative variation in flux across the simulated Sun source beam. These measurements were taken using the carbon arc Sun simulator and three apertures were used to obtain the size of the Sun as seen from Venus, Earth, and Mars. Readings were taken from a 10-ohm load across the output of a Hoffman silicon solar cell Type 200A. The image was focused on the cell through a 10-in. telephoto lens with an aperture setting of *f*22. For comparison, the same cell and lens setting was used to measure Sun intensity at JPL on July 26, 1961:

Test condition	Intensity readings, mv
Full Sun (outside)	242
Through heliostat (1 mirror)	196
Through heliostat (2 mirrors)	147

4. Celestial Sensor Lab Dark Room Facilities

Dark rooms have been constructed for conducting tests on various sensors and optical breadboarding; these dark rooms had three essential requirements:

(1) Convenience of access between dark rooms and electronic breadboarding technician areas.

(2) Versatility such that varying phases of sensor development could all be handled by the dark rooms.

(3) Several light-tight compartment so that testing could be conducted on many items simultaneously.

These requirements led to the construction of a long dark tunnel divided by four plastic folding curtains. The folding curtains allow each small room to be sealed for individual experimentation. When requirements arise for a long optical shot the four curtains are all pulled aside as shown in Fig. 51.

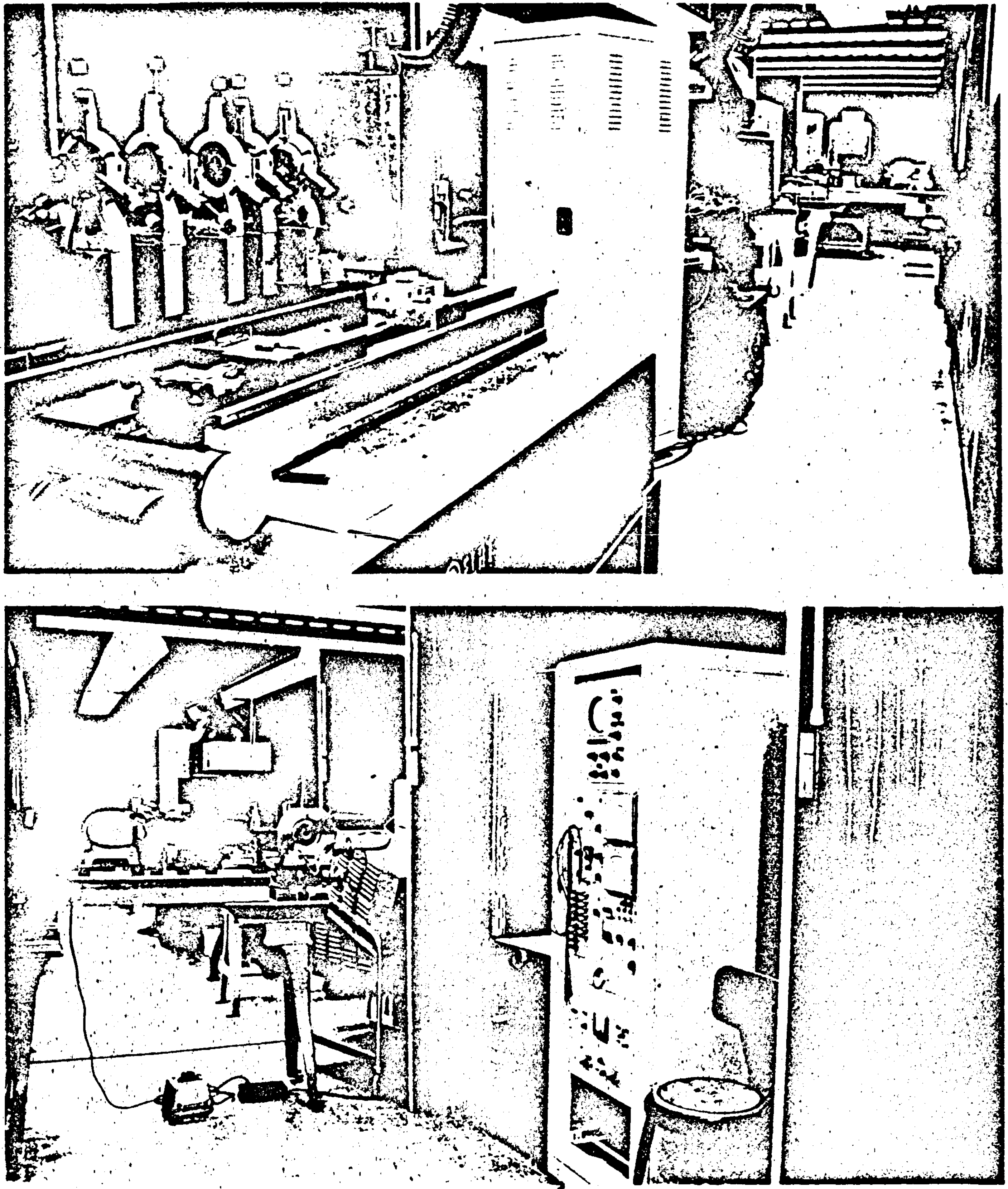

Fig. 51. Dark room facilities across rear section of the celestial simulator building

4. Long-Range Earth Sensor

The long-range Earth sensor (LRES) is affected by off-axis disturbances, to some degree. Extensive testing was performed to estimate and correct this defect. During these tests, additional problems associated with properly simulating the space environment arose. Extraneous light was also reflected from test equipment, dark room walls, and operating personnel so that the results tended to be on the pessimistic side.

During initial testing a problem arose due to the front surface of the vibrating reed being highly reflective. Solution to the problem was twofold: (1) blacken the reed, especially the 45-deg bevel, and (2) introduce wave-shape discrimination into the acquisition channel. The LRES has been qualified and made ready for flight.

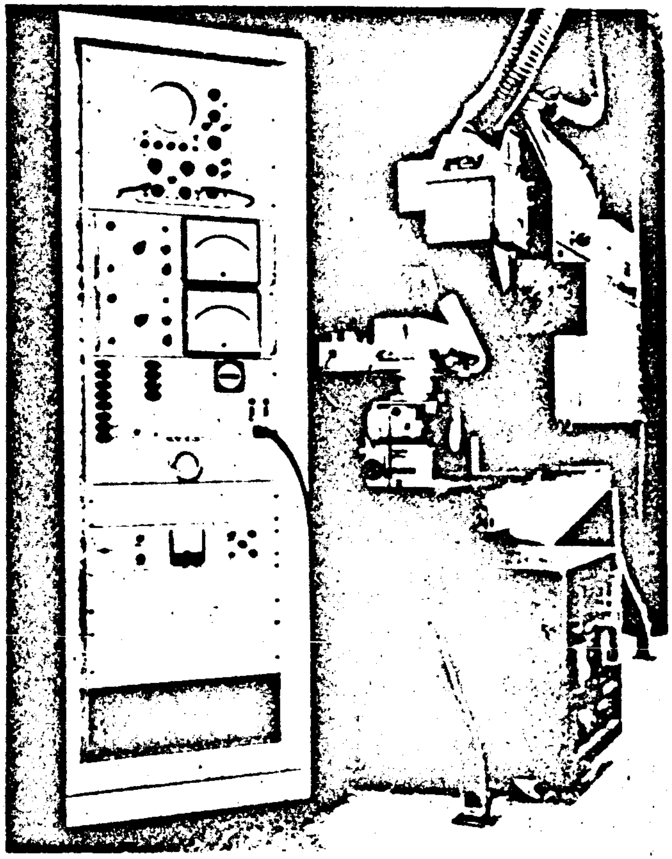

Fig. 7. Long range Earth sensor test equipment

Testing of the LRES is done with an Earth–Moon simulator and a Griswold optical dividing head; the test setup and rack are shown in Fig. 7.

The Earth–Moon simulator (Fig. 8) is a device designed and fabricated by Nortronics to present a simulation of the Earth, Moon and Earth, or a star. The simulator provides the means with which to determine accuracy of alinement and flux level response. Continuous variable levels of irradiance are available for discrete distances from the Earth. There are provided five different Earth-phase positions for the larger size diameter Earth. The simulator provides a 5-in. diameter collimated light which is good to 5-sec-of-arc accuracy with reference to the point source. Earth diameters from 5.411 to 0.000452 deg can be simulated (in discrete steps), and variations in flux are possible over a range of 159.7×10^{-6} to 1.12×10^{-12} w/cm^2.

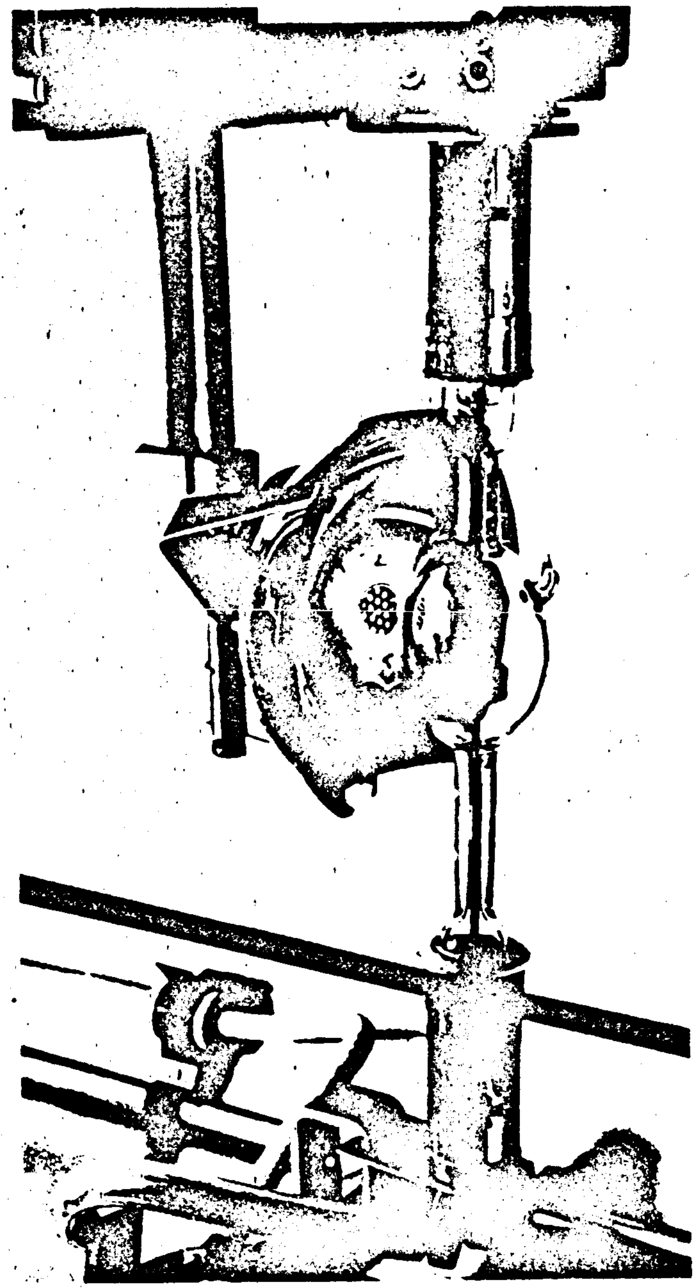

Fig. 8. Earth–Moon simulator light source and reflector

0
1
2
3
INCHES

Fig. 2. Redesigned Earth sensor

C. Guidance and Control

1. Ranger Earth Sensor

The *Ranger* Earth sensor, previously described in *SPS 37-16*, Vol. I, has been modified for missions starting with *Ranger 8*. A very large field of view (40 × 60 deg) had been incorporated into the earlier units so that changes in acquisition preset hinge angle would not be necessary during any launch period. The large field of view, however, presented many constraints to the *Ranger* terminal maneuver and picture-taking mission. In order to circumvent these constraints, the field of view has been reduced to 10 × 20 deg for the *Ranger 8* and all subsequent missions. A 9-position antenna preset hinge angle update system has also been incorporated to make the small field of view possible.

Fig. 2 is a photograph of the redesigned Earth sensor. A series of evaluation tests were performed on the redesigned Earth sensor to verify the modification. The evaluation tests consisted of a dynamic offset response curve, null-axis response data at light intensities which correspond to Earth-sensor first turn-on, mid-course maneuver and terminal maneuver, Earth-probe-Sun angle measurements, light reflection tests from the spacecraft into the Earth sensor, and type-approval environmental tests. The redesigned Earth sensor passed all the tests.

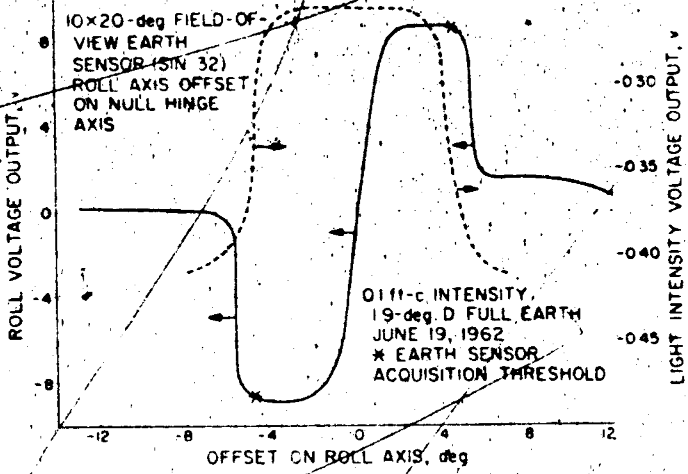

Fig. 3. Error signal and light intensity vs roll angle

Fig. 3 shows the effect of roll-axis angular offsets at a null hinge angle; it includes roll-error voltages, Earth-sensor light intensity voltage outputs, and acquisition threshold points of the reduced field-of-view Earth sensor. The redesigned Earth sensor can operate safely within tolerance at an Earth-probe-Sun angle during terminal maneuver of 47 deg or larger. Previously modification on the Earth-probe-Sun angle constraint during terminal maneuver was 75 deg or larger. The reflection measurements indicate that the maximum antenna angle during Earth search is 140 deg; previously, it had been 120 deg.

Fig. 4 shows the effects of light reflection into the 40 × 60-deg field-of-view design and into the reduced

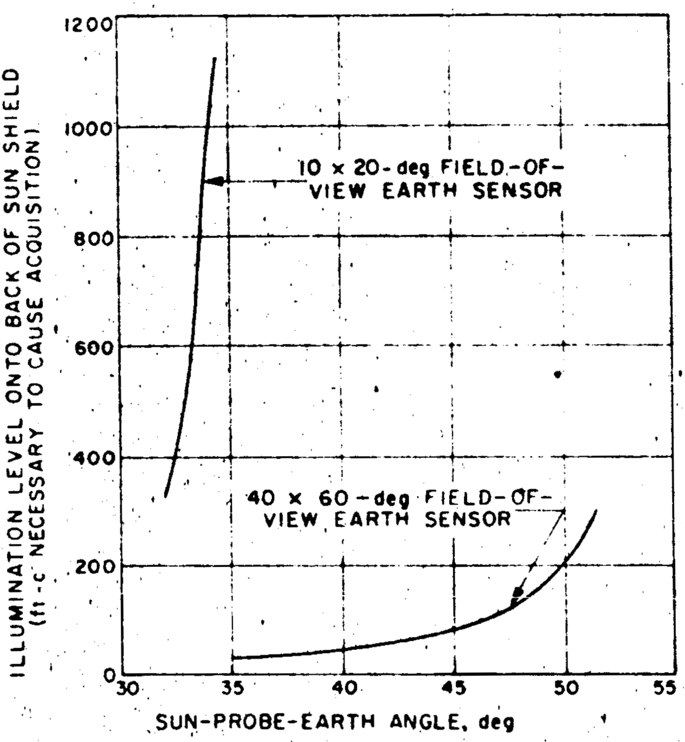

Fig. 4. Sun-shield back-side-illumination Earth-sensor disturbance vs hinge angle

field-of-view Earth sensors that are intense enough to produce an acquisition signal in the Earth sensors.

In summary, Earth-sensor performance in the presence of off-axis disturbances has been greatly enhanced by reduction of field of view.

2. Long Range Earth Sensor, Mariner 2

The *Mariner 2* long range Earth sensor (LRES) previously described in *SPS 37-6, -9, -14,* and *-16,* Vol. II, performed very well during the Venus 1962 mission.

The LRES uses a single, end on, ¾-in. diameter, S-11 photocathode Dumont photomultiplier tube and a 22-cps vibrating reed light chopper in its mechanization. A 2-in. diameter $f/1$ lens images the Earth on the reed which is shaped so that, essentially, phase yields roll error information, and pulse width (minus a constant) is proportional to hinge error. To hold angular scale factors constant over a very large dynamic range of Earth illuminance, photomultiplier output pulse amplitudes were held constant at about ¼ μamp through a high voltage regulation loop. This very low current output also assured an extremely long photomultiplier tube life. Threshold of the LRES was set at 4.17×10^{-6} ft-c to prevent interference from bright stars (approximately a factor of 10 greater sensitivity was actually available). Maximum Earth flux on a typical mission is approximately 0.1 ft-c, which yielded a useable dynamic range of flux input of 24,000.

The 165° F in-flight temperatures near encounter far exceeded design limits; however, the large sensitivity margin (a factor of 7.6) enabled Earth tracking considerably past encounter. Actual drop-out occurred at an Earth range and phase of 86.6×10^{6} km and 45.5 deg, respectively. Computation of Earth flux at this point indicates a loss in sensitivity (due to the very high temperatures) of a factor of 3.1.

The LRES dependably and accurately delivered its 2-axis angular error signals to the attitude control system for the duration of the mission. There was, however, one perplexing discrepancy during the early days of the mission. For engineering evaluation of the LRES, a telemetry readout proportional to the servoed high voltage (indicating apparent Earth illuminance) was included. At first acquisition this telemetry readout indicated that one of the following problem conditions existed:

(1) LRES sensitivity had fallen by a factor of 94.

(2) Telemetry calibration was in error.

(3) The LRES had locked on the Moon.

A very exhaustive series of tests was run to determine which one of these conditions was in effect, and why. A summary of the testing is presented in the following:

Problem 1: Loss of sensitivity due to adjacent dynode elements shorting together in the photomultiplier tube used as a detector in the LRES.

Test. Of the ten dynodes in the photomultiplier tube, various combinations of dynodes were shorted together while the LRES was being operated. A simulated Earth of the same size and brightness as calculated for that particular time was used. The Earth brightness voltage was monitored on a test rack to detect an indication similar to that obtained in the telemetered data of the actual flight.

Result. There were no combinations of dynode shorts which would give a loss of sensitivity exactly as shown on the actual telemetered data.

Problem 2: Loss of sensitivity due to contamination of the front lens of the LRES or of the reflecting mirror in the Earth sensor hood from the *Agena B* fuel ejection during separation.

Test. Tests were performed at Lockheed, Sunnyvale, with the *Agena* booster ejecting fuel vapor. Measurements of the vapor density were made at various distances from the booster.

Result. This test was witnessed by JPL representatives, and the results verified the initial assumption that the maximum contamination caused by the fuel vapor impinging on the spacecraft was so small that it would not be a possible source of trouble for the LRES.

Problem 3: Dust particles contaminating the mirror and front lens causing a loss of sensitivity.

Test. Talcum powder was sprayed into the opening of the LRES hood to coat the mirror and front lens in varying degrees.

Result. Nothing definite could be concluded from this test.

Problem 4: Contamination or degradation in the quality of the mirror, lens or photomultiplier tube from the "new" radiation belt (electron bombardment).

Test 1. The lens system was exposed to a cobalt radiation field and also to an electron bombardment field at Atomic International's facility, Canoga Park. The lens system was given a transmission test before and after each radiation dose with a dosage accumulation from 450 to 23000 rads.

Result. The transmission quality of the lens changed in varying degrees as it was exposed to the radiation field:

Accumulated radiation, rad	Relative transmission, %
450	100
3,450	84.4
13,450	68.0
23,450	54.4

The spacecraft was only exposed to the "new" radiation belt for a few minutes; therefore, the accumulative dosage would not exceed 3000 rad. The drop in transmission quality was due to the discoloration effect on the lens surface. This discoloration would gradually disappear when the lens is exposed to temperatures over 100°F for a period of time depending on the actual temperature and the amount of the radiation dosage accumulated. The Sun's rays could also eliminate the discoloration of the lens.

Test 2. The mirror was put through the same radiation tests as the lens system. The reflectivity of the mirror was checked before and after each test.

Result. There was no measurable change in the reflectivity of the mirror in any of these tests.

Test 3. An electron bombardment test was performed on the following items and each item was tested before and after the test for any change in component quality:

(1) Lens, 7500 rad

(2) Mirror, 3000 rad

(3) Photomultiplier tube, 3000 rad

(4) Transistor 2N1711 (2), 3000 rad

Result. The relative transmission of the lens did not change; the reflectivity of the mirror did not vary; the sensitivity of the photomultiplier tube remained the same; and the transistors were checked for beta, V_{co}, and V_{cbo} and showed no measurable change.

Problem 5: A saturated preamplifier in the Earth sensor could cause the sensitivity to appear low.

Test. The Earth sensor was operated looking at a fairly bright simulated Earth to saturate the preamplifier, and then the intensity was gradually decreased while the Earth brightness voltage was being monitored. When the Earth sensor was looking at the bright simulated Earth, the power to the Earth sensor was turned on and off several times to see what effect this would have on the preamplifier.

Result. Although the preamplifier was saturated, it would not stay in the saturated condition with a decrease in light intensity, and the sensitivity encountered in the actual flight data could not be duplicated. This possibility, although *very remote*, probably is *relatively* the most likely cause of the difficulty.

Test 2. A breadboard of the preamplifier was fabricated with the proper input and output impedance. A simulated signal was injected into the preamplifier, and the operating parameters were changed by varying the resistor and capacitor values. The input signal to the preamplifier was also varied as the output of the preamplifier was being monitored.

Result. Although the preamplifier was made to saturate, it would not stay in this condition without a large input signal. Decreasing the resistor values gave the proper loss of sensitivity, but in order for the resistance to decrease to the proper value the temperature would have to go below zero deg. The actual temperature during the period in question varied from 81 to 94°F and climbed much higher with time.

Problem 6: There was a possibility that the Sun's reflection on the spacecraft and its associated components reflected enough stray light to the Earth sensor to give a low Earth brightness output voltage.

Test. The *Mariner R-3* spacecraft was set up in the celestial simulator so that the simulated Sun would illuminate the spacecraft in the proper direction. The antenna, with the Earth sensor mounted on the antenna yoke, was moved in the hinge axis through its traveling range. The Earth brightness output voltage was monitored on the test rack during this test.

Result. There was a 10% drop in the Earth brightness voltage, but this was just a fraction of what was being sought. There were more reflections from the walls and floor of the simulator room shining into the Earth sensor than from the spacecraft proper.

Tests will continue to be made as new ideas and theories are generated. So far, nothing has actually produced the same Earth brightness readings which were encountered in flight.

The command for the midcourse maneuver was delayed 1 day to see if there would be any changes in the low Earth brightness reading. No changes occurred, so the command to initiate the midcourse maneuver was sent to the spacecraft. After the midcourse maneuver was completed, the Sun sensors orientated the spacecraft so that the extended solar panels would face the Sun again. The Sun gate triggered the relay to apply power to the LRES. After a 24-min roll search, the Earth sensor acquired and locked onto the Earth. The telemetered Earth brightness data still indicated that the sensitivity was very low. As the days passed, the telemetered Earth brightness was gradually decreasing to the point where it would lose Earth acquisition. After 26 days of operation, on September 29, 1962, the LRES lost Earth acquisition, but only momentarily, and then reacquired the Earth. The telemetered Earth brightness reading jumped up to the proper calibration level indicating normal operating conditions as shown in Fig. 3.

Fig. 4 shows that after this transient had occurred, the Earth brightness curve followed closely the calibration curve up to the 72nd day of flight. The deviation of the actual flight curve after this time was due to the temperature rise in the Earth sensor. The spare Earth sensor, Serial 3, was given a temperature versus Earth brightness output voltage test to see exactly how much the temperature affected the Earth brightness readout. Table 3 gives the results of this test, and it shows that although there was very little change from 70 to 130°F, there was a very

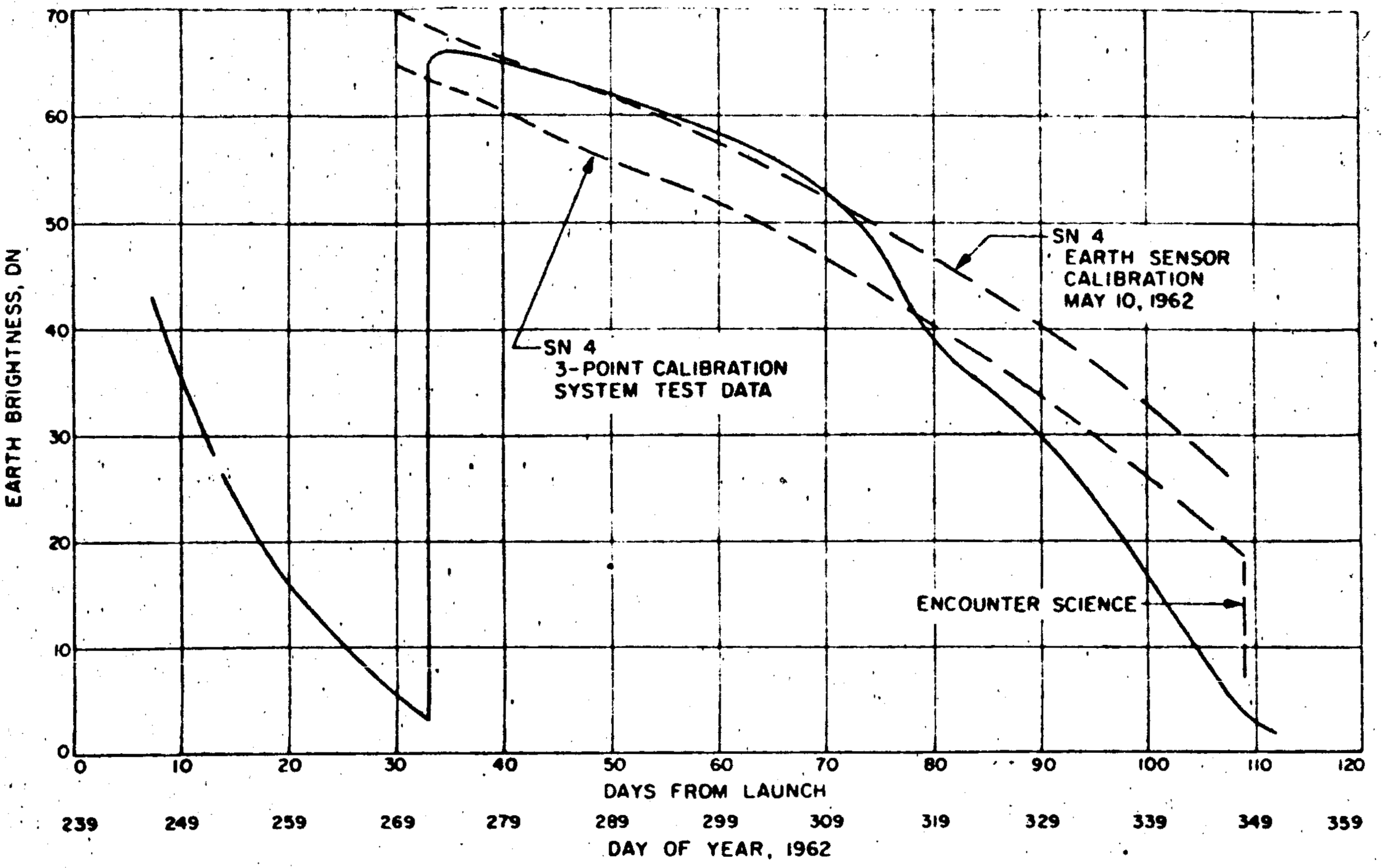

Fig. 3. Average Earth sensor intensity versus time

noticeable change at 150°F. At this temperature the Earth brightness output reading changed approximately 0.2 v, which is equivalent to about 8 DN on the graph. As shown in Fig. 5, the temperature went from 130 to 150°F between the 330th to 340th day. Also of interest are the daily fluctuations of the telemetered Earth brightness data which varied $\pm 9.2\%$ as seen in Fig. 6. This daily variation was concluded to be due to the different surface and cloud condition of the Earth.

Table 3. Temperature test, LRES Serial 3

Temperature transducer, °F	Earth intensity (simulator), w/cm²	Earth brightness output voltage, v
70	5×10^{-7}	−0.57
70	5×10^{-9}	−1.1
70	1×10^{-10}	−2.02
90	5×10^{-7}	−0.60
90	5×10^{-9}	−1.2
90	1×10^{-10}	−2.05
110	5×10^{-7}	−0.59
110	5×10^{-9}	−1.15
110	1×10^{-10}	−2.05
130	5×10^{-7}	−0.625
130	5×10^{-9}	−1.23
130	1×10^{-10}	−2.18
150	5×10^{-7}	−0.638
150	5×10^{-9}	−1.25
150	1×10^{-10}	−2.22

The calculated Earth brightness with respect to time as the distance from the Earth is increased is shown in Fig. 7. This calculated curve as compared with the actual telemetered Earth brightness curve is shown in Fig. 8 as a percentage deviation during the flight, to 110 days. The deviation could not be calculated past 110 days, because the telemetered Earth brightness signal had reached saturation.

The LRES operated extremely well considering the unexpected high temperatures which it had to withstand. The Earth sensor was originally designed to operate in the region between 32 and 100°F. The temperature at

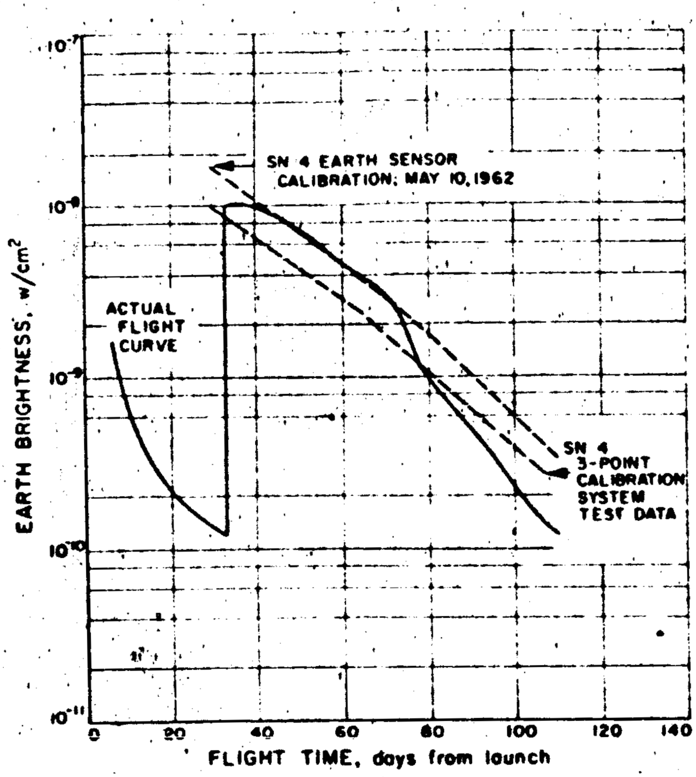

Fig. 4. Earth sensor intensity versus time

closest approach to Venus was estimated to be 165°F, as shown in Fig. 5, which is 65°F higher than anticipated. This was an estimated temperature because the particular temperature transducer used on the Earth sensor saturated at 143°F. The temperature probably went higher than 165°F for the LRES as the spacecraft passed Venus to orbit around the Sun.

In the immediate region of encounter, the Earth-probe-near-limb of Venus angle became quite small (Earth setting behind Venus). This was the cause of some concern since tests (*SPS 37-16*, Vol. II, p. 15) indicated Earth lock would be lost under certain conditions of angle and Venus intensity. Although none of the tests shown were violated, the approach was close enough to indicate limits to give rise to concern about loss of lock. Table 4 indicates the angles and intensities actually encountered in flight. In particular, it is interesting to note that a Venus/Earth intensity ratio of 164,000, only 29 deg off axis, did not cause loss of Earth lock.

The Earth sensor operated satisfactorily up to January 3, 1963, which was almost 3 weeks past the time of closest approach to Venus.

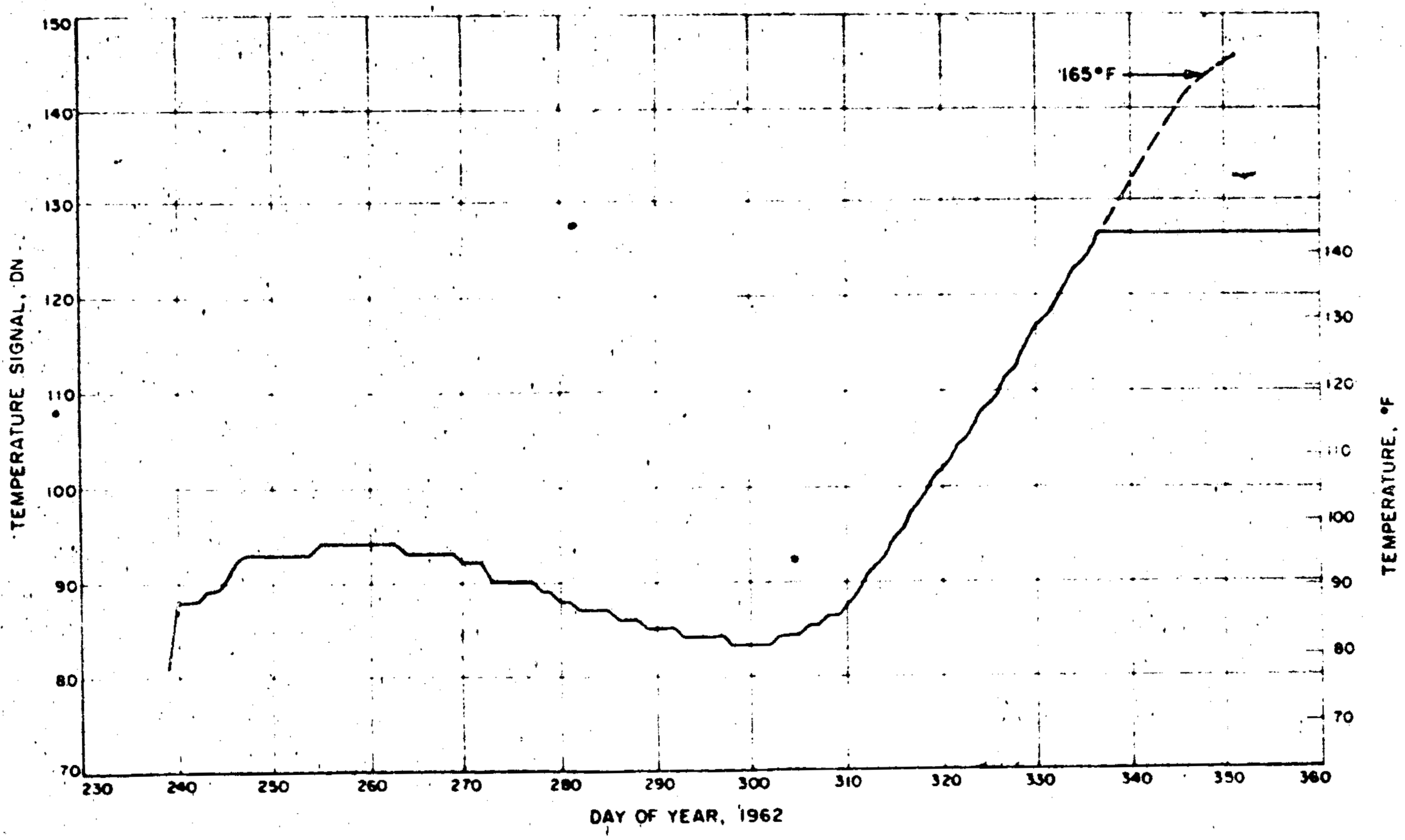

Fig. 5. *Mariner 2 Earth sensor temperature telemetry data*

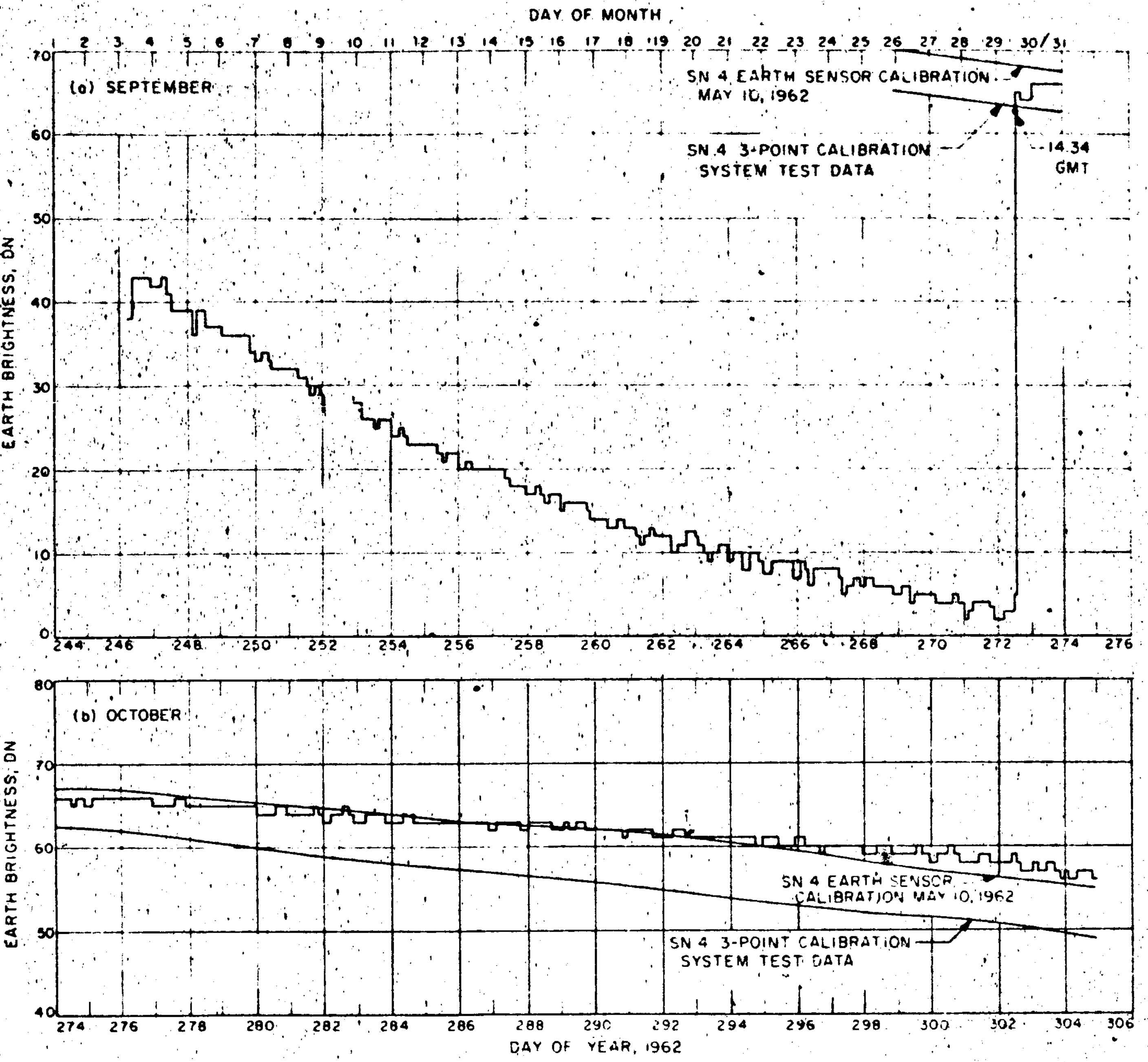

Fig. 6(a,b). Earth sensor intensity versus time

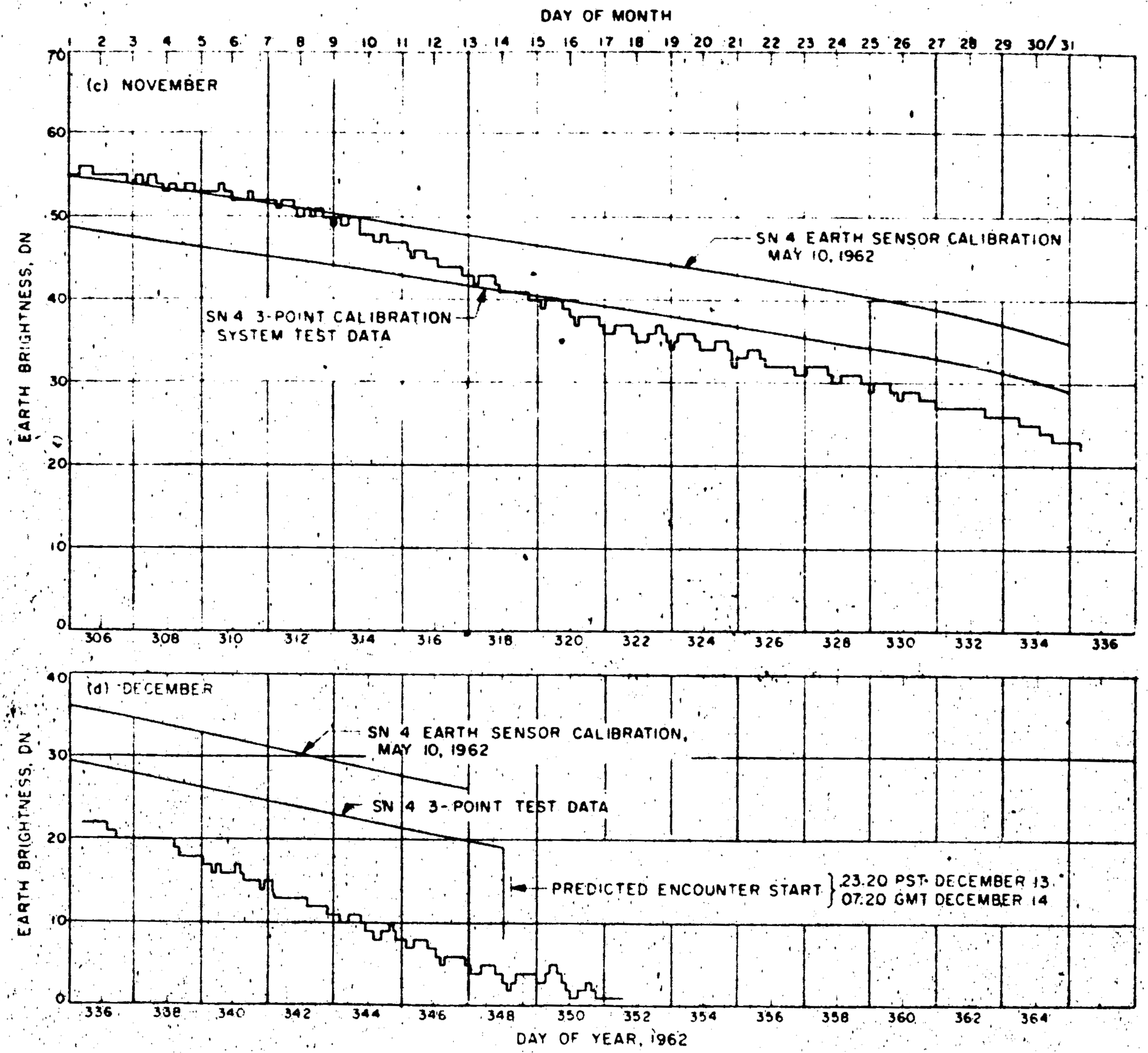

Fig. 6(c,d). Earth sensor intensity versus time

Table 4. Venus–Earth encounter parameters

Time from closest approach, hr	Earth–Probe–near-limb of Venus angle, deg	Venus–Probe distance, km × 10^3	Phase angle, deg	Distance in radii	Venus intensity, w/cm^2	Earth versus Venus intensity ratio
−2	163	58	114.94	9.2	1.13×10^{-4}	$1:2.6 \times 10^5$
−1.5	153	50	108.64	7.8	1.94×10^{-4}	$1:4.5 \times 10^5$
−1.0	140	44	100.00	6.9	2.24×10^{-4}	$1:5.2 \times 10^5$
−0.5	124	41	88.53	6.4	5.67×10^{-4}	$1:1.3 \times 10^6$
0	106	40	74.80	6.3	8.64×10^{-4}	$1:2.0 \times 10^6$
0.5	91	42	61.12	6.0	1.08×10^{-3}	$1:2.5 \times 10^6$
1.0	78	46	50.31	7.2	1.11×10^{-3}	$1:2.55 \times 10^6$
1.5	67	52	43.52	8.1	9.72×10^{-4}	$1:1.88 \times 10^6$
2.0	60	60	40.04	9.4	8.10×10^{-4}	$1:2.17 \times 10^6$
4.0	42	97	39.26	10+	7.56×10^{-4}	$1:1.75 \times 10^6$
6.0	35	136	42.83	10+	1.44×10^{-4}	$1:3.3 \times 10^5$
8.0	31	176	44.51	10+	8.93×10^{-5}	$1:2.05 \times 10^5$
10.0	29	216	45.75	10+	7.08×10^{-5}	$1:1.64 \times 10^5$
12.0	27	256	46.71	10+	3.95×10^{-5}	$1:9.15 \times 10^4$
14.0	25	332	47.49	10+	2.46×10^{-5}	$1:5.7 \times 10^4$
16.0	24	374	48.13	10+	2.09×10^{-5}	$1:4.84 \times 10^4$
18.0	23.6	417	48.67	10+	1.65×10^{-5}	$1:3.8 \times 10^4$
20.0	23.1	460	49.14	10+	1.43×10^{-5}	$1:3.3 \times 10^4$

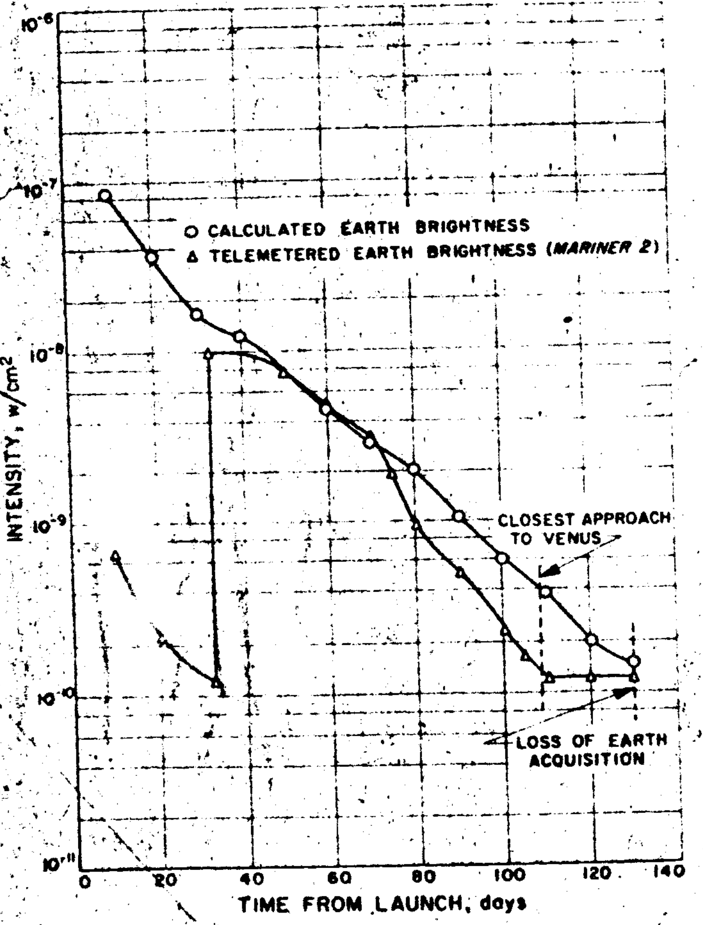

Fig. 7. Earth brightness versus flight time

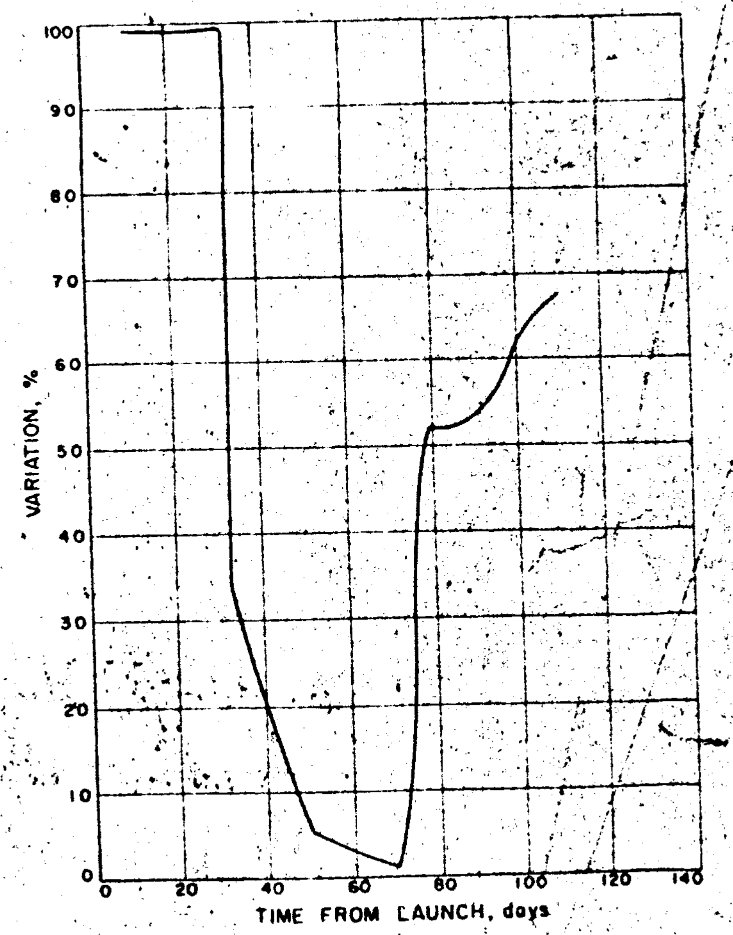

Fig. 8. Flight versus calculated Earth brightness deviation